SYNTHESIS OF PRECIOUS METAL NANOPARTICLES IN MESOPOROUS SOLIDS AND THEIR CATALYTIC PROPERTIES

A THESIS SUBMITTED TO THE

UNIVERSITY OF PUNE

FOR THE DEGREE OF

DOCTOR OF PHILOSOPHY

IN

CHEMISTRY

BY

ATUL KUMAR

Dr. RAJIV KUMAR

(RESEARCH GUIDE)

CATALYSIS AND INORGANIC CHEMISTRY DIVISION
NATIONAL CHEMICAL LABORATORY
PUNE 411008
INDIA

MAY 2011

DECLARATION BY RESEARCH GUIDE

Certified that the work incorporated in the thesis entitled: "**Synthesis of precious metal nanoparticles in mesoporous solids and their catalytic properties",** submitted by Mr. Atul Kumar, for the Degree of ***Doctor of Philosophy,*** was carried out by the candidate under my supervision at Catalysis and Inorganic Chemistry Division, National Chemical Laboratory, Pune-411008, India. Such material as has been obtained from other sources has been duly acknowledged in the thesis.

Dr. Rajiv Kumar

(Research Supervisor)

DECLARATION BY RESEARCH SCHOLAR

I hereby declare that the thesis entitled "**Synthesis of precious metal nanoparticles in mesoporous solids and their catalytic properties",** submitted for the ***Degree of Doctor of Philosophy*** to the University of Pune, has been carried out by me at Catalysis and inorganic Chemistry Division, National Chemical Laboratory, Pune-411008, India, under the supervision of Dr. Rajiv Kumar. The work is original and has not been submitted in part or full by me for any other degree or diploma to this or any other University.

Atul Kumar

.....*Dedicated*

To my

Beloved Parents

And

Brother

Acknowledgement

It is my great pleasure to acknowledge my research supervisor Dr. Rajiv Kumar who introduced me to a fascinating realm of chemistry. I am grateful to him for giving me liberty to carry out my research work independently throughout the course of this programme. My deepest personal regards are due for him forever.

I am deeply indebted to Dr. Nandini Devi for her invaluable guidance and unconditional support. Her constant inspiration and constructive criticism helped me a lot to focus my views in proper perspective. Her tireless attitude has been an impetus for me throughout the course of study. I take this opportunity to express my deepest sense of gratitude and reverence towards her for guiding me in the right direction throughout the course of this work.

My heartfelt thanks to Dr. C.V.V. Satyanarayna for his helping hands and fruitful discussions. I wish to express my sincere gratitude to Dr. Maya Devi for kinetic studies and Dr. Rajmohanan for NMR studies. I would like to thank R. P. Hodgkins for his scientific contributions to my research work. I am thankful to Dr. A. P. Singh, Dr. P. L. Dephe, Dr. Anil Kinage and Dr. Raja for helping in every possible way during my tenure in NCL. I also thank Dr. Guruswamy, Dr. Amol Kulkarni and Dr. Ajit for their scientific discussions. I am also thankful to Dr. Nilima, Mr. Gholap, Mr. Dev, Narender, Anuj and Panderaj for TEM and Ketan for SEM.

I sincerely acknowledge the help provided by Dr. Subhangi Umbarkar, Dr. Seema Deshpande, Dr. Kala Raj, Dr. Joshi, Dr. C. S. Gopinath, Dr. Belegar, R. K. Jha, Ms. V. Samuel, Dr. Selvaraj, Purushotam, Tejas, Niphadkar and other scientific and non scientific staff of catalysis division. I would also like to acknowledge the help received from Mr. Madhu, Mr. Milind and Mr. Jagtap of catalysis division and Mr. Mane from NMR division.

It gives me great pleasure to thank my labmates Dr. Senapati, Dr. Amit, Dr. Pranjal, Dr. Mahesh, Dr. Binuraj, Aparna, Pravin, Pooja, Tusar, Anupam, Rajesh, Jijil, Sumona, Leena, Saumya, Ramit, Manoj, Deepa, Anup, Prasanjeet, Babashaeb, Rakesh, Jitesh, Raj, Dhanshekhar, Cristy and Asha for their helpful hand and making the lab feel like a family. Without their support it would not have been possible to complete this task.

I would like to express my gratefulness to colleagues in the division- Dr. Surendran, Dr. Srikant, Dr. Selvakumar, Dr. Chitanmbaram, Sheetal, Shital, Sanjay, Shoy, Aneesh, Priti, Dr. Ankush, Dr. Ankur, Dr. Suman, Dr. Shanbag, Dr. Neelam, Trupati, Swati, Rajni, Vaibhav, Dr. Lakshi, Dr. Maitri, Dr. Surekha, Dr. Deu, Mahajbeen, Bogesh, Nagraj, Tusara, Sivaranjini, Edwin, Ganesh, Richa, Nishita, Narshimha, Lakshman and other research scholars in catalysis division for their constant support throughout my stay in NCL. Special thanks to Koteshwar Rao, Reji, Hanumant, Santosh and Kalpana for their help throughout the course of my work. Many

thanks to Kaja, Ravikumar, Mangesh, Anal, Kamendra, Malvi, Vijay, Hilda, Eldoh, Anny, Hari, Jima, Venugopal, Divya, Pradeep, Nishant, Ravindra, Debashis G. and Subhash for their timely help.

I would like to express my appreciation to my colleagues and friends, Anuj, Jitender, Umesh, Kaushal, Adish, Anand, Hamender, Prakash, Ajeet, Kunal, Sanjay, Ajay and Prince for the wonderful time I had with them. I am grateful to my dear friends Deepak and Ramakanta for their sympathetic ears and making my stay at NCL a very comfortable and memorable one. It gives me great pleasure to thank my old friends, Kishan, Anil, Pushpender, Sunil, Vishal and others from whom I have received unfailing support and encouragement during many years of studies.

I have to acknowledge especially my teachers in B.Sc. and M.Sc. class who really nourished my interest in Chemistry. It gives me great pleasure to thank my parents and family members, for their love, unfailing support, tremendous patience, trust and encouragement that they have shown to me. Due adoration to my brother Vijay for his steadfast faith in my capability has always spurred me to go ahead, especially in difficult times.

Finally, my thanks are due to Council of Scientific and Industrial Research, Government of India, for awarding the research fellowship, and to Dr. S. Sivaram, former Director and Dr. Saurabh Pal, Director, National Chemical Laboratory, to carry out my research work and extending all possible infrastructural facilities, and to allow me to submit this work in the form of a thesis for the award of Ph.D. degree.

May 2011 *Atul Kumar*

ABSTRACT

Catalysis by nanoparticles has attracted attention due to its unique significance in academia and considerable contributions to industry. Highly dispersed metal nanoparticles play a significant role in many catalytic reactions. The employment of such catalysts span decades from earliest examples of Pt/Al_2O_3 in petroleum reforming to precious metals like Rh, Pt and Pd in three way catalysts for treatment of automobile exhaust developed recently. Since active centers in metal nanoparticles are present on the surface and the surface features of the metal nanoparticles change with shape and size, activity and selectivity can be tuned by controlling these parameters. To explore nanosize effect in catalysis, one needs to be able to synthesize monodispersed metal nanoparticles with controlled shape and size and with high thermal stabilities, which has been proved to be extremely difficult in practice. Conventionally, inert inorganic supports with rigid frameworks and high surface areas are being used to get higher dispersion of metal nanoparticles. However, non-uniform pore structure of the traditional supports viz. high surface silica and alumina makes the preparation of monodispersed particles difficult and the obtained metal nanoparticles are often randomly distributed. The discovery of mesoporous silica materials has initiated intensive interest in various research areas. These mesoporous silica materials have large networks of channels and pores giving them very high porosity and surface area - advantageous for supporting metal nanoparticles. Moreover, the fact that the pore dimensions and pore characteristics can be easily fine tuned makes them more attractive for engineering the size, morphology and electronic properties of the encapsulated nanoparticles.

In the present work, a novel *in situ* method has been developed to synthesize the metal nanoparticles in channels of SBA type mesoporous silica solids. This gives a narrow size distribution of metal nanoparticles in the mesoporous channels. This method is found to be versatile in varying the size and morphology of the nanoparticles by changing synthetic conditions and template characteristics. Several attempts also have been made to thoroughly characterize these systems as well as to understand the mechanism of formation of metal nanoparticles. Mechanism of formation of various morphologies of Pt nanoparticles in SBA-15 channels has been investigated by studying the metal precursor-mixed micelle composite by UV-Visible, NMR and IR spectroscopy. Catalytic activities of various sizes of Pt nanoparticles

synthesized in mesoporous channels have been studied for CO oxidation reaction. Effect of size of Pt nanoparticles on the selectivity of the reaction has also been studied by using these materials in hydrogenation of cinnamaldehyde. The thesis is presented in five chapters, a brief summary of which is given here.

Chapter 1 gives general introduction to the metal nanoparticles in catalysis and role of their shape and size in selectivity of the reaction. This chapter also describes the current status of nanotechnology in which various methods for synthesising the monodispersed metal nanoparticles are discussed. Various methods for synthesizing the metal nanoparticles in mesoporous channels reported in literature are described. Advantages of mesoporous silica in comparison to conventional silica and alumina as support for metal nanoparticles are discussed. Basic principles of various physico-chemical techniques used to characterize the metal nanoparticles containing mesoporous silica solids are also given.

In Chapter 2, *in situ* method for synthesizing the metal nanoparticles in mesoporous channels is discussed. Cationic surfactant helps in anchoring the metal precursor in polymer micelle corona during the synthesis which is prerequisite to synthesizing metal particles in mesoporous channels. Effect of different concentrations of CTAB on the pore size and mesoporous order of SBA-15 has been studied. Pt/SBA-15 synthesized using optimum concentration of CTAB in triblock-copolymer P123 and hexachloroplatinic acid as platinum precursor has been characterized by X-Ray diffraction, N_2 adsorption, SEM and HRTEM studies. ICP has been used to determine the platinum content in the samples. This chapter also includes *in situ* X-ray diffraction and *in situ* UV-Visible studies during calcination to probe the mechanism of formation of platinum particles. Au and Pt-Au/ SBA-15 have been synthesized using the same *in situ* method and characterized by using X-ray diffraction, N_2 adsorption, UV-Visible spectroscopy and HRTEM studies.

Chapter 3 is divided in to two parts. Part A includes the synthesis of various morphologies of Pt in mesoporous channels of SBA-15 by slightly changing the synthesis conditions. These materials have been characterized by X-ray diffraction, N_2-adsorption, HRTEM, SEM and elemental mapping by EDX. Mechanism for the formation of different morphologies of platinum have been investigated by UV-Visible, NMR and IR studies of metal precursor mixed micelle composite. In part B, effect of channel size in controlling the particle size of platinum nanoparticles has

been studied by synthesizing the platinum nanoparticles in mesoporous SBA-12. XRD, N_2 adsorption and SEM studies have been carried out to study the effect of different concentrations of CTAB on the order and pore size of SBA-12 materials. HRTEM studies of Pt/SBA-12 materials show Pt nanoparticles of size varying from 4-5.5 nm in the channels of mesoporous SBA-12. Pt content in all the materials have been analysed by inductively coupled plasma technique. Platinum has also been incorporated in three dimensional mesoporous material FDU-12 using the same *in situ* method.

In Chapter 4, effect of particle size over activity of catalyst was studied by taking CO oxidation as model reaction. In this study four different particle sizes (1.8, 3.6, 4.4 and 8 nm) of platinum supported over SBA type materials were screened for their activity in CO oxidation at various flow rates. Kinetic studies have been done to find out the activation energy of CO oxidation over various Pt particle sizes. Pt/SBA materials with different average sizes of platinum particles have also been studied for understanding the effect of size on the selectivity in cinnamaldehyde hydrogenation.

Chapter 5 gives overall conclusion of the work done. As a whole this thesis describes a novel *in situ* method for synthesizing metal nanoparticles in channels of mesoporous solids. Flexibility of the method has been proved by synthesizing the Pt metal nanoparticles in various mesoporous solids like two dimensional SBA-15, SBA-12 and three dimensional FDU-12. Au and Au-Pt nanoparticles have also been synthesized in mesoporous SBA-15 using the same method. Size and shape sensitive reactions like hydrogenation of α, β-unsaturated aldehydes and CO oxidation have been taken as model reactions to understand the systems comprehensively.

TABLE OF CONTENTS

MESOPOROUS SBA-15

List of Figures

List of Schemes

List of Tables

List of Abbreviations

BET	Braunauer-Emmett-Teller
BJH	Barrett-Joyner-Halenda
CMC	Critical Micellization Concentration
CTAB	Cetyltrimethyl ammonium bromide
CVD	Chemical Vapor Deposition
DFT	Density Functional Theory
DR	Dubinin-Radushkevich method
F127	Pluronic F127 Triblock Co-polymer
FID	Flame Ionization Detector
FSM-16	Folded Sheet Material
FTIR	Fourier Transform Infrared
GC	Gas Cromatography
GHSV	Gas hour space velocity
EDAX	Energy Dispersive X-Ray Analysis
HK	Horvath-Kawazoe method
HRTEM	High Resolution Transmission Electron Microscopy
ICP-OES	Inductively Coupled Plasma-Optical Emission Spectroscopy
MCM	Mobil's Crystalline Material
NMR	Nuclear Magnetic Resonance
P123	Pluronic P123 Triblock Co-polymer
PEO-PPO-PEO	Polyethylene oxide-polypropylene oxide-polyethylene oxide
PVP	Poly(vinylpyrrolidone)
SBA	Santa Barbara Amorphous
SEM	Scanning Electron Microscopy
TEOS	Tetraethyl orthosilicate
TEM	Transmission Electron Microscopy
TMOS	Tetramethyl orthosilicate
TSP d_4	3-Trimethylsilyl propionic acid 2,2,3,3, d_4 sodium salt
UV-Vis	Ultraviolet-Visible
XRD	X-Ray Diffraction

CHAPTER 1

INTRODUCTION
AND
LITERATURE REVIEW

1.1. INTRODUCTION

Metal nanoparticle based catalysts were developed as early as 1920's for hydrocarbon conversion, partial oxidation and combustion reactions [1]. Even in the early stages of development, an awareness of the peculiar attributes of "smallness" of the active metal sites existed. Taylor pointed to the possibility of "detachment" of atoms from metal surfaces making them more active [2]. Hence it will not be an exaggeration to say that heterogeneous catalysis is the oldest form of nanotechnology in practical use much before the word was coined [3].

A large number of industrially important catalysts are metal particles, sized few nanometres, supported on "inert" oxides like silica or alumina. Activity of the catalyst depends on the dispersion, size, shape, morphology and surface properties of the metal nanoparticles. There is a clear interdependence of these parameters as revealed by different atomic planes exposed in nanoparticles of different shapes and sizes. Fig. 1. depicts different platonic and related geometries adapted by solids in general which can also be envisaged for nanoparticles.

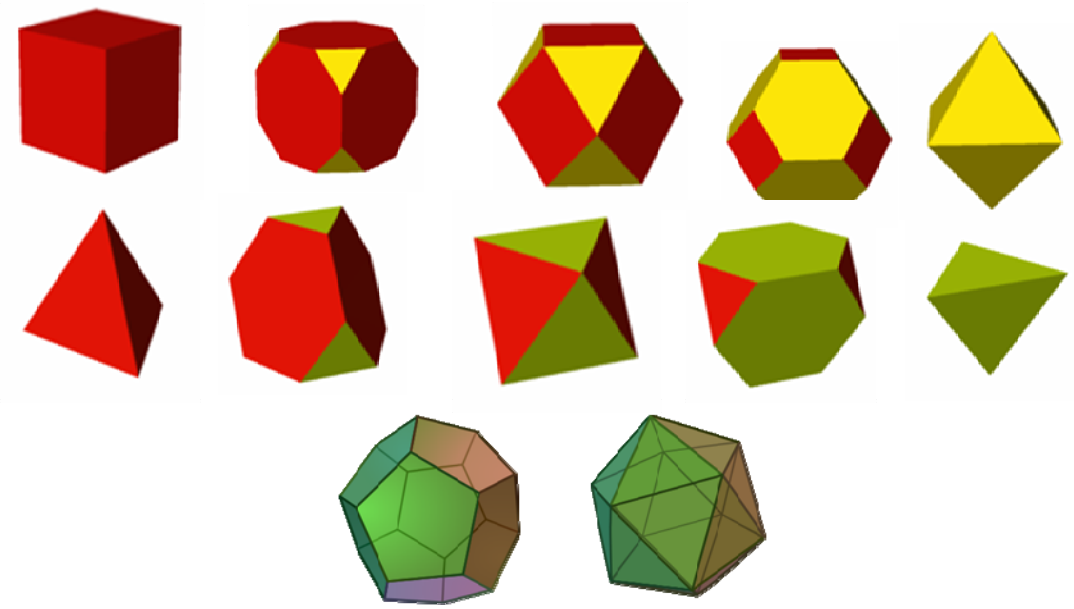

Fig. 1.1. Various platonic and related geometries possible for nanoparticles. [Source: http://en.wikipedia.org.]

As is evident from the figure, different planes are exposed when the shapes change. For example, when the (111) planes of a cuboctahedron is preferentially allowed to grow, an octahedron is formed whereas (100) plane growth leads to a cube. This affects the characteristic atomic plane exposed in various shapes of nanoparticles.

Hence an octahedron has only (111) planes exposed and a cube exposes (100) planes. A cuboctahedron exposes both depending on the size of the nanoparticle.

Such an observation has immense implications on catalysis since the natures of the atomic planes dictates the adsorption characteristics of molecules, a phenomenon which forms the heart of heterogeneous catalysis. For example, in case of platinum which is a very well known nanocatalyst with a FCC unit cell, (110), (100) and (111) planes show different close packing tendencies (Fig. 1.2.)

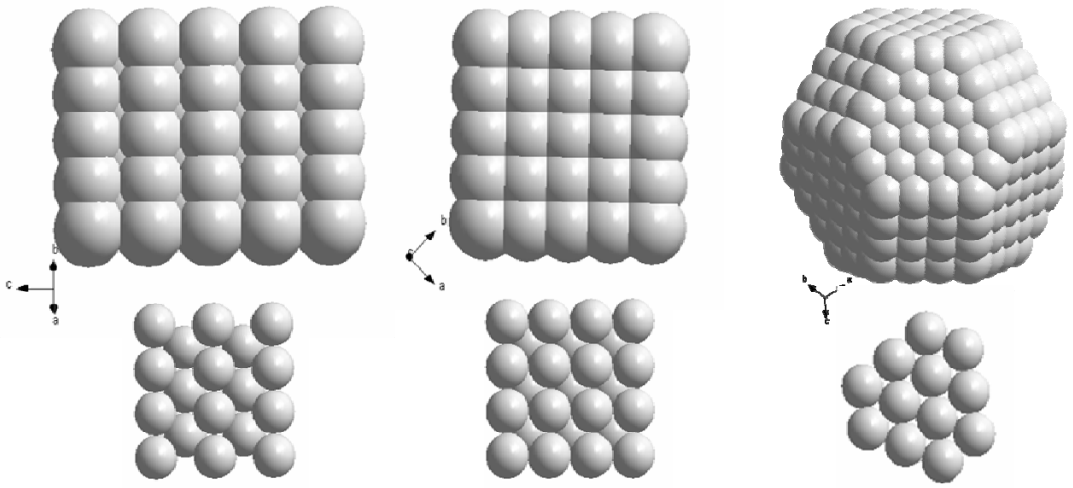

Fig. 1.2. Different close packing geometries in different planes for an FCC unit cell (left) (110), (middle) (100) and (right) (111).

This in-turn affects the adsorption transition state geometry of molecules and hence activity and selectivity. This is highlighted in the case of hydrogenation of α, β-unsaturated aldehydes which is an industrially important reaction. Three possible hydrogenation products can be formed in such processes (i) the C=C double bond is hydrogenated to give the saturated aldehydes (ii) the C=O bond is hydrogenated to give unsaturated alcohol and (iii) both C=C and C=O bonds are hydrogenated to give saturated alcohol, the desired product being unsaturated alcohol. It was found that adsorption energies of C=C and C=O bonds on different planes are different and this can be exploited for improving the selectivity of the catalyst [4, 5].

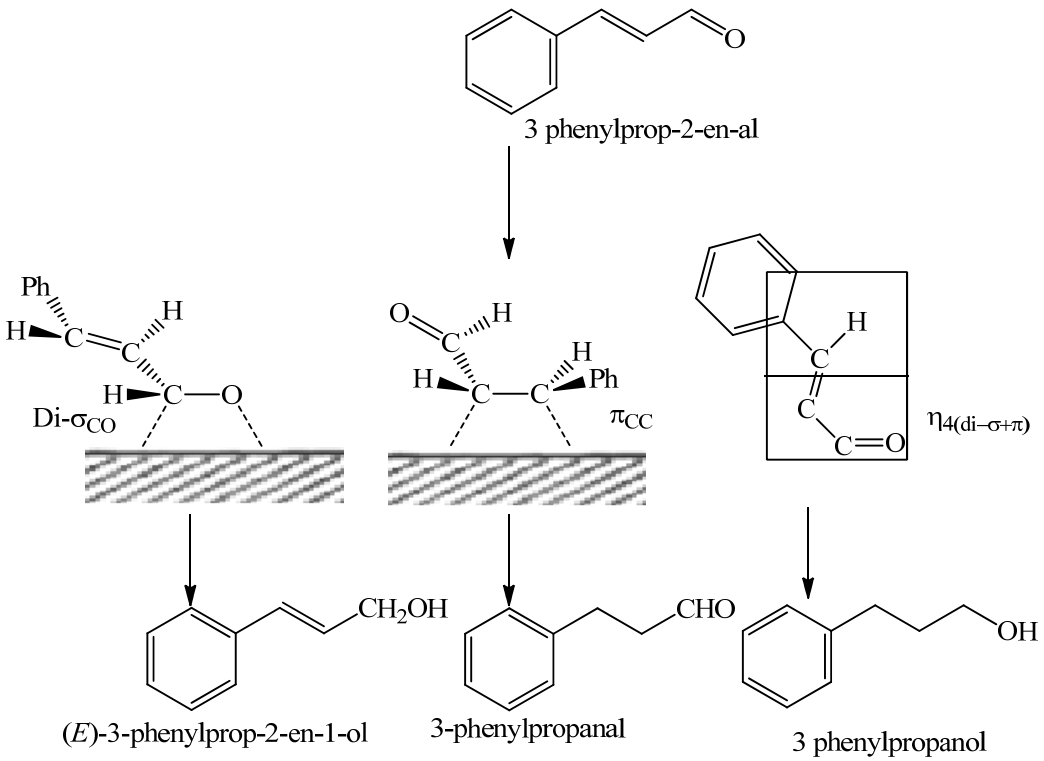

Scheme 1.1. Various adsorption geometries of 3-phenylprop-2-en-al yielding different products.

This concept is also evident in benzene hydrogenation to give cyclohexene (CHE) and cyclohexane (CHA) [6]. Pt cuboctahedra expose both (111) and (100) planes and cubes expose exclusively (100) planes. Selectivity for cyclohexane is high in case of Pt (100) hence cubes produce exclusively cyclohexane.

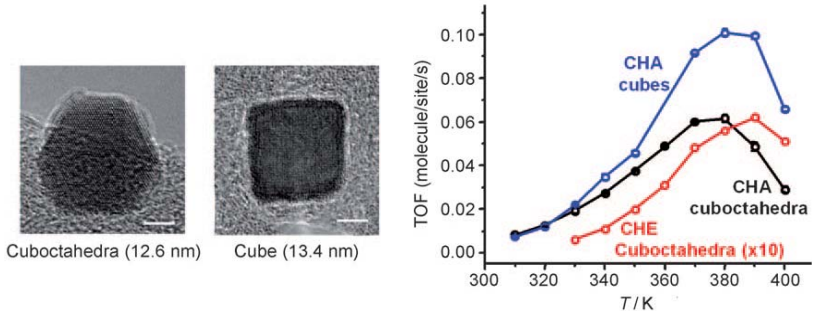

Fig. 1.3. Effect of shape of Pt particles on hydrogenation of benzene. [Source: Ref. 6]

Monodispersity of the particles become highly relevant in this context. Another parameter important to the industrial catalysis is the deactivation of metal nanoparticles by sintering, a phenomenon leading to agglomeration of small particles to form bigger particles [7-10]. The change in size, hence shape as well as overall

energetics of the particle surface is one of the main problems plauging chemical industry at this time.

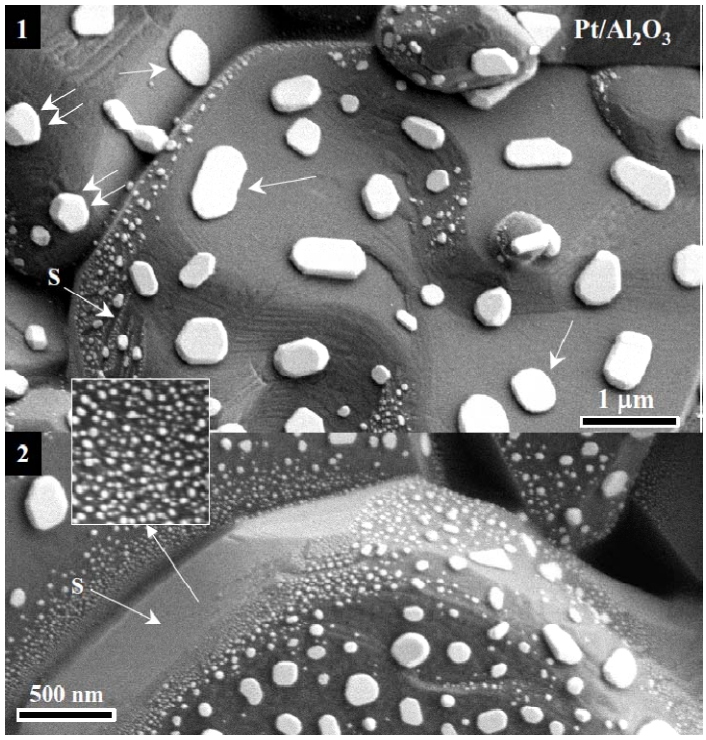

Fig. 1.4. *In situ* SEM images of Pt/Al_2O_3 catalyst showing the agglomeration of Pt particles on certain faces of the alumina support. S denotes unchanged particles. [Source: Ref. 7]

In the last century, emphasis was on activity and productivity by the chemical industry. However, stricter regulations as well as better awareness of pollution effects of various chemicals released into the environment have led to a paradigm shift in their focus. This may have happened due to regulatory effects or a conscious effort from the community to put the principles of "Green Chemistry" into practice or both. Hence more steps are taken to avoid unwanted side products, reduced steps of syntheses, use of easily separable catalysts etc. Turn of this century, therefore, has seen an increased focus on the concept of selectivity [11-13]. Since usually the industrial catalysts are metal nanoparticles on various supports, this concept can be implemented by controlling the shape and size of the nanoparticles.

1.2. CURRENT STATUS OF METAL BASED NANOMATERIALS

Engineering metal nanoparticles with different size and morphology is very well established now. For example, Co nanoparticles of varying sizes and shapes were synthesised in a coordinating ligand and surfactant system whereby organometallic

$Co_2(CO)_8$ was allowed to rapidly nucleate in hot *o*-dichlorobenzene and stabilised in a mixed surfactant system consisting of oleic acid and trioctylphosphine oxide (TOPO). Quenching the reaction for different durations shows an excellent control on the morphology of the resulting nanoparticles [14]. The rapidly formed nuclei are allowed to be coated with the coordinating ligand followed by subsequent charge transfer leading to the modification of surface tension and size control. It was observed that hcp-Co rods were obtained in the surfactant mixture on injection which transformed in to ε-Co with a spherical morphology.

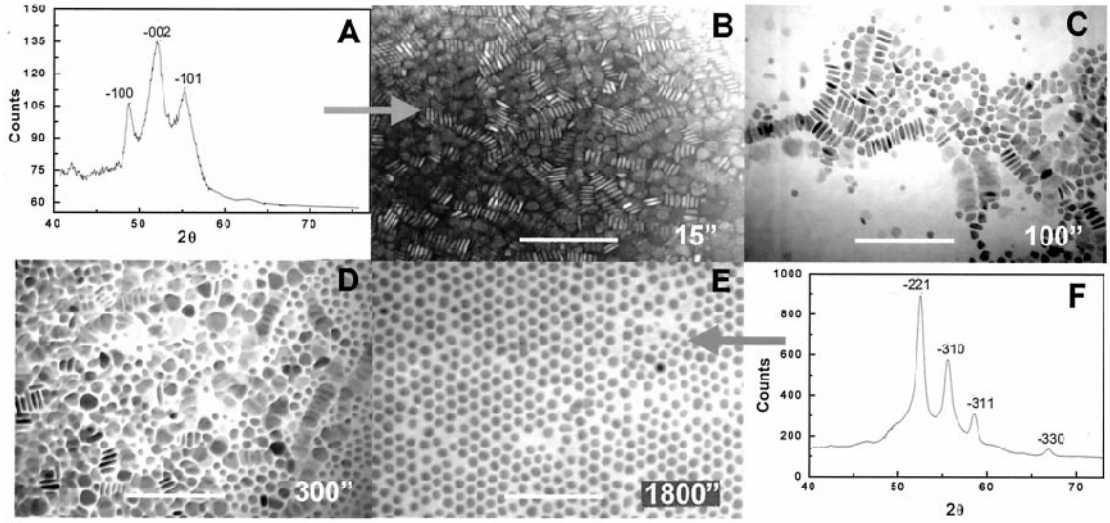

Fig. 1.5. Transformation of hcp-Co into ε-Co with time; A) XRD pattern at 15 s corresponding to a hcp-Co crystal structure; B) hcp Co rods at 15 s, C) 100 s, D) 300 s and E) 1800 s; F) XRD pattern at 1800 s corresponding to a ε-Co crystal structure. Bar, 100 nm. [Source: Ref. 14]

Precise control over the sizes of Pd, Ag and Pt nanoparticles was achieved by fine tuning of synthetic parameters. These were prepared from simple salts, reduced by mild agents like ethylene glycol, citric acid or ascorbic acid and stabilised with polymers or surfactants. In these cases, the formation of nanoparticles is supposed to be initiated by nucleation and seed formation which subsequently grow into nanocrystals of specific geometries. For example, in fast reduction of $Na_2[PdCl_4]$, as in the case when ethylene glycol is used, single crystal seeds grow into cuboctahedra in presence of air [15]. However, slight changes in the temperature as well as addition of Br^- ions which are expected to adsorb on the seed surfaces and alter the surface energy and growth patterns, lead to the formation of an array of shapes from nanobars to nanorods and cubes [16, 17]. It is reported that twinning effects also can be controlled by slow reduction using citric acid to obtain various shapes and sizes of

nanoparticles. Similar versatility is observed for other metals like Ag, Au, Pt, Fe etc. [18].

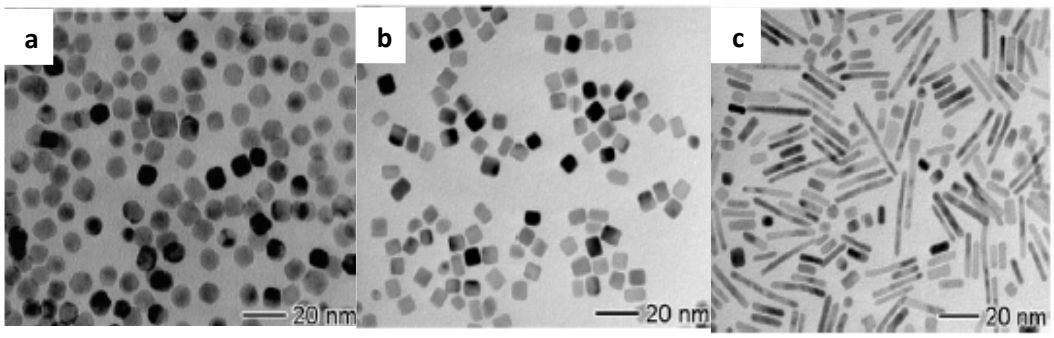

Fig. 1.6. TEM images of Pd nanostructures; a) cuboctahedra prepared in ethylene glycol at 110°C, (Source: Ref. 16) b) nanocubes prepared in water and in the presence of KBr at 100°C, (Source: Ref. 15) and c) nanorods prepared in ethylene glycol-water mixture at 120°C in presence of KBr. (Source: Ref. 17)

Various biological agents like fungi, plant extract etc. are also used for reduction of aurochloric acid to give gold nanoparticles with different shapes and sizes [19, 20].

Even though these giant leaps have taken us closer to achieving better control of the size and shape of nanoparticles and also better understanding of their growth mechanisms, translating these advances into successful applications in catalysis has been a difficult task. One of the main drawbacks is the homogeneity of the nanoparticle solutions which prevents recycling. Moreover, there is a possibility for agglomeration and sintering of the nanoparticles under harsh catalytic reaction conditions since they are usually stabilized in organic moieties like capping agents and protective polymers. Hence it is imperative to support the nanoparticles effectively on solid and stable materials which would aid in minimizing such deactivation processes. In conventional catalyst preparation methods, metal particles are stabilized on the surface and within the macropores of oxide supports just by adsorption of precursor ions and subsequent reduction. However, in such cases, control on particle size is poor and they are loosely anchored on the surface and tend to sinter at higher temperatures (Fig. 1.4). One way to minimise this effect would be to encapsulate the nanoparticles within the oxide support thereby preventing further growth and sintering, at the same time not compromising on the access to the active sites. It is now possible to implement this concept advantageously with the advent of mesoporous compounds with pores in range of ~3 nm to ~30 nm, ideal for incorporation of metal nanoparticles (Fig. 1.7).

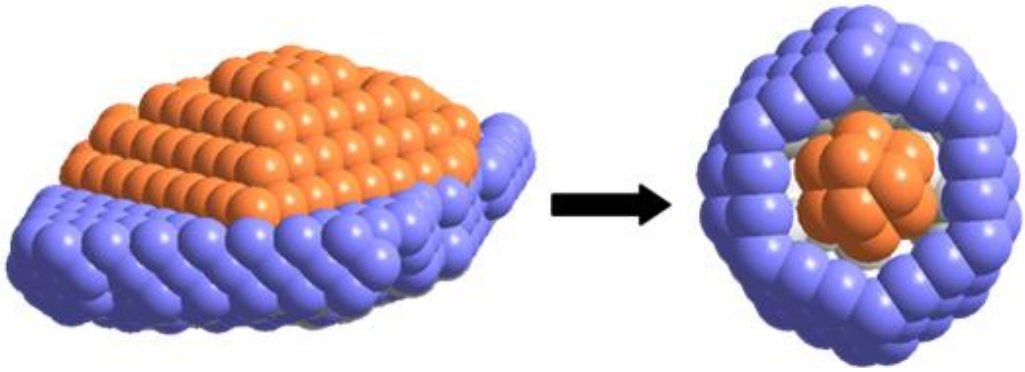

Fig. 1.7. Encapsulation of metal particles inside the channels preventing agglomeration.

1.3. MESOPOROUS COMPOUNDS

First reports of ordered mesoporous silica were made by Mobil scientists in the early 1990's as M41S series of compounds of which MCM-41 caught attention with its hexagonally stacked one-dimensional channels [21]. These compounds were made from cationic surfactant micelles as templates. This was followed by the discovery of SBA series of compounds by Prof. Galen Stucky's group in Santa Barbara in 1998, utilizing non-ionic block copolymer micelles and non-ionic surfactants as templates [22]. A number of studies have been carried out to understand the mechanism of formation of these compounds using NMR and scattering experiments [23-26].

In the M41S series of materials, it is suggested that charged oligomeric silica species interact strongly with the cationic head groups of micelles under specific conditions (Fig. 1.8). This leads to a drastic reduction in electrostatic repulsion between the micelles and favours rapid self-assembly [27].

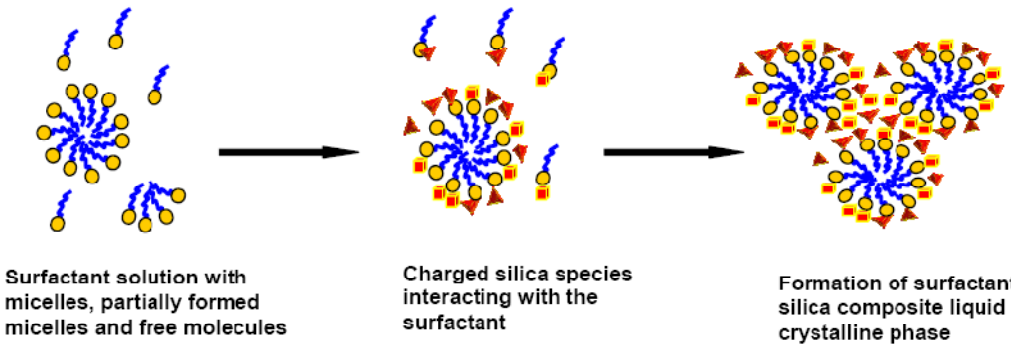

Fig. 1.8. Mechanism of formation of mesoporous silica with charged surfactants.

Whereas, for SBA series of silica based mesoporous materials prepared under highly acidic conditions, the involvement of repulsive force between the micelle is proposed [22]. Here, cationic silica species are hydrogen bonded to the oxygen atoms in the hydrophilic region of the micelles. Initially, the hydrophobic organosilica precursor like tetraethoxy or tetramethoxy silane penetrates into the hydrophobic core of the micelle and progressively gets hydrolysed and transported towards the corona and surface, which further condenses to form the mesophase. This mechanism is evident from the presence of micro porosity in SBA-15 when compared to MCM-41. Even though the exact mechanism of formation is not clear, we can assume that condensation of silica aids the aggregation of micelles into hexagonal, cubic or lamellar structures [28] leading to mesophased silicas with varied morphologies (Fig. 1.9).

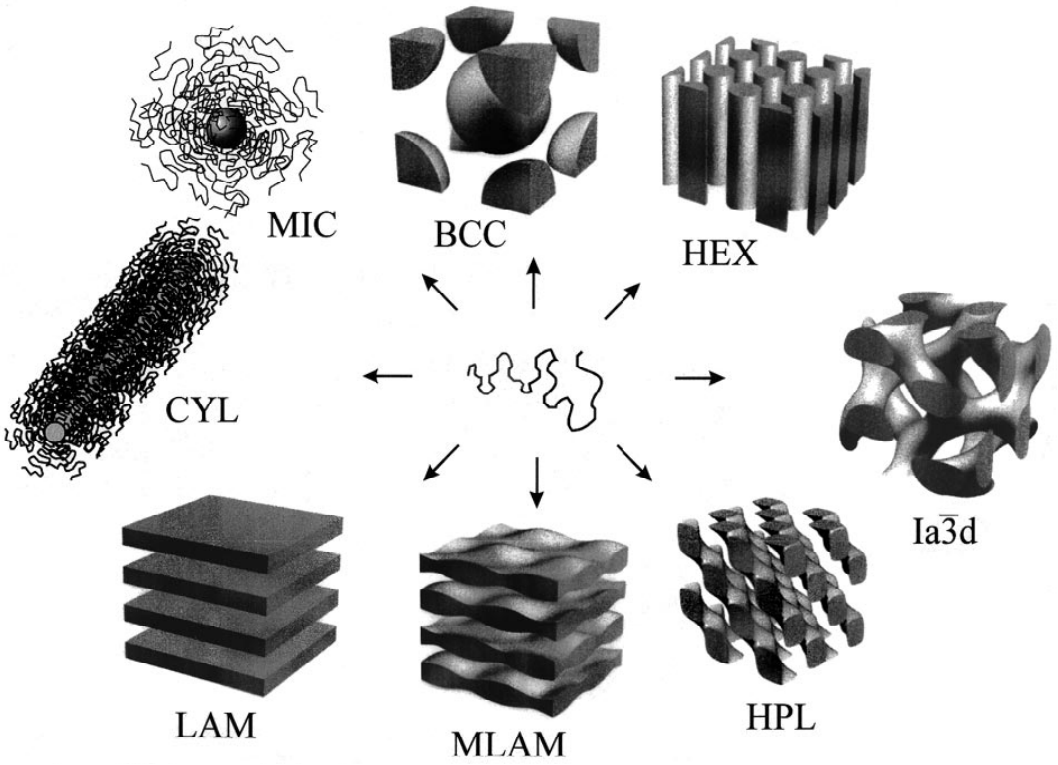

Fig. 1.9. Common morphologies of micro phase-separated block copolymers; body centred cubic packed spheres (BCC), hexagonally ordered cylinders (HEX), gyroid (Ia3d), hexagonally perforated layers (HPL), modulated lamellae (MLAM), lamellae (LAM), cylindrical micelles (CYL), and spherical micelles (MIC). [Source: Ref. 28]

It is evident from these structural studies that the pore structure is definitely dependent on the micelle template characteristics, especially size. One of the most important advantages of utilising mesoporous compounds for encapsulating nanoparticles is that the pore characteristics are easily tuneable. Since the pore

dimensions are mainly dependent on the hydrophobic part of the template, it can be varied by changing the alkyl chain length as in the case of alkyl ammonium surfactants or by molecular weights of the hydrophobic part in polymeric templates. Various ways of fine tuning of the pore structure also have been reported, mainly by changing the hydrophobic/hydrophilic characteristics as well as by using mixed micelles or changing synthetic conditions.

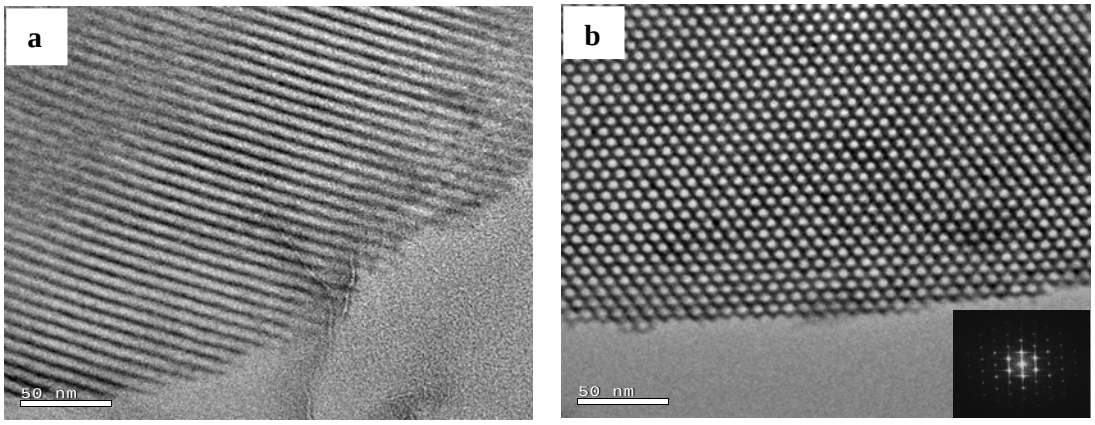

Fig. 1.10. A representative TEM images of SBA-15 showing the presence of channels; a) perpendicular to them, b) down the channels.

The resulting silica framework after removal of the micelle template by extraction or calcination has porous and high surface area structures. The high surface area and their appropriate channel structure is conducive for encapsulating metal nanoparticles making these materials ideal in catalysis and adsorption industries.

1.4. ENCAPSULATION OF METAL NANOPARTICLES IN MESOCHANNELS

Various methods have been developed to achieve encapsulation of nanoparticles within the mesochannels. In general mesoporous compounds are used as high surface area hosts for encapsulation of metal nanoparticles using conventional methods like impregnation, ion exchange as well as novel methods like grafting of ligands to anchor nanoparticles. The methods for encapsulation of already synthesised nanoparticles either *in situ* or by sonication have been also used recently [29, 30].

The simplest way reported for the synthesis of supported catalysts based on mesoporous oxides is incipient wet impregnation also regarded as dip-coating whereby metal precursor solution is allowed to be adsorbed on the silica surface which on calcination forms metal nanoparticles supported on the surface, both inside

the channels and on the surface of mesoporous silica particles. It has been observed that Ag nanoparticles owing to uncontrolled growth of particles on solid supports lead to bimodal distribution of nanoparticles [31].

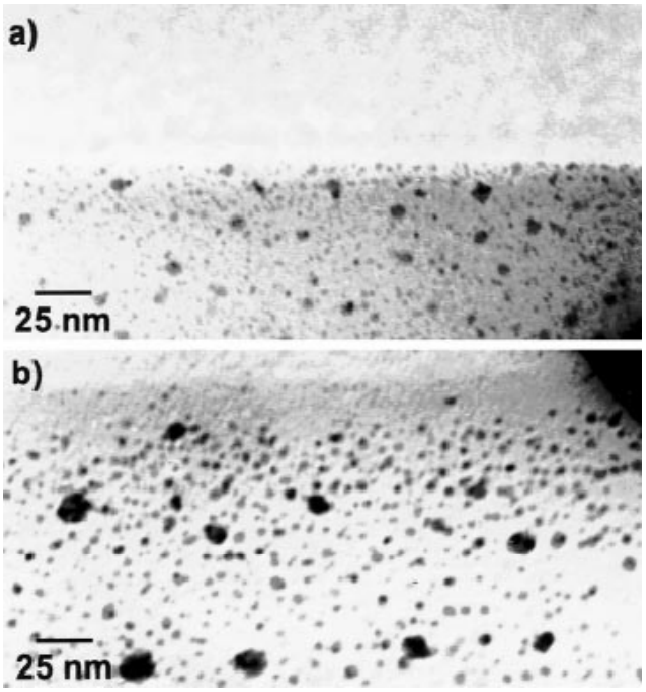

Fig. 1.11. TEM images of Ag particles in mesoporous silica after reductive treatment at 450^{o}C. [Source: Ref. 31]

Various morphologies like spherical particles and nanowires have been prepared by this method, the latter being carried out using very high concentrations and repeated impregnation steps [32]. It is also observed that calcination and reduction may have an effect on the particle size. However, a correlation of these varying morphologies to the synthetic conditions is not yet very clear. The main disadvantage of this methodology is the possibility of agglomeration of the particles on the surface. Same is the case with ion-exchange method where surface agglomeration cannot be avoided. A slight improvement in distribution and stability is obtained by grafting organometallic complexes of metals to surface silanol groups. For example, $Co_2(CO)_8$ derived Co/SBA-15 was found to be as active as $Co_2(CO)_8$ homogeneous catalyst in Pauson-Khand reaction [33]. However, selective encapsulation within the channels and thereby prevention of surface growth of nanoparticles could not be achieved.

Another improved method involves grafting of ligands which will stabilise metal complexes which form precursors for nanoparticle formation. Functional groups like thiols, amines etc. can be grafted on to the inner walls of the mesoporous channels. These groups form a metal-ligand complex with the metal salt precursor thereby anchoring them strongly on to the walls. This method is versatile in the sense that this can be used for heterogenising and immobilising homogeneous, organometallic catalysts as well as facilitating formation of metal nanoparticles during thermal treatments. The metal particle formation can also be achieved by reduction processes involving agents like $NaBH_4$ as well as autoreduction. For example, Au nanoparticles were formed by reduction using $NaBH_4$ after grafting metal salt precursor to thiol or amine groups functionalized on the walls [34, 35].

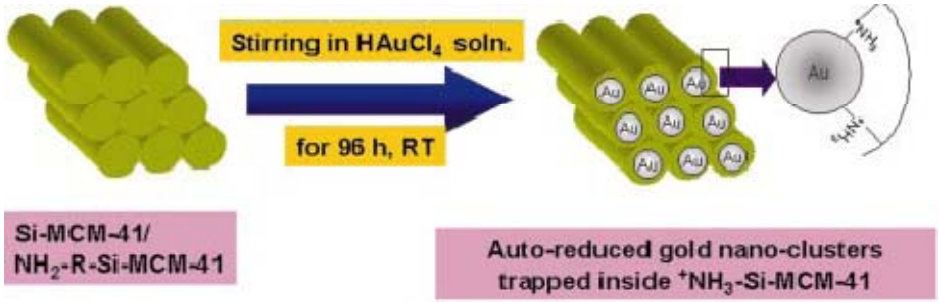

Fig. 1.12. Scheme representing the fuctionalization of inner walls of MCM-41 with amine groups which autoreduce chloroaurate ions. [Source: Ref. 35]

Similarly, anionic ammonium head groups of alkyl siloxanes have been employed to attract cationic precursor salts of Pd, Pt and Ag and anchored for further reduction into metal nanoparticles [36]. In some cases, thermal treatment is found to lead to a diffusion of metal particles out of the channels forming large particles outside the channels. The advantage of this method is that outer surface may be effectively deactivated preventing uncontrolled growth of nanoparticles on the surface. However, the disadvantage is that this may involve tedious surface fuctionalization processes and multi step synthesis. These conventional methods often give non-uniform dispersion of nanoparticles.

These problems are mostly addressed by recently developed *in situ* encapsulation methods. One such strategy exploits the advances made in synthesis and control of particle size in homogeneous systems. Primarily, uniform distribution of nanoparticles is made with controlled sizes and these pre-synthesized metal

nanoparticles are incorporated into the mesochannels either through *in situ* synthesis of mesoporous silica or by wet impregnation and capillary inclusion into already synthesised mesoporous compounds. Pre-synthesised Au nanoparticles of sizes 2, 5 and 20 nm were added to the surfactant solution prior to the addition of TEOS and further condensation in basic medium to give MCM-41 and MCM-48. Even though the Au nanoparticles were not visible in TEM images, other characterization methods including XRD, N_2 adsorption technique and sulphur XANES confirmed the presence of metal nanoparticles inside the channels. It was found that as the concentration of 2 nm particles increased, the channel became larger as evident from a low angle shift in XRD [37]. As mentioned earlier, MCM-41 has low shelf life as well as stability when compared to SBA-15 prepared under highly acidic conditions. However, the above mentioned method is not conducive for the incorporation of metal nanoparticles in to SBA-15 [38] since the protected nanoparticles are not normally stable under the synthetic conditions of SBA-15. When such a synthesis was followed, it is found that the resulting encapsulated Pt was not catalytically active. However, if SBA-15 type of mesoporous silica can be synthesised under neutral pH conditions, this problem can be avoided. In this context, the same group has reported an elegant method in which Pt colloidal solution is prepared and stabilized in a capping agent poly (vinylpyrrolidone) (PVP) and encapsulated within the SBA-15 silica framework synthesized at milder conditions. This was achieved by using a fluoride rich synthesis gel and TMOS as silica source with Pluronic P123 as template. Extensive characterisation on these materials revealed successful incorporation of presynthesised 1.7, 2.9, 3.6 and 7.1 nm sized Pt particles exclusively inside the SBA-15 channels [39]. PVP is a hydrophilic compound due to the pyrrolidone moiety, however, on interaction with Pt particles, this moiety gets attached to the Pt surface and the hydrophobic alkyl groups get exposed making this composite hydrophobic. On addition of this hydrophobic composite to P123 (which is a triblock copolymer forming a hydrophobic core and hydrophilic surface), they migrate to the hydrophobic core. On addition of TMOS and NaF, silica species hydrolyses and condenses over the P123 forming the mesoporous silica.

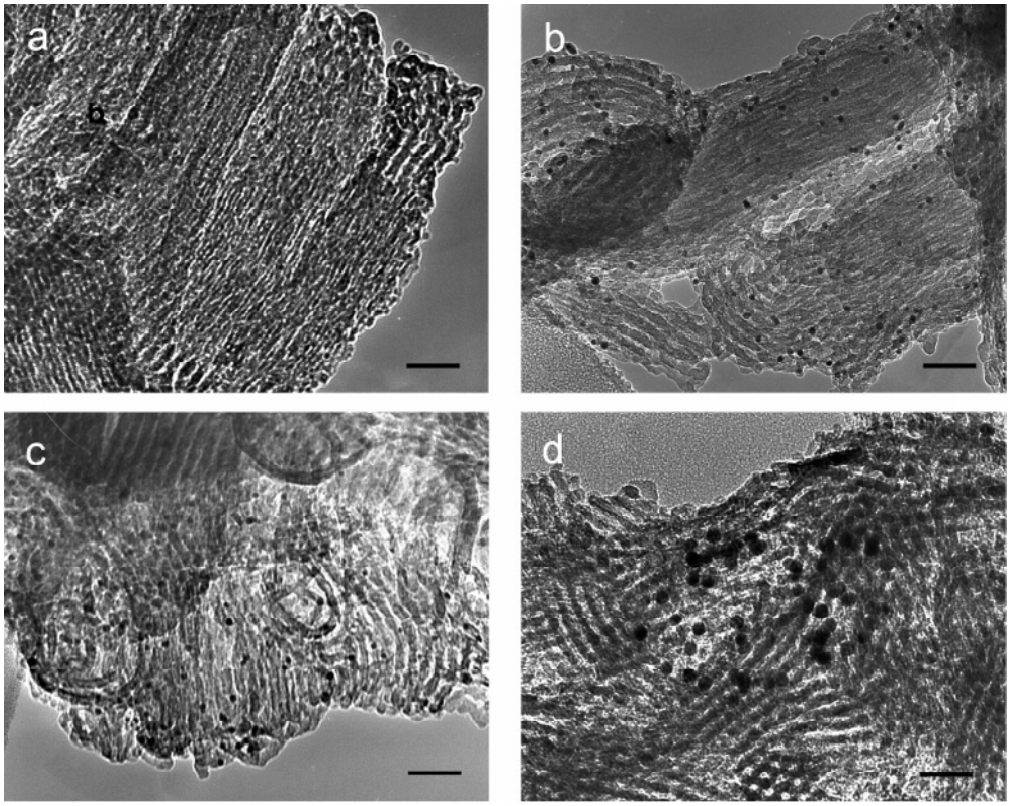

Fig. 1.13. TEM images of Pt/SBA-15 catalysts; a) 1.7 nm, b) 2.9 nm, c) 3.6 nm, and d) 7.1 nm. The scale bars represent 40 nm. [Source: Ref. 39]

Another method in which encapsulation is more ensured is the incorporation of the pre-synthesised nanoparticles into the calcined mesoporous compounds (viz. empty channels) by sonication [40]. It is said that sonication has enough driving power to push the particles inside the channels which probably makes this method better than incorporation by wet impregnation due to capillary effects. A more uniform distribution of particles inside the channels was observed for sonication method whereas surface agglomeration was observed in case of wet impregnation [41].

1.5. PROPERTIES OF MESOPOROUS MATERIALS WITH NANOPARTICLES

Nanoparticles when embedded in mesoporous solids, impart their properties to the materials due to spatial organization or location in the mesoporous channels. Nanoparticle incorporated mesoporous solids have properties which make them useful in three important areas: catalysis [42-44], optical [45-47] and magnetic materials [48, 49]. For catalytic applications, the most essential characteristics are interpenetrating pore structure of the mesoporous solids and formation of small particles located

within the pores. Such particles offer a huge surface area and superior catalytic properties in a variety of catalytic reactions. For optical materials, particle size, particle size distribution, and particle locations are crucial, so the ordered mesoporous oxides can also be perfect hosts for inclusion of optically interesting particles. For magnetic applications, particle size and particle size distribution are most crucial parameters determining the type of magnetic properties. Considering these requirements, particular synthetic methods should be chosen when certain applications are targeted.

1.5.1. Catalytic Activity

Numerous examples of reactions catalysed by metal nanoparticle supported on mesoporous compounds are reported in literature. Because of their durability and reusability, mesoporous oxides with nanoparticles can be successfully used as catalysts in such reactions where nanoparticles embedded in polymeric systems cannot be employed. As mentioned in Section 1.1, under thermal conditioning or long durations in isothermal conditions, nanoparticles due to their high surface energies, tend to agglomerate to bigger particles either by Ostwald ripening or particle movement and coalescence [50-52]. Mesoporous materials such as SBA-15 have thick pore walls and higher thermal and hydrothermal stabilities. It can be expected that if the particles are confined within the channels of mesoporous compounds, once the particle size and channel size matches, sintering can be minimised. An extensive study on Au inserted in mesoporous channels of various sizes showed that compounds with 1D channel are more capable of preventing growth by coalescence beyond 6 nm under reductive conditions at 400^{o}C [53]. Improved durability of metal and metal clusters supported on mesoporous compounds also was observed under reaction conditions [54, 55]. Yang et al. found that highly dispersed Pt nanoparticles confined within the SBA-15 showed no observable mobility at 773 K [56]. Dai et al. found that highly dispersed gold nanoparticles confined within channels of SBA-15 were highly resistant to sintering [57]. Pd nanoparticles confined in the complementary micropores of SBA-15 were found to show higher stabilities [58]. Metallic cobalt nanoparticles confined within the channels of SBA-15 were found to be air stable and reusable [59].

Another probable advantage of mesoporous catalysts is an appropriate use of pores as nano-reactors of certain size. This can be applicable to large molecules or to cyclization reaction where pore size and shape will influence the reactive path [60]. The isomerisation of n-hexane performed with Pt nanoparticle supported in MCM-41 aluminosilicates has been reported in [61]. The authors showed some improvement of the catalyst performance compared to disordered aluminosilica which might be caused by better control over nanoparticle growth. Palladium nanoparticles in MCM-41 pores synthesized by CVD method have been found to be efficient catalyst for Heck reaction [62].

There are various reports of hydrogenation of organic substrates using Pd or Pt nanoparticles embedded in mesoporous materials [63, 64]. One of the important applications of mesoporous solids with metal nanoparticles is hydro cracking of vacuum gasoil. Here reaction temperatures exceed 400°C and no polymer or other organic catalysts can be used. NiMo/MCM-41 has been found to have better performance in mild hydrotreating of a vacuum gasoil as compared to amorphous silica-alumina and USY zeolites with same Ni and Mo loading [65]. This has been attributed to large surface area and uniform pore size along with the mild acidity and high stability of NiMo/MCM-41.

Pt and Rh nanowires and nanoparticles prepared in FSM-16 display interesting catalytic properties in water-gas shift reaction [66] and hydrogenolysis of butane [67]. In hydrogenolysis of butane, Pt wire/FSM-16 demonstrates higher catalytic activity than Pt particle/FSM-16. The XANES and XPS studies show that the Pt wires are more electron deficient than particles which may cause a different catalytic activity. Similarly, Pt-Rh wire/FSM-16 displayed a high activity in butane isomerisation. Here the use of mesoporous solid is highly justified as it ensures nanowire formation and modification of its properties due to host influence. In the early studies, Schuth *et al.* found that very small Pt nanoparticles (ca. 2 nm) encapsulated within MCM-41 materials showed very high activity in the CO oxidation reactions, for which 50% conversion was reached at temperatures as low as 360 K [66]. Recently, Dai *et al.* reported that, after removing the amine ligands (*i.e.* activation), highly dispersed gold nanoparticles confined in mesoporous SBA-15 exhibited extremely high CO oxidation reactivity; 50% CO conversion was reached at temperatures as low as 253 K [69].

Corma *et al.* found that gold nanoparticles trapped in the mesoporous silica materials exhibited high catalytic activity for the solventless, aerobic oxidation of alcohols to carbonyl compounds in the absence of base. Under these conditions the solid can be recycled without losing catalytic activity and maintaining the mesoporous structure [70]. Metallic cobalt nanoparticles confined within the channels of SBA-15 materials were found to be highly active in many intermolecular cycloaddition reactions [71]. Johnson *et al.* found that monodispersed metallic/bimetallic nanoclusters confined in MCM-41 materials showed a vastly improved enatioselectivity in the hydrogenation reactions compared with the homogeneous analogues [52].

Shi *et al.* reported that ultrafine Pd nanoparticles confined in mesoporous SBA-15 were more efficient than traditional Pd catalysts in Heck coupling reactions; only one fifth of the amount of catalyst was needed to reach the same conversion under the same reaction conditions [72]. In addition, it is also found that by tuning the pore size of mesoporous silica, monodispersed silver nanoparticles with different particle size have been obtained which showed size-dependent oxygen dissociation behaviour and catalytic selectivities to formaldehyde in the methanol oxidation reactions [73].

1.5.2. Optical Properties

Semiconductor particles (metal sulphides, selenides, oxides etc.) prepared in mesoporous solids show change of optical properties of nanoparticles compared to bulk, similar to semiconductor particles prepared in any other environment. There is no specific interaction with walls of mesoporous solids which can change the optical properties in most of cases. However, if particles are prepared via CVD or high temperature treatment, mesoporous solids are the only choice for stabilization of such particles. For example, GaAs/MCM-41 show blue-shift in absorption and visible photoluminescence even at room temperature [74]. CdS nanoparticles show a change in absorption spectra after their incorporation into mesoporous silica containing thiol groups [75]. Gold nanoparticles prepared within mesoporous silica monolith showed red-shift of Mie-resonance absorption band with decreasing the Au particle size but theoretical calculations for particles of 5-20 nm embedded in nonadsorbent showed that no shift should be expected. So the optical behaviour of Au nanoparticles in the

mesoporous matrix was ascribed to the charge transfer between the Au nanoparticles and the pore walls [76]. Silver nanoparticles obtained by thermal decomposition of $AgNO_3$ within mesoporous pores show interesting optical properties [77]. Ag doping results in a large red shift of the absorption edge which is attributed to the interband adsorption of Ag in Ag-silica system and dipole interaction between Ag particles.

1.5.3. Magnetic Properties

Magnetic properties of particles strongly depend on particle size. With decrease of particle diameter, the nature of magnetism changes: ferromagnetic particles become superparamagnetic and these properties are temperature-dependent. Magnetic measurements are often used for materials containing magnetically active particles to elucidate their composition and structure. For example magnetic measurements helped to confirm the existence of a hydroxo layer on iron oxide particles formed in mesoporous alumina [78]. Iron nanoparticles prepared by pyrolysis of poly(ferrocenylsilanes) inside periodic mesoporous silica displayed the absence of room temperature hysteresis in the magnetisation curves which shows their superparamagnetic behaviour [79]. However, magnetic measurements should be combined with other techniques to allow more accurate evaluation of particle structure. Iron oxide nanoclusters (γ-Fe2O3) synthesized within mesoporous MCM-41 aluminosilicate matrices demonstrated high stability against ($\gamma \rightarrow \alpha$) phase transition [80]. The authors suggest that the high thermal stability and increased magnetisation from calcination make this material a good candidate for high-temperature magnetic applications.

1.6. PHYSICOCHEMICAL CHARACTERIZATION

Characterization of these materials involves the determination of mesoporous structure as well as metal nanoparticles. It can be done by a combination of methods used for the study of mesoporous materials as well as metal nanoparticles like XRD, N_2 adsorption, HRTEM, SEM, UV-Vis spectroscopy, FTIR spectroscopy, NMR spectroscopy and ICP technique.

1.6.1. Powder X-Ray Diffraction

It is well recognised that XRD, based on wide-angle elastic scattering of X-rays, has been the single most important tool to determine the structure of the

materials characterized by the long range ordering. The XRD patterns are obtained by the measurements of the angles at which the X-ray beam is diffracted by the sample. Bragg's equation relates the distance between two *hkl* planes *(d)* and angle of diffraction (2θ) as:

$$n\lambda = 2d \sin\theta$$

where λ = wavelength of X-rays, n= an integer known as the order of reflection (*h, k,* and *l* represent Miller indices of respective planes) [81]. From the diffraction patterns, the uniqueness of mesoporous structures [82], phase purity [83], degree of crystallinity [83] and unit cell parameters [82] of the semi crystalline hybrid materials can be determined.

The identification of phase is based on a comparison of a set of reflections of the sample with that of pure reference phases distributed by International Center for Diffraction Data (ICDD). Unit cell parameter (a_0) of a cubic lattice can be determined by the following equation: $a_0 = d_{hkl}\sqrt{(h^2 + k^2 + l^2)}$, where d=distance between two consecutive parallel planes having Miller indices *h, k,* and *l* [81].

XRD broadening analysis has been widely used to characterize supported metal crystallites in the nanoscale. The average size of nanoparticles can be estimated using Debye-Scherrer equation:

$$D = {k\lambda}/{\beta \cos\theta}$$

where D=thickness of the nanocrystal, k is a constant, λ= wavelength of X-rays, β = width at half maxima of reflection at Bragg's angle 2θ [84].

1.6.2. Adsorption Measurements

1.6.2.1. Adsorption Isotherm and BET Method

Gas adsorption measurements are widely used for determining the surface area and pore size of porous solid materials. Nitrogen is commonly used as the adsorbate at liquid nitrogen temperature. N_2 adsorption desorption isotherms of mesoporous materials (pore size 2-50 nm) are of the type IV. Characteristics features of type IV isotherms are its hysteresis loop which is associated with capillary condensation taking place in the mesopores and limiting uptake over a range of high ${p}/{p_0}$. The initial part of type IV isotherm corresponds to monolayer and multilayer adsorption [85]. Hysteresis loops may exhibit a wide variety of shapes and these often have been

identified with specific pore structures (Fig. 1.14). Type H1 is associated with uniform pores with narrow size distribution. Type H4 is given by many porous adsorbents but in these cases distribution of pore size and shape is not well defined. Type H2 and H3 may be regarded as intermediate between two extremes. The steep increase in N_2 adsorption (in the $^{p}/_{p_0}$ range of 0.2 to 0.4) corresponds to capillary condensation within uniform pores.

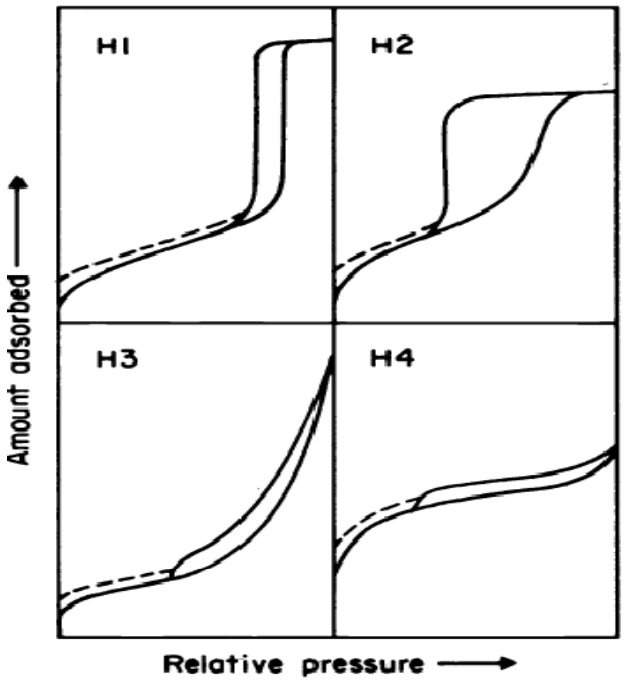

Fig. 1.14. Types of hysteresis loops. [Source: Ref. 85]

The Braunauer-Emmett-Teller (BET) volumetric gas adsorption technique using N_2 is a standard method for the determination of the surface area and pore size distribution of finely divided porous samples [86]. The simple form of this equation can be written:

$$^{p}/_{V_a}\,(p_0 - p) = {}^{1}/_{V_m}\,c + {}^{p(c-1)}/_{V_m}\,p_0 c$$

Where V_a is the volume of gas adsorbed at equilibrium pressure, p_0 is vapour pressure of gas at sample temperature and p is the absolute pressure inside the sample chamber, c is an isothermal constant that depends upon adsorbate, adsorbent and temperature and 'V_m' is the monolayer capacity of surface. By plotting $^{p}/_{V_a}\,(p_0 - p)$ vs. $^{p}/_{p_0}$ and determining V_m from the slope of the resultant straight line in the partial pressure range of 0.05 to 0.35, the surface area can be calculated.

1.6.2.2. The t- and β Plots

The *t-plot* analysis, a plot of the amount adsorbed versus the thickness of the adsorbed gas on the walls of the pores, is mostly applied to differentiate between the adsorption mechanisms in micropores, mesopores and macropores. Lippens and de Boer showed that if the multimolecular layer of adsorbed nitrogen could be formed freely on the surface, the statistical thickness, t (in nm) of the adsorbed layer could be calculated according to the equation.

$$t = 0.3538\left(V_a/V_m\right) = f_1(p/p_0)$$

If the adsorption data are presented in the form of a *t*-plot, two linear regions are obtained. The first linear region represents both micropore filling and surface coverage of larger pores. The second linear region gives the layer-by layer adsorption taking place in meso and macropores but not in micropores. The y-axis intercept multiplied by the ratio of the gas and liquid densities of the adsorbate (0.00156 for nitrogen) will provide the micropore volume in cc per gram of the solid. The slope of the second linear region gives the surface area provided by pores with radii larger than 10 Å, *i.e.*, the mesopore area. The first linear region extrapolates to the origin and the slope of this line gives the value of the total surface area of the material provided by all pores. Usually this number agrees with the BET surface area within 10-15%. Micropore volume can also be observed from the β plot also where

$$\beta = \left[\ln(0.4)/\ln(p/p_0)\right]^{1/2.7}$$

Three different regions can be seen on these plots: (i) a linear region due to multilayer adsorption in mesopores; (ii) a steep region due to capillary condensation within these mesopores; and (iii) a last linear region due to multilayer formation onto the external surface of the grains. Micropore and mesopore volumes can be obtained by the intercept between the adsorbed amount (y-axis) and the linear segments (i) and (iii). These two extrapolations give V_{micro} and (V_{micro} + V_{meso}) respectively. The β plots of SBA-15 yield non-zero V_{micro} values, thus indicating the presence of micropores.

1.6.2.3. Pore Volume and Pore Size Distribution

The total pore volume is derived from the amount of vapour adsorbed at relative pressure close to unity assuming that all the pores are filled with condensed absorptive in normal liquid state. Pore size distribution is the distribution of pore volume with respect to pore size. The computation of pore size distribution involves a number of assumptions (pore shape, mechanism of pore filling, validity of Kelvin equation etc). It is generally accepted that desorption isotherm is more appropriate than adsorption isotherm for evaluating the pore size distribution of the adsorbent. The mesopore size calculations are made assuming cylindrical pore geometry using Kelvin equation in the form:

$$r_k = \frac{-2\gamma\, V_m}{RT \ln\left({}^{p}/_{p_0}\right)}$$

Where γ= surface tension of nitrogen at its boiling point, V_m = Molar volume of liquid nitrogen, R= gas constant, T= boiling point of liquid nitrogen, ${}^{p}/_{p_0}$= relative pressure of nitrogen, r_k= the Kelvin radius of the pore. If the radius of cylindrical pore is r_p and correction is made for the thickness of a layer already adsorbed on the pore walls, i.e. the multilayer thickness, t, then

$$r_p = r_k + t$$

Several computational procedures are available for the derivation of pore size distribution of mesoporous samples from physiosorption isotherms. Among the classical macroscopic theories, most popular is the Barrett-Joyner-Halenda (BJH) model, which is based on speculative emptying of the pores by a stepwise reduction of ${}^{p}/_{p_0}$, and allowance being made for the contraction of the multilayer in those parts already emptied by the condensate [87]. The mesopore size is usually expressed as a plot of ${}^{\Delta V_p}/_{\Delta r_p}$ versus r_p , where V_p= mesopore volume, and r_p = pore radius. It is assumed that the mesopore volume is completely filled at high ${}^{p}/_{p_0}$. But classical macroscopic, theories like DR, BJH, HK etc. do not give a realistic description of the filling of micropores and even narrow mesopores. This leads to an underestimation of pore sizes. Microscopic theories like Non Local Density Functional Theory (NLDFT)

[88, 89] consider the sorption and phase behaviour of fluids in narrow pores on a molecular level. The NLDFT correctly describes the local fluid structure near curved solid walls; adsorption isotherms in the model pores are determined based on the intermolecular potentials of the fluid-fluid and solid-fluid interactions. The relation between isotherms determined by these microscopic approaches and experimental isotherm of a porous solid can be interpreted in terms of a Generalized Adsorption Isotherm (GAI) equation. The pore size distribution is then derived by solving the GAI equation numerically via a fast non-negative least square algorithm.

1.6.3. Transmission Electron Microscopy

Transmission electron microscopy (TEM) is typically used for high resolution imaging of thin sections of solid samples for nanostructural and compositional analysis. The technique involves: (i) irradiation of a very thin sample by a high energy electron beam, which is diffracted by the lattice of a crystalline or semi crystalline material and propagated along different directions, (ii) imaging and angular distribution analysis of the forward-scattered electron (unlike SEM where backscattered electrons are detected) and (iii) energy analysis of the emitted X-rays [90]. A beam of accelerated electrons can interact with an object in a conventional transmission electron microscope in one of two ways. Usually elastic scattering takes place, whereby the electrons change their path in the specimen without a loss of energy. Inelastic scattering can also occur, resulting in a loss of energy due to an interaction of the impinging electrons with the orbital electrons surrounding the nucleus of each atom in the object. Those electrons, which are not or hardly scattered, contribute positively to the image. However, considerably deflected electrons are prevented from doing so by apertures in the optical path. As a result, differences in light intensity (contrast) are created in the final image, which relate to areas in the object with different scattering potentials. As the atomic number increases, their scattering efficiency will also increase. Hence, heavy metals can form images with good contrast. The imaging system consists of an objective lens and one or more projector lenses. The chief lens in transmission microscopes is the objective. It determines the degree of resolution in the image. It forms the initial enlarged image of the illuminated portion of the specimen in a plane that is suitable for further enlargement by the projector lens. The projector lens, as it implies, serves to project the final magnified image on the screen or photographic emulsion. The great depth of

focus provides the high magnification of the sample. The topographic information obtained by TEM in the vicinity of atomic resolution can be utilized for structural characterization and identification of various phases of mesoporous materials, viz., hexagonal, cubic or lamellar [91]. TEM also provides real space image on the atomic distribution in the bulk and surface of a nanocrystal [92].

1.6.4. Scanning Electron Microscopy

Scanning electron microscopy (SEM) is one of the most widely used techniques for characterization of nanomaterials and nanostructures. The resolution of the SEM approaches a few nanometres, and the instruments can operate at magnifications that are easily adjusted from ~10 to over 300,000. This technique provides not only topographical information like optical microscopes do, but also information of chemical composition near the surface. A scanning electron microscope can generate an electron beam scanning back and forth over a solid sample. The interaction between the beam and the sample produces different types of signals providing detailed information about the surface structure and morphology of the sample. When an electron from the beam encounters a nucleus in the sample, the resultant columbic attraction leads to a deflection in the electron's path, known as Rutherford elastic scattering. A fraction of these electrons will be completely backscattered, remerging from the incident surface of the sample. Since the scattering angle depends on the atomic number of the nucleus, the primary electrons arriving at a given detector position can be used to produce images containing topological and compositional information [93]. The high-energy incident electrons can also interact with the loosely bound conduction band electrons in the sample. However, the amount of energy given to these secondary electrons as a result of the interactions is small, and so they have a very limited range in the sample. Hence, only those secondary electrons that are produced within a very short distance from the surface are able to escape from the sample. As a result, high-resolution topographical images can be obtained in this detection mode [94].

1.6.5. UV-Visible Spectroscopy

It deals with the study of electronic transitions between orbitals or bands of atoms, ions or molecules in gaseous, liquid and solid state. In the case of transition metal ions or atoms, any change in their coordination sphere may affect their optical

properties and therefore can be characterized by UV-Vis [95]. The metallic nanoparticles are known to exhibit different characteristic colours. Mie was the first to explain the origin of this colour theoretically in 1908 by solving Maxwell's equation for the absorption and scattering of electromagnetic radiation by small nanoparticles [96]. This absorption of electromagnetic radiation by metallic nanoparticles originates from the coherent oscillation of the valence band electrons induced by an interaction with the electromagnetic field [97]. These resonances are known as surface plasmons, which occur only in case of nanoparticles and not in case of bulk metallic particles [98]. Hence, UV-Visible spectroscopy can be utilized to study the unique optical properties of the hybrid mesoporous materials containing occluded metallic nanoparticles, exploiting the size- and shape dependent surface plasmon resonance [99].

1.6.6. Fourier Transform Infrared Spectroscopy

Fourier transform infrared (FTIR) spectroscopy deals with the vibration of chemical bonds in a molecule at various frequencies depending on the elements and types of bonds. After absorbing electromagnetic radiation the frequency of vibration of a bond increases leading to transition between ground state and several excited states. These absorption frequencies represent excitations of vibrations of the chemical bonds and thus are specific to the type of bond and the group of atoms involved in the vibration. The energy corresponding to these frequencies correspond to the infrared region (4000–400 cm^{-1}) of the electromagnetic spectrum. The term Fourier transform (FT) refers to a recent development in the manner in which the data are collected and converted from an interference pattern to an infrared absorption spectrum that is like a molecular "fingerprint"[100].

1.6.7. Nuclear Magnetic Resonance Spectroscopy

Nuclear magnetic resonance (NMR) spectroscopy is one of the most powerful tools to investigate structure and dynamics of a molecular system in liquid phase. Atomic nuclei consisting of odd number of protons and/or neutrons possessing a nuclear spin $I \neq 0$ and consequently a magnetic moment $\mu = \gamma\hbar I$ (γ = gyromagnetic ratio), when placed in a magnetic field of strength B_0, Zeeman interaction results in quantized orientations of the nuclear magnetic moments [101]. The nucleus can adopt $2I + 1$ Eigen states with energies $E(m) = -m\gamma\hbar B_0$, where m = (I, I–1,…., –I).

Transitions between neighbouring energy states ($\Delta m = \pm 1$) can be induced by electromagnetic radiation (energy $E = h\nu$) of frequency $\nu_0 = \gamma B_0/2\pi$. The chemical shift interaction arises from secondary local magnetic fields induced by the interaction of the electrons surrounding the nucleus. The induced local field opposes B_0 and hence shields the nucleus under observation. The shielding is spatially anisotropic due to the nonspherical electron distribution around the nucleus [102].

1.6.8. Inductively Coupled Plasma-Optical Emission Spectroscopy

Inductively coupled plasma-optical emission spectroscopy (ICP-OES) is an analytic technique which is used to determine metal content in solid or liquid samples. In plasma emission spectroscopy (OES), a sample solution is introduced into the core of inductively coupled argon plasma, which generates temperature of approximately 8000°C. At this temperature all elements become thermally excited and emit light at their characteristic wavelengths. This light is collected by the spectrometer and passes through a diffraction grating that serves to resolve the light into a spectrum of its constituent wavelengths. Within the spectrometer, this diffracted light is then collected by wavelength and amplified to yield an intensity measurement that can be converted to an elemental concentration by comparison with calibration standards. In metal containing mesoporous silica, material is dissolved by treating with hydrofluoric acid and aqua regia and metal content is determined by analysing these solutions.

1.7. SCOPE AND OBJECTIVE OF THESIS

Nanocatalysis is the oldest form of heterogeneous catalysis. Shape and size of nanoparticles can play an important role in controlling the selectivity in a reaction. There are various methods described in literature for the synthesis of monodispersed metal nanoparticles in terms of shape and size in colloidal solutions but they have limited use in catalysis. Mesoporous materials are advantageous as supports due to their interpenetrating channels and high surface area; moreover, they provide thermal stability to the metal nanoparticles when completely isolated within the channels. Also, the fact that the pore dimensions and pore characteristics can be easily fine tuned makes them more attractive for engineering the size, morphology and electronic properties of the encapsulated nanoparticles. Methods currently employed vary from conventional impregnation to sophisticated post synthesis modifications. However,

there is still scope for improvement in overall particle dispersity, control of size and localization. At this juncture, it would be worthwhile exploring direct and simpler methodologies for localizing metal nanoparticles predominantly within the mesochannels while retaining high surface areas and pore volumes – ideal for catalysis amongst other applications. In this context, present thesis describes a novel *in situ* method for synthesizing metal nanoparticles with narrow size distribution in the mesoporous channels of SBA type materials.

Specific problems chosen are:

(i) *In situ* synthesis of Pt, Au and Pt-Au nanoparticles in the mesoporous channels of SBA-15.

(ii) Fine tuning of size and morphology of Pt nanoparticles in channels of SBA type materials.

(iii) Mechanistic study of the formation of Pt particles of various size and morphology in mesoporous silica channels using various techniques like *in situ* XRD, *in situ* UV-Vis studies, FTIR and NMR spectroscopy.

(iv) Effect of size of Pt nanoparticles present in mesoporous channels in size sensitive reactions like CO oxidation and cinnamaldehyde hydrogenation.

1.8. REFERENCES

1. G. C. Bond, *Catalysis by metals,* Academic Press, London, 1962.

2. H. S. Taylor, *Proc. R. Soc. Lond. A.* **1925**, *108*, 105.

3. J. Grunes, J. Zhu, G. A. Somorjai, *Chem. Commun.* **2003**, 2257.

4. F. Delbecq, P. J. Sautet, *J. Catal*. **1995**, *152*, 217.

5. P. Gallezot, D. Richard, *Catal. Rev.-Sci. Eng*. **1998**, *40*, 81.

6. G. A. Somorjai, J. W. Park, *Angew*. *Chem.*, *Int. Ed.* **2008**, *47*, 9212.

7. J. Liu, *Microsc. Microanal.* **2003**, *9 (Suppl 2)*, 290.

8. R.-J. Liu, P. A. Crozier, C. M. Smith, D. A. Hucul, J. Blackson, G. Salaita *Microsc. Microanal.* **2004**, *10(Suppl 2)*, 488.

9. R. S. Goeke, A. K. Datye, *Top. Catal.* **2007**, *46*, 3.

10. A. K. Datye, Q. Xu, K. C. Kharas, J. M. McCarty, *Catal. Today* **2006**, *111*, 59.

11. G. A. Somorjai, Y. G. Borodko, *Catal. Lett.* **2001**, *76*, 1.

12. R. M. Rioux, H. Song, M. Grass, S. Habas, K. Niesz, J. D. Hoefelmeyer, P. Yang, G. A. Somorjai, *Top. Catal.* **2006**, *39,* 167.

13. L. Guczi, G. Peto, A. Beck, Z. Paszti, *Top. Catal*. **2004**, *29*, 129.

14. V. F. Puntes, K. M. Krishnan, A. P. Alivisatos, *Science* **2001**, *291*, 2115.

15. Y. Xiong, Y. Xia, *Adv. Mater.* **2007**, *19*, 3385.

16. Y. Xiong, J. Chen, B. Wiley, Y. Xia, S. Aloni, Y. Yin, *J. Am. Chem. Soc.* **2005**, *127*, 7332.

17. Y. Xiong, H. Cai, B. J. Wiley, J. Wang, M. J. Kim, Y. Xia, *J. Am. Chem. Soc.* **2007**, *129*, 3665.

18. B. Wiley, Y. Sun, B. Mayers, Y. Xia. *Chem.--Eur. J.* **2005**, *11*, 454.

19. S. S. Shankar, A. Rai, B. Ankamwar, A. Singh, A. Ahmad, M. Sastry, *Nat. Mater.* **2004**, *3*, 482.

20. P. Mukherjee, A. Ahmad, D. Mandal, S. Senapati, S. R. Sainkar, M. I. Khan, R. Ramani, R. Pasricha, P. V. Ajaykumar, M. Alam, M. Sastry, R. Kumar, *Angew. Chem., Int. Ed*. **2001**, *40*, 3585.

21. C. T. Kresge, M. E. Leonowicz, W. J. Roth, J. C. Vartuli, J. S. Beck, *Nature* **1992**, *354*, 710.

22. a) D. Y. Zhao, J. Feng, Q. Huo, N. Melosh, H. G. Fredrickson, B. F. Chmelka, G. D. Stucky, *Science* **1998**, *279*, 548. b) D. Y. Zhao, Q. Huo, J. Feng, B. F. Chmelka, G. D. Stucky, *J. Am. Chem. Soc.* **1998**, *120*, 6020.

23. J. D. Epping, B. F. Chmelka, *Curr. Opin. Colloid Interface Sci.* **2006**, *11,* 81.

24. K. Flodstrom, C. V. Teixeira, H. Amenitsch, V. Alfredsson, M. Linden, *Langmuir,* **2004**, *20*, 4885.

25. G .J. de, A. A. Soler-Illia, C. Sanchez, B. Lebeau, J. Patarin. *Chem. Rev.* **2002**, *102*, 4093.

26. Y. Wan, D. Zhao, *Chem. Rev.* **2007**, *107*, 2821.

27. A. Firouzi, D. Kumar, L. M. Bull, T. Besier, P. Sieger, Q. Huo, S. A. Walker, J. A. Zasadzinski, C. Glinka, J. Nicol, D. Margolese, G. D. Stucky, B. F.

Chmelka, *Science* **1995**, *267*, 1138.

28. S. Forster, M. Antonietti, *Adv. Mater.* **1998**, *10*, 195.

29. L. M. Bronstein, *Top. Curr. Chem.* **2003**, *226*, 55.

30. J. Sun, X. Bao, *Chem.--Eur. J.* **2008**, *14*, 7478.

31. Y. Plyuto, J.-M. Berquier, C. Jacquiod, C. Ricolleau, *Chem. Commun.* **1999**, 1653.

32. M. H. Huang, A. Choudrey, P. Yang, *Chem. Commun.* **2000**, 1063.

33. S.-W. Kim, S. U. Son, S. I. Lee, T. Hyeon, Y. K. Chung, *J. Am. Chem. Soc.*, **2000**, *122*, 1550.

34. Y. Guari, C. Thieuleux, A. Mehdi, C. Reye, R. J. P. Corriu, S. Gomez-Gallardo, K. Philippot, B. Chaudret, R. Dutartre, *Chem. Commun.* **2001**, 1374.

35. P. Mukherjee, C. R. Patra, R. Kumar, M. Sastry, *PhysChemComm.* **2001**, *5*, 1.

36. C. -m. Yang, H. -s. Sheu, K. -j. Chao, *Adv. Funct. Mater.* **2002**, *12*, 143.

37. Z. Konya, V. F. Puntes, I. Kiricsi, J. Zhu, J. W. Ager, III, M. K. Ko, H. Freil, P. Alivisatos, G. A. Somorjai, *Chem. Mater.* **2003**, *15*, 1242.

38. J. Zhu, Z. Konya, V. F. Puntes, I. Kiricsi, C. X. Miao, J. W. Ager, A. P. Alivisatos, G. A. Somorjai, *Langmuir* **2003**, *19*, 4396.

39. H. Song, M. R. Rioux, D. J. Hoefelmeyer, R. Komor, K. Niesz, M. Grass, P. Yang, G. A. Somorjai, *J. Am. Chem. Soc.* **2006**, *128*, 3027.

40. R. M. Rioux, H. Song, J. D. Hoefelmeyer, P. Yang, G. A. Somorjai, *J. Phys. Chem. B* **2005**, *109*, 2192.

41. Z. Konya, E. Monar, G. Tasi, K. Niesz, G. A. Somorjai, I. Kiricsi, *Catal. Lett.* **2007**, *113*, 19.

42. J. Y. Ying, C. P. Mehert, M. S. Wong, *Angew. Chem., Int. Ed* **1999**, *38*, 56.

43. M. S. Morey, J. D. Bryan, S. Schartz, G. D. Stucky, *Chem. Mater.* **2000**, *12*, 3435.

44. J. Liu, X. Feng, G. E. Fryxel, L-Q Wang, A. Y. Kim, M. Gong, *Adv. Mater.* **1998**, *10*, 161.

45. H. Shi, L. Zhang, W. Cai, *J. Appl. Phys.* **2000**, *87*, 1572.

46. K. W. Powers, L. L. Hench, *Ceram. Trans.* **2000**, *101*, 253.

47. K. Moller, T. Bein, *Chem. Mater.* **1998**, *10,* 295.

48. J. J. Schnider, N. Czap, J. Hagen, J. Engstler, J. Ensling, P. Gütlich, U. Reinoehl, H. Bertagnolli, F. Luis, L. J. de Jongh, M. Wark, G. Grubert, G. L. Hornyak, R. Zanoni, *Chem.--Eur. J.* **2000**, *6*, 4305.

49. J-S Jung, W-S Chae, R. A. McIntyre, C. T. Seip, J. B. Wiley, C. J. O'Connor, *Mater. Res. Bull.* **1999**, *34*, 1353.

50. W. W. Pai, A. K. Swan, Z. Zhang, J. F. Wendelken, *Phys. Rev. Lett.* **1997**, *79*, 3210.

51. R. A. Dixon, R. G. Egdell, *J. Chem. Soc., Faraday Trans.* **1998**, *94*, 1329.

52. R. T. K. Baker, P. S. Harris, R. B. Thomas, *Surf. Sci.* **1974**, *46*, 311.

53. J. P. Gabaldon, M. Bore, A. K. Datye, *Top. Catal.* **2007**, *44*, 253.

54. F. G. Johnson, *Top. Catal.* **2003**, *24,* 147.

55. A. Fukuoka, J.-I. Kimura, T. Oshio, Y. Sakamoto, M. Ichikawa, *J. Am. Chem. Soc.* **2007**, *129*, 10120.

56. C. M. Yang, P. H. Liu, Y. Ho, C. Chiu, K. Chao, *Chem. Mater.* **2003**, *15*, 275.

57. H. G. Zhu, C. D. Liang, W. F. Yan, S. H. Overbury, S. Dai, *J. Phys. Chem. B* **2006**, *110*, 10842.

58. I. Yuranov, L. Kiwi-Minsker, P. Buffat, A. Renken, *Chem. Mater.* **2004**, *16*, 760.

59. S.-W. Kim, S. U. Son, S. I. Lee, T. Hyeon, Y. K. Chung, *J. Am. Chem. Soc.* **2000**, *122*, 1550.

60. J. C. Vartuli, S. S. Shih, C. T. Kresge, J. S. Beck, *Stud. Surf. Sci. Catal.* **1998**, *117*, 13.

61. K. J. Del Rossi, G. H. Hatzikos, A. Jr. Huss **(1993)** US Pat 5245101, Chem Abs CAN 119:274, 893.

62. C. P. Mehnert, D. W. Weaver, J. Y. Ying, *J. Am. Chem. Soc.* **1998**, *120,* 289.

63. M. Chatterjee, T. Iwasaki, Y. Onodera, T. Nagase, *Catal. Lett.* **1999**, *61*, 99.

64. D. S. Shephard, *Stud. Surf. Sci. Catal.* **2000**, *129*, 789.

65. A. Corma, A. Martinez, V. Martinez-Soria, J. B. Monton, *J. Catal.* **1995**, *153*, 25.

66. A. Fukuoka, N. Higashimoto, Y. Sakamoto, M. Sasaki, N. Sugimoto, S Inagaki, Y. Fukushima, M. Ichikawa, *Catal. Today,* **2001**, *66*, 23.

67. A. Fukuoka, N. Higashimoto, Y. Sakamoto, S. Inagaki, Y. Fukushima, M. Ichikawa, *Micropor. Mesopor. Mater.* **2001**, *48*, 171.

68. U. Junges, W. Jacobs, I. Voigt-Martin, B. Krutzsch, F. Schuth, *J. Chem. Soc., Chem. Commun.* **1995**, 2283.

69. H. G. Zhu, C. D. Liang, W. F. Yan, S. H. Overbury, S. Dai, *J. Phys. Chem. B* **2006**, *110*, 10842.

70. C. Aprile, A. Abad, H. GarcVa, A. Corma, *J. Mater. Chem.* **2005**, *15*, 4408.

71. S.-W. Kim, S. U. Son, S. I. Lee, T. Hyeon, Y. K. Chung, *J. Am. Chem. Soc.* **2000**, *122*, 1550.

72. L. Li, J. L. Shi, L. X. Zhang, L. M. Xiong, J. N. Yan, *Adv. Mater.* **2004**, *16*, 1079.

73. X. H. Bao, unpublished results.

74. V. I. Srdanov, I. Alxneit, G. D. Stucky, C. M. Reaves, S. P. Den Baars, *J. Phys. Chem. B* **1998**, *102,* 3341.

75. T. Hirai, H. Okubo, I. Komasawa, *J. Colloid Interface Sci.* **2001**, *235*, 358.

76. L. Zhang, W. Cai, C. Mo, *Prog. Natur. Sci.* **1999**, *9*, 401.

77. C. Weiping, Z. Lide, *J. Phys.: Condens. Matter* **1997**, *9*, 7257.

78. J. J. Schnider, N. Czap, J. Hagen, J. Engstler, J. Ensling, P. Gütlich, U. Reinoehl, H. Bertagnolli, F. Luis, L. J. de Jongh, M. Wark, G. Grubert, G. L. Hornyak, R. Zanoni, *Chem.--Eur. J.* **2000**, *6*, 4305.

79. M. J. MacLachlan, M. Ginsburg, N. Coombs, N. P. Raju, J. E. Greedan, G. A. Ozin, I. Manners, *J. Am. Chem. Soc.* **2000**, *122*, 3878.

80. L. Zhang, C. Papaefthymiou, J. Y. Ying, *J. Phys. Chem. B* **2001**, *105*, 7414.

81. W. H. Bragg, W. L. Bragg, *The Crystalline State, Vol. 1*, McMillan, New York, 1949.

82. S. Biz, M. Occelli, *Catal. Rev. –Sci. Eng.* **1998**, *40*, 329.

83. G. Bergeret, in: *Handbook of Heterogeneous Catalysis, Vol. 2,* Eds: G. Ertl, H. Knozinger, J. Weitkamp, Wiley-VCH, Weinheim, 1977, pp. 464-475.

84. R. C. Rau, in: *Advances in X-Ray Analysis, Vol. 5,* Ed: W. M. Mueller, Sir Isaac Pitman and Sons Ltd., London, 1962, pp. 104-106.

85. K. S. W. Sing, D. H. Everett, R. A. W. Haul, l. Moscou, R. A. Pierotti, J. Rouquerol, T. Siemieniewska, *Pure & App. Chem., Vol. 57, No. 4,* pp. 603—619, 1985.

86. S. Braunauer, P. H. Emmett, E. Teller, *J. Am. Chem. Soc.* **1938**, *60*, 309.

87. E. P. Barrett, L. G. J oyner, P. P. Halenda, *J. Am. Chem. Soc.* **1951**, *73*, 373.

88. R. Evans, U. M. B. Marconi, P. Tarzona, *J. Chem. Soc., Faraday Trans. II* **1986**, *82*, 1763.

89. P. I. Ravikovitch, G. L. Haller, A. V. Neimark, *Adv. Colloid Interfac.* **1998**, *203*, 76.

91. J. R. Fryer, *Chemical Applications of Transmission Electron Microscopy*, Academic Press, San Diego, 1979.

91. a) J. M .Thomas, O. Terasaki, P. L. Gai, W. Zhou, J. Gonzalez-Calbet, *Acc. Chem. Res.* **2001**, *34,* 583. b) V. Alfredsson, M. Keung, A. Monnier, G. D. Stucky, K. K. Unger, F Schuth, *J. Chem. Soc., Chem. Commun.* **1994**, 921.

92. Z. L. Wang, in: *Characterization of Nanophase Materials,* Ed: Z. L. Wang, Wiley-VCH, Weinheim, 2000, Chapter 3, pp. 37-80.

93. G. Lawes, *Scanning Electron Microscopy and X-ray Microanalysis*, John Wiley and Sons Ltd., Chichester, 1987.

94. D. E. Newbury, D. C. Joy, P. Echlin, C. E. Fiori, J. I. Goldstein, *Advanced Scanning Electron Microscopy and X-ray Microanalysis*, Plenum Press, New York, 1986.

95. C. K. Jorgensen, *Absorption Spectra and Chemical Bonding in Complexes*, Pergamon, New York, 1962.

96. G. Mie, *Ann. Physik* 1908, *25*, 377.

97. M. Faraday, *Philos. Trans.* 1857, *147*, 145.

98. G. C. Papavassiliou, *Prog. Solid State Chem.* **1980**, *12*, 185.

99. a) S. Link, M. A. El-Sayed, *J. Phys. Chem. B* **1999**, *103*, 4212. b) C. Burda, T. Green, C. Landes, S. Link, R. Little, J. Petroski, M. A. El-Sayed, in: *Characterization of Nanophase Materials*, Ed: Z. L. Wang, Wiley-VCH, Weinheim, 2000, Chapter 7, pp. 197–241.

100. P. R. Griffiths, J. A. De Haseth, *Fourier Transform Infrared Spectrometry*, John Wiley and Sons Inc., New York, 1986.

101. F. A. Rushworth, D. P. Tunstall, *Nuclear Magnetic Resonance*, Gordon and Breach Science Publishers Ltd., London, 1973.

102. W. W. Paudler, *Nuclear Magnetic Resonance: General Concepts and Applications*, John Wiley and Sons Inc., New York, 1987.

CHAPTER 2

IN SITU SYNTHESIS OF METAL NANOPARTICLES IN MESOPOROUS SBA-15

2.1. INTRODUCTION

The advent of mesoporous materials like SBA-15, MCM-41 [1-3] etc. has led to exciting forays into their utilization as supports for metal nanoparticles [4-6]. The advantage of using these mesoporous solids as supports is that they provide high surface area, interpenetrating channel system where particles can be stabilized against sintering at high temperatures and also facilitate better flow of reactants and products through the channels without any diffusion limitations. There are several methods reported in literature for synthesizing metal nanoparticles using mesoporous solids as support [7-13] but all these methods are disadvantageous in one way or other as described in chapter 1 (section 1.4).

In our attempt to have better control over size and morphology of metal particles, we have developed a very simple, direct and convenient *in situ* method for synthesizing metal particles in the mesoporous channels of SBA-15 materials [14]. We selected SBA-15 since it is known to have comparatively thicker walls and better hydrothermal stability compared to other mesoporous systems. SBA-15 is synthesized using nonionic triblock copolymer as template. Extensive studies on the mechanism of formation of SBA-15 suggest that hydrophobic core of the micelle and tetraethylorthosilicate (TEOS) interact initially and subsequent synthesis in the corona leads to microporous silica walls. In conventional *in situ* method for the synthesis of metal particles in SBA-15 generally the metal salts viz $H_2PtCl_4.6H_2O$, $HAuCl_4.H_2O$ etc. are added to the aqueous solution of template but this leads to the uncontrolled growth of metal particles on the walls since no preventive measures are taken to ensure that the metal precursors are solely isolated within the channels. This is because the uncharged components of the nonionic micelle do not provide any anchoring to the charged metal salts. The strategy we used to overcome this problem is to make the nonionic copolymer micelle charged by adding some ionic surfactant like cetyltrimethylammonium bromide (CTAB) and sodium dodecyl sulphate. This will provide incentive for the oppositely charged metal precursor to stay anchored in the template corona because of electrostatic interaction and finally to get encapsulated inside the mesoporous channels after the addition of silica. We have synthesized Pt, Au and Pt-Au nanoparticles in SBA-15 mesoporous material using this method. Cationic surfactant CTAB is added to the aqueous solution of triblock copolymer P123 to disperse the negative charged metal precursors in polymer corona since this

surfactant forms mixed micelle with polymer in such a way that surfactant hydrocarbon chain remain embedded in the PPO core and positive head in the hydrophilic PEO corona. Salts of these metals i.e. $H_2PtCl_6.6H_2O$ and $HAuCl_4.H_2O$ which have metal ion present in the negatively charged coordinating sphere of the compounds are taken as precursor. Negatively charged metal salt precursor gets dispersed in the mixed micelle composite of CTAB and P123 because of electrostatic interaction with the positive head of CTAB and results in the formation of ion pair. When silica precursor is added to acidic solution of metal precursor mixed micelle composite, it condenses around the composite and forms silica wall after the hydrothermal treatment. This on calcination gives fairly monodispersed metal particles mostly in the mesoporous channels of SBA-15.

2.2. SYNTHESIS

2.2.1. Synthesis of SBA-15 with Different Amounts of CTAB in Polymer P123

SBA-15 was first prepared using polymer-surfactant composite with varying concentrations of CTAB. The final molar composition of the gel used was 1 TEOS : 585 H_2O : 6.3 HCl : 0.017 P123 : 0.01- 0.32 CTAB. Typically, CTAB (Aldrich) was added to 100 g of 1 wt% solution of triblock copolymer Pluronic P123 (Aldrich) and this mixture was stirred for 24 h at room temperature. This solution was made acidic (pH < 2) by adding 6 g of conc. HCl (37%) (Loba Chemie) and 2.08 g of TEOS (Aldrich) was added after 3 h under stirring. Stirring was continued for another 24 h at 40^oC and then autoclaved at 100^oC for 48 h. The product was filtered, washed and dried at 70^oC for 24 h. The as-synthesized material was calcined to remove the polymer and surfactant by heating with a rate of 0.8^oC/min from room temperature to 450^oC under nitrogen flow. Then temperature was increased to 500^oC with the same heating rate under air flow and material was kept at this temperature for 12 h. The CTAB concentration was progressively increased to 32 mM in 1 wt% P123 for different samples.

2.2.2. Synthesis of Pt/SBA-15, Au/SBA-15 and Pt-Au/SBA-15

Typically, CTAB was added to 100 g of 1 wt% solution of P123 so that the final composition was 1 mM of CTAB and this mixture was stirred for 24 h at room temperature. For Pt incorporation, 2.6 mL of 0.019 M solution of $H_2PtCl_6.6H_2O$

(Aldrich) was added to the polymer–surfactant composite solution and stirred for 24 h at 40°C. This solution was made acidic (pH < 2) by conc. HCl (37%) and 2.08 g of TEOS was added under stirring. Stirring was continued for another 24 h at 40^{o}C and then autoclaved at 100^{o}C for 48 h. The final molar composition of the gel was 1 TEOS : 585 H_2O : 6.3 HCl : 0.017 P123 : 0.01 CTAB : 0.005 H_2PtCl_6. The product was filtered, washed, dried and calcined by the same procedure as mentioned in section 2.2.1. For Au/SBA-15, 3.58 mL of 0.027 M solution of $HAuCl_4.H_2O$ (Aldrich) was added in place of $H_2PtCl_6.6H_2O$. The rest of the procedure was same as mentioned above in this section. The final molar composition of the gel was 1 TEOS : 585 H_2O : 6.3 HCl : 0.017 P123 : 0.01 CTAB : 0.01 $HAuCl_4$. Similarly, for Pt-Au/SBA-15, a mixture of 1.30 mL of 0.019 M solution of $H_2PtCl_6.6H_2O$ and 1.79 mL of 0.027 M sol. of $HAuCl_4.H_2O$ were added. Rest of the procedure was same as mentioned above. The final molar composition of the gel was 1 TEOS : 585 H_2O : 6.3 HCl : 0.017 P123 : 0.01 CTAB : 0.0025 H_2PtCl_6 : 0.005 $HAuCl_4$.

2.3. INSTRUMENTS FOR CHARACTERIZATION

Various physico-chemical techniques like powder X-ray diffraction (XRD), N_2 adsorption, high resolution transmission electron microscopy (HRTEM), scanning electron microscopy (SEM), UV-Vis spectroscopy and inductively coupled plasma spectroscopy (ICP) were used for characterizing the metal containing mesoporous materials. Specifications of the instruments used for these characterization is described below. This section holds good for all the experiments in the other chapters also until and unless specified.

2.3.1. Powder X-Ray Diffraction

All the samples were characterized using a PANalytical X'pert Pro dual goniometer diffractometer. A proportional counter detector was used for low angle experiments and an X'celerator solid state detector was employed in wide angle experiments. The radiation used was Cu Kα (1.5418 Å) with a Ni filter and the data collection was carried out using a flat holder in Bragg-Brentano geometry (0.5 to 5º; 0.2º/min). Care was taken to avoid sample displacement effects. Variable temperature *in situ* XRD experiments were carried out in an Anton-Paar XRK900 (Fig. 2.1) reaction chamber under gas flow.

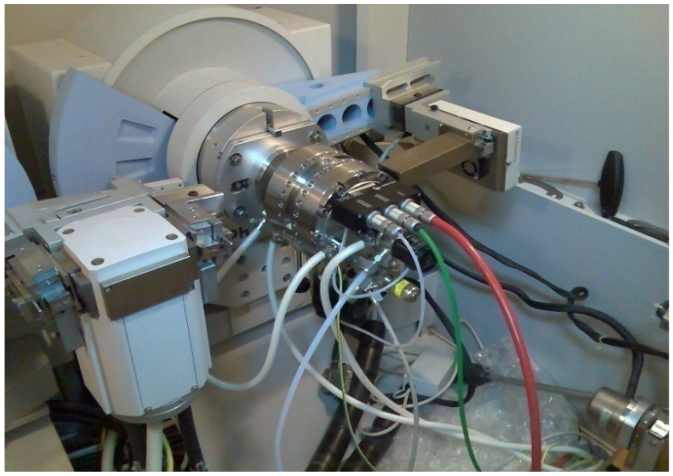

Fig. 2.1. Anton-Paar XRK-900 reaction chamber

2.3.2. N_2 Adsorption

Nitrogen adsorption/desorption isotherms were acquired using a Micromeritics ASAP 2020 instrument and Autosorb 1C Quantachrome USA. The program consisting of both an adsorption and desorption branch and typically ran at -196°C after samples were degassed at 250°C for 2 h. Specific surface areas were calculated via the BET model at relative pressures of $P/P_o = 0.06 – 0.3$. The total pore volume was estimated from the uptake of adsorbate at a relative pressure of $P/P_o = 0.99$. Pore size distribution curves were obtained via the NLDFT model assuming cylindrical pore geometry and the micropore volume calculated via t-plot analyses as a function of relative pressure using the Broekhoff de Boer model for thickness curve measured between 3.5 – 5.0 Å.

2.3.3. High Resolution Transmission Electron Microscopy

A JEOL JEM-3010 and Tecnai (Model F30) both operating at 300 kV were used for HRTEM sample observation. Some samples were also observed in T20STWIN with thermionic gun operating at 200 kV. Samples were crushed and dispersed in isopropanol with low power sonication before putting a drop over carbon coated Cu grid for observation.

2.3.4. Scanning Electron Microscopy

The scanning electron micrographs of the samples were obtained in dual beam scanning electron microscope (FEI company, model Quanta 200 3D) operating at 30

kV. The samples were loaded on stubs and sputtered with thin gold film to prevent surface charging and also to protect from thermal damage due to electron beam.

2.3.5. UV-Visible Spectroscopy

UV-Vis spectral data were acquired using a Perkin-Elmer Lambda 650 spectrometer. Samples were finely grinded and placed in sample holder and $BaSO_4$ was taken as reference. UV spectra were recorded after making instrument autozero with $BaSO_4$. Variable temperature experiments were carried out in high temperature reaction chamber (Fig. 2.2) in the Praying Mantis Diffuse Reflectance attachment (Harrick Scientific Inc.) under gas flow.

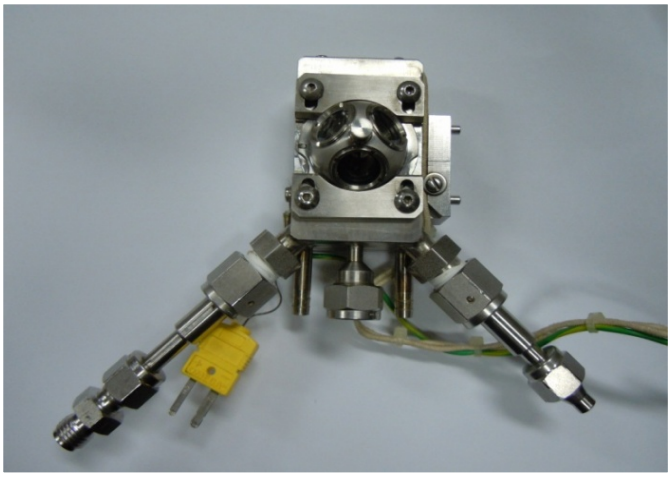

Fig. 2.2. High temperature reaction chamber for UV-Visible studies.

2.3.6. Inductively Coupled Plasma Spectroscopy

Chemical analysis was carried out in a LabTam 8440 Plasma lab sequential mode ICP-AES spectrometer and a Spectro Arcos ICP-OES instrument. Standard solutions were used for calibration purpose. In case of Pt or Au containing mesoporous SBA-15 materials, 0.05 g was taken in the polypropylene bottle. 0.5 mL of hydrofluoric acid and 0.5 mL of water was added to it. The mixture was heated at 80^oC up to dryness. Then, 1 mL of aqua regia was added to it and contents were heated at 80^oC till dryness. 10 g of water was added and solution was recovered. Later, it was made up to 25 mL and then analyzed for metal content by ICP.

2.4. CHARACTERIZATION OF SBA-15 AND Pt/SBA-15

2.4.1. Effect of Different Concentrations of CTAB on Mesoporous Order of SBA-15

Triblock copolymer P123 is known to form mixed micelles with ionic surfactants like CTAB and SDS in aqueous solution. When ionic surfactants are added to PEO-PPO-PEO block copolymer micellar system, three concentration regimes are observed denoted as low, intermediate and high concentration [15-19]. At lower surfactant concentrations (<1-2 mM) association with block copolymer micelle occurs via noncooperative binding of surfactant monomers and a large copolymer rich complex is formed, which becomes more charged as more surfactant molecules are added to the system. The binding of surfactant monomers can be considered as solubilization of the hydrocarbon chains of surfactants into PPO cores of the copolymer micelle. Here an increased interaction between the complexes with increasing surfactant concentration is observed. In the intermediate concentration regime two coexisting complexes are found "P123 micelle-surfactant complex" and "surfactant-P123" complex. The later one consists of one or more P123 unimers and a few surfactant monomers. As the surfactant concentration further increases, the smaller surfactant complexes grow in number until all unimers have been "peeled off" the large complexes. At higher concentrations, the P123 micelles are broken up and only the "surfactant–P123" complex, that is slightly smaller than a surfactant micelle exists [16]. Selection of the cooperative composite structure is crucial, since at low concentrations, addition of surfactant does not disturb the overall micelle structure and hence ensures the formation of the desired mesoporous material with continued long range order. Since a well structured P123 micelle is desirable for the formation of mesoporous SBA-15, we resorted to optimize the concentration of CTAB which will give final ordered mesoporous material.

For this purpose we synthesized SBA-15 with different concentrations of CTAB varying from 1 mM to 32 mM in 1 wt% P123. These materials have been characterized by XRD, N_2 adsorption and SEM.

2.4.1.1. Powder X-Ray Diffraction

SBA-15 was synthesized with varying amounts of the CTAB in the polymer P123 and XRD studies were carried out to follow the effect on mesoporous order. Fig.

2.3 indicates a clear effect of the surfactant on the P123 micelle and hence the mesoporous structure. At 1 mM CTAB, the mesoporous structure with long range order remained intact as shown by the higher angle peaks, albeit with a negligible contraction. However, as CTAB concentration was increased to 4 mM, there was a contraction of the unit cell and the long range order started decreasing. Any further increase in CTAB concentration resulted in a collapse of the structure since the micellar structure was completely destroyed. This observation is in direct correlation to the variations in the P123 micelle structure due to its interaction with CTAB. As CTAB concentration increases, hydrophobic nature of the core enhances leading to shrinkage of the micelle. This in turn leads to a decrease in the unit cell of the resulting mesoporous compound. Further increase in CTAB concentration and subsequent deterioration of micelle structure leads to a decrease in mesoporous order and complete collapse of the mesoporous structure.

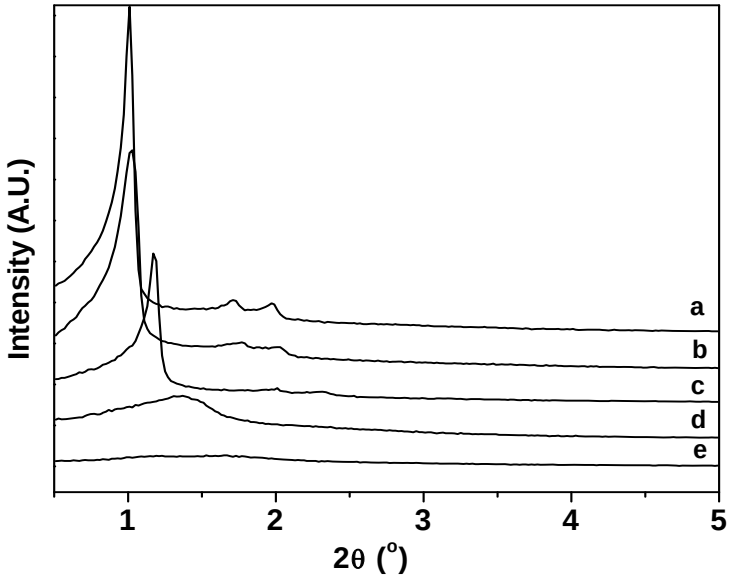

Fig. 2.3. Comparison of XRD patterns of SBA-15 synthesized with 1 wt% P123 and varying amounts of CTAB; a) no CTAB, b) 1 mM CTAB, c) 4 mM CTAB, d) 16 mM CTAB and e) 32 mM CTAB.

2.4.1.2. N_2 Adsorption Studies

All mesoporous SBA-15 materials show type IV isotherms which are the characteristics of mesoporous solids (Fig. 2.4). SBA-15 synthesized without CTAB and with 1 mM CTAB show much steep rise in hysteresis region of isotherm indicating narrow distribution of pore size (Fig. 2.4 left). Decrease in steepness of hysteresis after 4 mM onwards shows wider distribution of pore size also clear from

Fig. 2.5. N_2 adsorption studies also show that there is a decrease in pore size with increase in CTAB concentration (Table 2.1). As described earlier, cationic surfactant breaks up the polymer micelles when their concentration is increased in the P123. This means that the volume of the hydrophobic surfactant chain of P123 decreases continuously by addition of cationic surfactant. Hence the decrease in pore size with increase in CTAB concentration is obvious since it is the radii of hydrophobic PPO core which determines the pore size of the mesoporous material. However, the surface area calculated by BET equation seems to show no trend. This may be due to amorphous high surface area silica which is present in the samples.

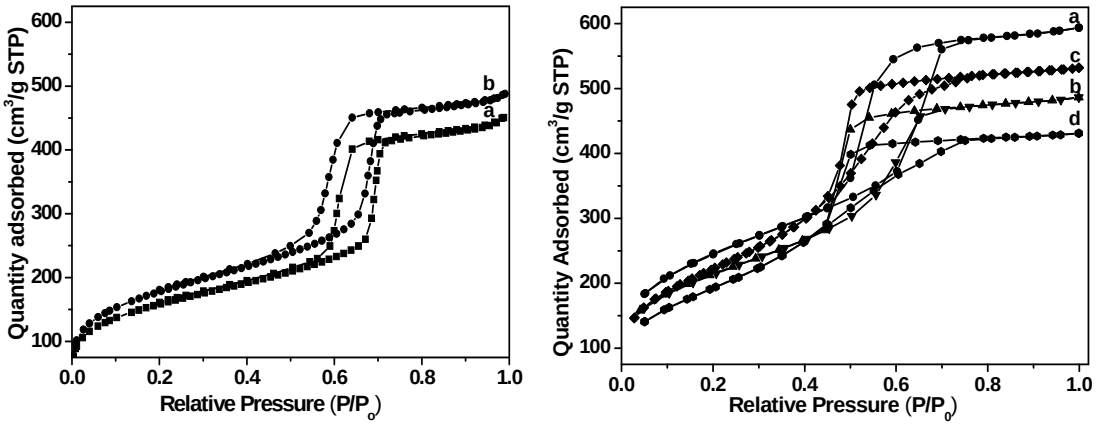

Fig. 2.4. N_2 adsorption isotherms of SBA-15 materials with different concentrations of CTAB in 1 wt% P123; left: a) without CTAB, b) with 1 mM CTAB; right: a) 4 mM CTAB, b) 8 mM CTAB, c) 16 mM CTAB and d) 32 mM CTAB.

Table 2.1. N_2 adsorption measurements of SBA-15 materials synthesized with different concentrations of CTAB in 1 wt% P123.

CTAB Concentration (mM)	Pore Size (Å)	BET (m^2/g)	N_2 Uptake (cm^3/g, STP)	Total Pore Volume (cm^3/g)	Micropore Volume (cm^3/g)
-	87	550	451	0.7	0.03
1mM	83	621	489	0.75	0.02
4mM	54	882	593	0.92	0.1
8 mM	47	770	486	0.75	0.05
16 mM	43	794	532	0.82	0.003
32 mM	33	698	432	0.66	0.65

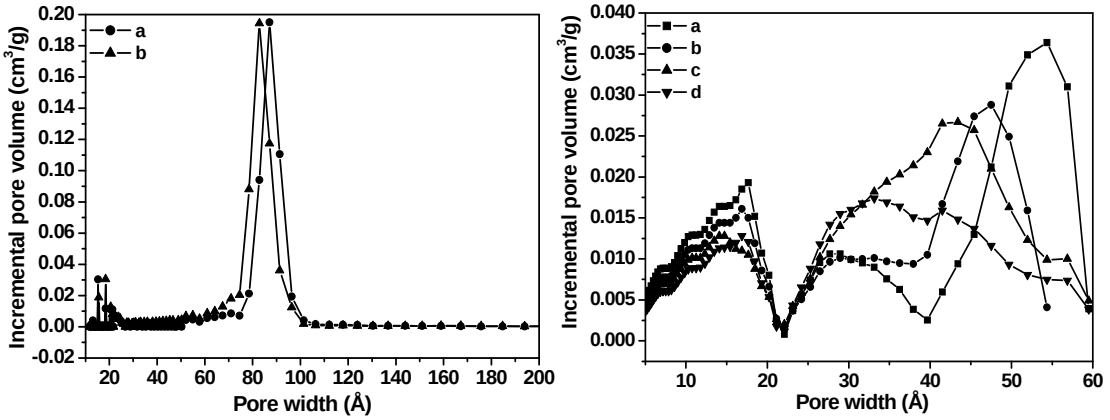

Fig. 2.5. Pore size distributions of SBA-15 materials with different conc. of CTAB in 1 wt% P123; left; a) without CTAB, b) 1 mM CTAB; right: a) 4 mM CTAB, b) 8 mM CTAB, c) 16 mM CTAB and d) 32 mM CTAB.

Thus, it becomes evident that the presence of CTAB at 1 mM concentration within the polymer micelle has no effect on the overall micellar structure. So, it is taken as optimum concentration for incorporating the metals in SBA-15.

2.4.1.3. Scanning Electron Microscopy

SEM studies were done to study the morphology of various SBA-15 materials synthesized with different concentration of CTAB in P123 (Fig. 2.6). SBA-15 synthesized without any CTAB showed small spherical particles (<1μm) attached to each other forming long bead like structures. Small particles with polygonal and spherical morphologies with size varying from 0.5 to 1.5 μm were observed in case of SBA-15 synthesized with 1 mM CTAB. SBA-15 synthesized with 4 mM CTAB showed highly agglomerated particles of various sizes mostly between 1-2 μm and elongated particles with coiled morphologies were also observed. Particles with various sizes and morphologies like spherical, polygonal, coiled and irregular shape were observed in the samples synthesized with 8 mM CTAB. Bigger lumps (4-25 μm) along with smaller spherical (0.5-3 μm) morphologies were predominant in materials synthesized with 16 mM CTAB in P123. Mostly spherical particles of size 0.5-3 μm were observed in case of 32 mM CTAB. This observation may also be correlated to a disturbance to the micellar structure with increasing CTAB concentration as well as the presence of disordered material.

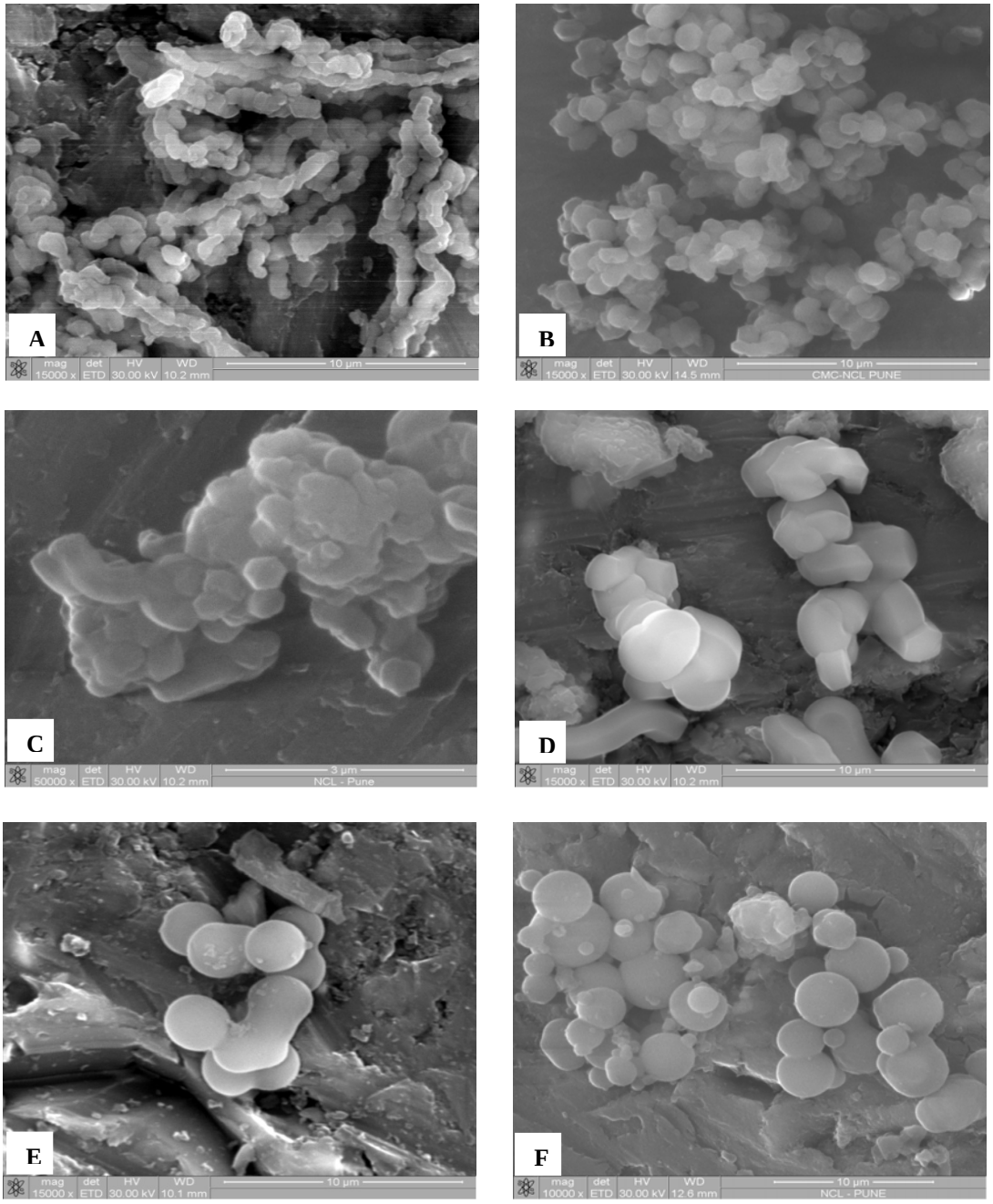

Fig. 2.6. SEM Images of various SBA-15 materials synthesized with different concentration of CTAB in 1 wt% P123; A) w/o CTAB, B) with 1 mM CTAB, C) 4 mM CTAB, D) 8 mM CTAB, E) 16 mM CTAB and F) 32 mM CTAB.

2.4.2. Characterization of Pt/SBA-15

An optimum concentration of 1 mM CTAB in the final mixed micelle composite was taken to incorporate platinum since higher concentration results in decrease in order of the final mesoporous material. When platinum precursor is added to mixed micelle, it results in the formation of ion pair ($[CTA]_2[PtCl_6]$) also indicated by the appearance of sudden turbidity in the system (discussed in detail in chapter 3A

section 3A.5). Since there is an electrostatic interaction of CTAB with $[PtCl_6]^{2-}$, the molar ratio of CTAB and H_2PtCl_6 was kept 2:1. Hence concentration of platinum was fixed at 0.5 mM which amounts to a Pt loading of 1-2 wt% in the final mesoporous compound. Pt/SBA-15 was characterized by XRD, N_2 adsorption, SEM and HRTEM and compared with SBA-15.

2.4.2.1. Powder X-Ray Diffraction

The XRD studies showed that the mesoporous nature of SBA-15 was intact after Pt incorporation (Fig.2.7). Moreover, as clear from the presence of higher order peaks, long range order was maintained in the Pt incorporated sample. Unit cell values for calcined samples were calculated based on hexagonal lattice parameters $a=\sqrt{(4/3)}d_{100}$ where d_{100} was calculated from Bragg's equation. A discernible expansion of the mesoporous unit cell parameters occurred by the inclusion of Pt when compared to the mesoporous material prepared without platinum dispersion (Table 2.2). Scanning at higher angles revealed the presence of Pt nanoparticles of ~ 8 nm calculated by Scherrer equation. A small swelling of the material with Pt before calcination was observed pointing to a possible effect by the mere dispersion of Pt precursor within the template on the unit cell.

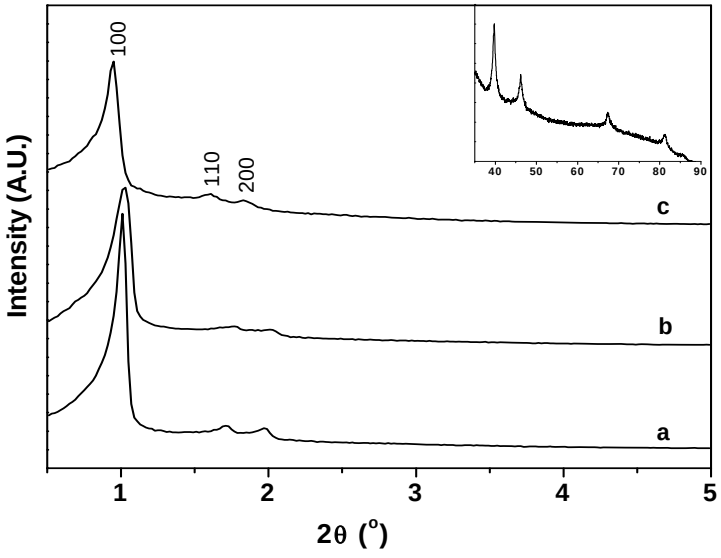

Fig. 2.7. XRD patterns of calcined samples of a) pure SBA-15 using 1 wt% P123 as template, b) SBA-15 with 1 mM CTAB incorporated into 1 wt% P123 and c) Pt incorporated SBA-15 prepared with 1 wt% polymer template P123 and 1 mM CTAB. Inset: Wide angle XRD showing the presence of Pt nanoparticles.

2.4.2.2. N_2 Adsorption

N_2 adsorption studies showed that the Pt incorporation had led to an unusual increase in surface area and overall adsorption capability when compared to pure and CTAB modified SBA-15 (Table 2.2). The shape of the isotherm of Pt/SBA-15 remains unchanged indicating the absence of any blockage of the channels by the Pt nanoparticles (Fig. 2.8).

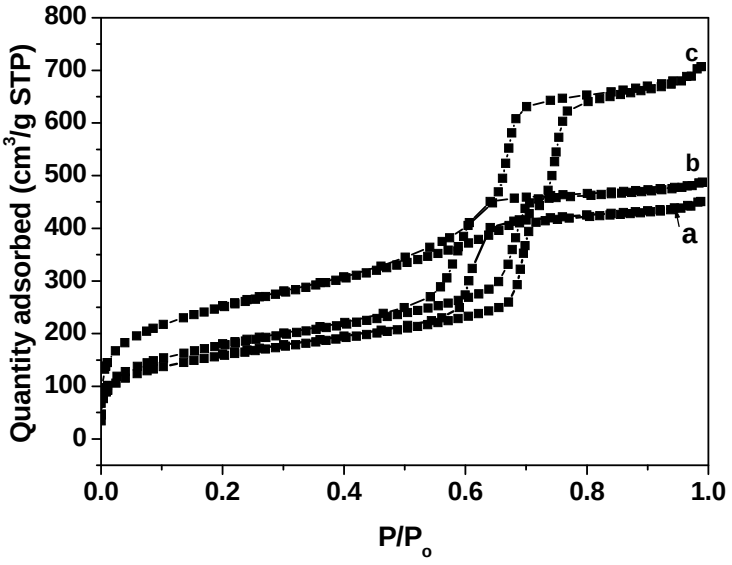

Fig. 2.8. N_2 adsorption isotherms of a) pure, b) CTAB added and c) Pt/CTAB incorporated SBA-15.

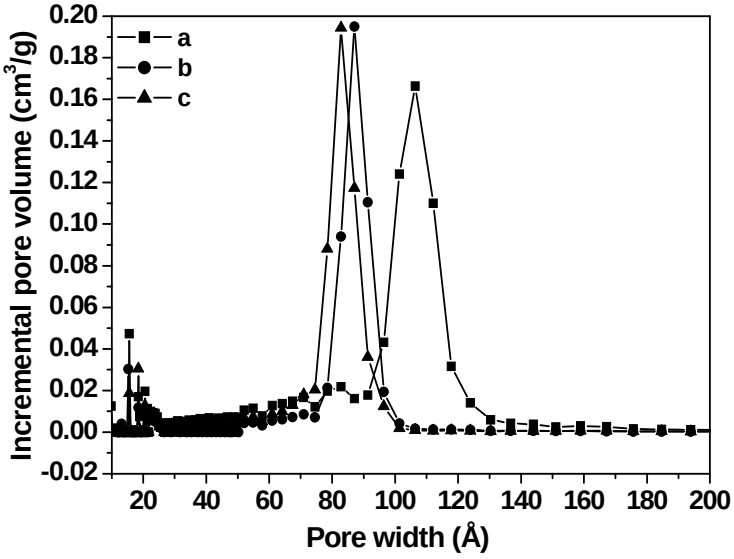

Fig. 2.9. Pore size distribution of a) Pt/CTAB incorporated SBA-15, b) CTAB added and c) pure.

Table 2.2. Unit cell and adsorption measurements of calcined pure SBA-15, SBA-15 (with CTAB) and Pt/SBA-15 (with CTAB).

Material	Unit Cell (Å)	Pore Size (Å)	BET (m^2/g)	N_2 Uptake (cm^3/g STP)	Total Pore Volume (cm^3/g)	Micropore Volume (cm^3/g)
Pure SBA-15	99	87	550	451	0.7	0.03
SBA-15 (with CTAB)	98	83	621	489	0.75	0.02
Pt/SBA-15(with CTAB)	108	106	870	707	1.09	0.04

The surface area, pore volume, adsorbate uptake and pore diameter were enhanced as compared to pure SBA-15. This was consistent with the unit cell expansion as seen by XRD studies and further suggested that the Pt particles reside within the channels. However these variations may also be inherent properties of different samples. A comparison of the pore size calculated from adsorption studies and the unit cell dimensions calculated from XRD gave the wall thickness of Pt/SBA-15 as 2 Å.

2.4.2.3. UV-Visible Spectroscopy

Metal particles show broad range of absorption in ultraviolet region, due to excitation of surface plasmon resonances or interband transitions [20, 21]. UV-Visible spectra of as-synthesized Pt/SBA-15 shows three distinct absorption maxima, one at 273 nm which is due to ligand to metal charge transfer (CT) absorption of $[PtCl_4][CTAB]_2$ complex, others at 375 nm and 475 nm which correspond to d-d transitions [22] (Fig. 2.10). In calcined samples these absorption maxima completely disappear. A broad absorption band at 266 nm appears which can be attributed to the platinum nanoparticles in the calcined samples [23, 24]. Absence of surface plasmon resonance bands in the as-synthesized sample indicates that the formation of Pt nanoparticles occurs mostly during calcination.

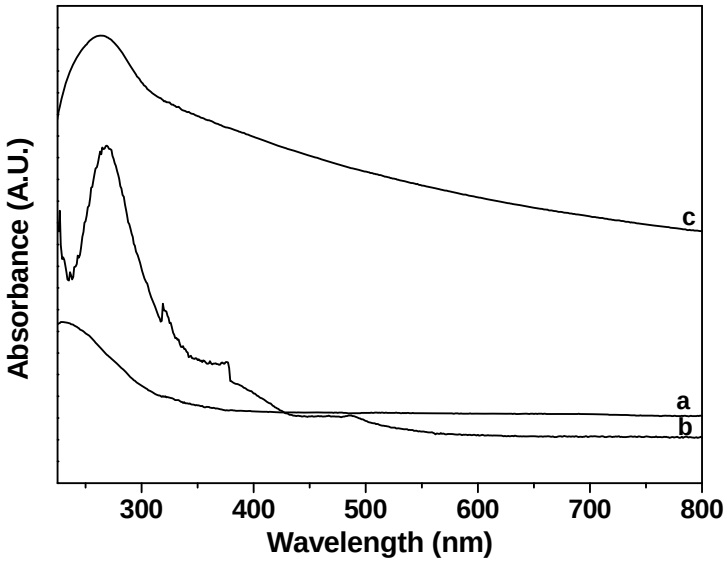

Fig. 2.10. UV-Visible spectra; a) SBA-15, b) as-synthesized Pt/SBA-15 and c) calcined Pt/SBA-15.

2.4.2.4. High Resolution Transmission Electron Microscopy

TEM images of the uncalcined sample showed only traces of Pt particles (Fig. 2.11).

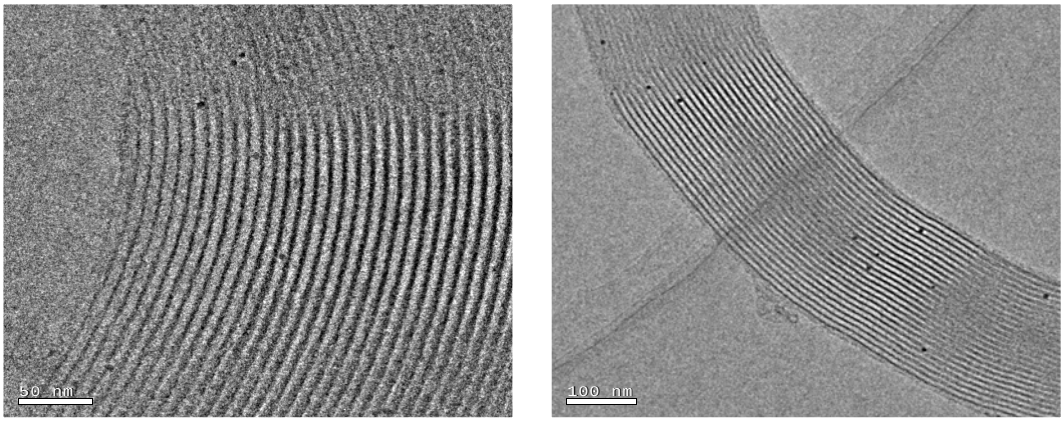

Fig. 2.11. TEM images of Pt incorporated as-synthesized Pt/SBA-15.

Calcined Pt/SBA-15 samples show a very uniform dispersion of Pt particles within the SBA-15 channels. A general scan of the sample did not show any Pt particles on the surface of the silica matrix, as expected (Fig. 2.12a). A closer look at the mesochannels (Fig. 2.12b, c) evidenced the presence of nanoparticles of size varying from 6 to 9 nm, located well within the mesopore (Fig. 2.13). Average size was found to be 8 nm. It also becomes clear from TEM that some of the nanoparticles may lead to localized swelling of the mesopore wall structure probably because the local concentration of the precursor exceeded the optimum for a restricted growth

within the channel (Fig. 2.12d). The particles are localized within the pores, grown within and molded by the channel walls. White circles mark localized swelling of the silica wall.

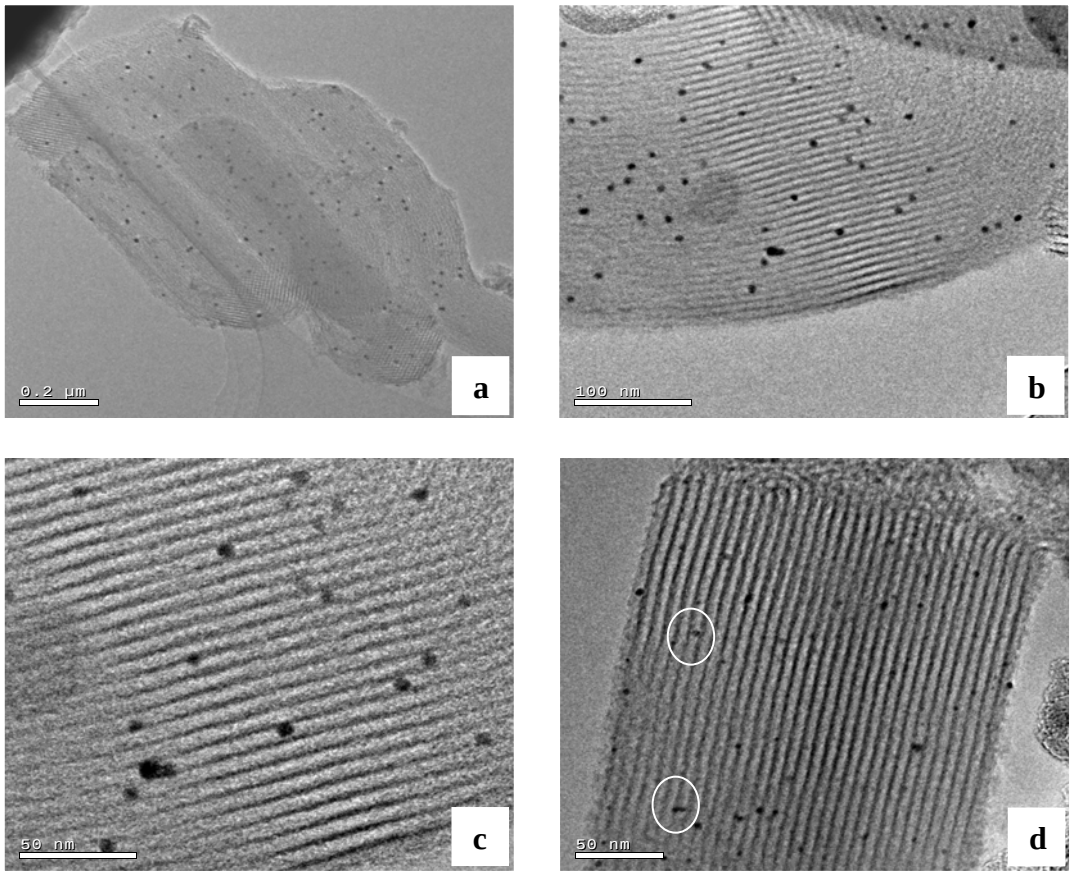

Fig. 2.12. TEM images of Pt incorporated calcined SBA-15.

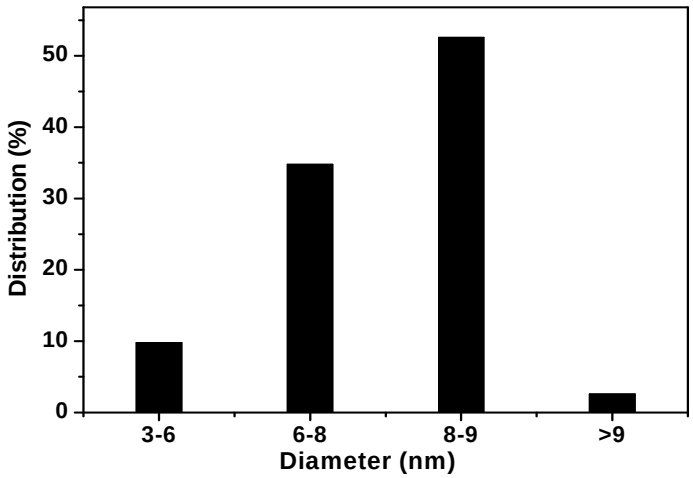

Fig. 2.13. Particle size distribution in Pt/SBA-15.

It is noteworthy that most of the particles have grown within the channels and no sign of agglomeration is seen. This shows that the Pt precursor could diffuse well into the micelle structure aided by the attractive force towards the ionic surfactant

within the core, preventing the formation of clusters of Pt precursor which would later lead to metal particle agglomeration. To confirm the role of CTAB in enhancing precursor dispersion, SBA-15 was prepared by using $[PtCl_6]^{2-}$/P123 composite as template without CTAB addition and the final calcined material observed under TEM (Fig. 2.14). In this case, agglomeration of Pt over the surface of the mesoporous material was seen. The retention of Pt also was highly improved (40%) in CTAB incorporated polymer when compared to naked micelle (7%).

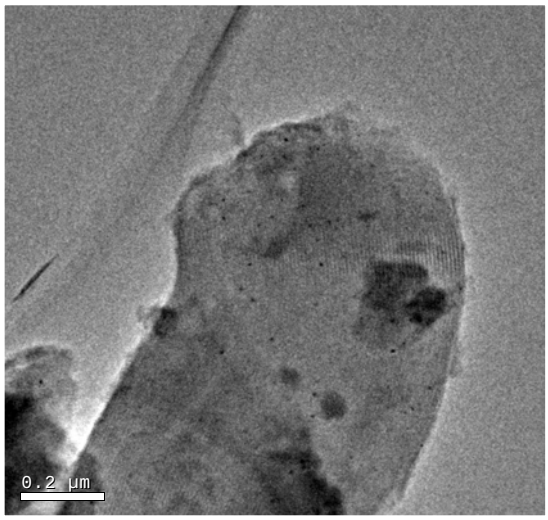

Fig. 2.14. TEM of calcined Pt/SBA-15 synthesized without CTAB in P123.

2.4.2.5. Scanning Electron Microscopy

Incorporation of Pt does not lead to any change in size and morphologies of particles. In this case also spherical and polygonal particles with 0.5-1.5 µm sizes were observed similar to SBA-15 synthesized with 1 mM CTAB in P123.

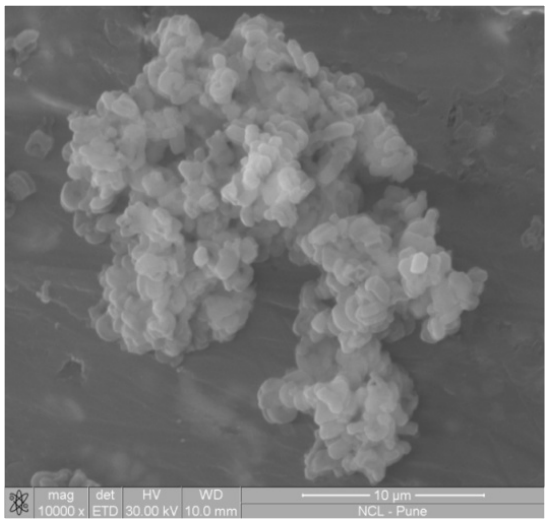

Fig. 2.15. SEM image of Pt/SBA-15

2.5. MECHANISTIC ASPECT OF FORMATION OF PLATINUM NANOPARTICLES IN MESOPOROUS CHANNELS

To understand the mechanism of formation of Pt nanoparticles, especially the stage at which they are encapsulated within mesochannels, *in situ* X-ray diffraction and UV-Visible studies were carried out during the calcination of as-synthesized Pt/SBA-15. Calcination was carried out under N_2 flow up to 400°C and after that in air up to 800°C with 1°C/min ramp rate.

2.5.1. *In Situ* High Temperature X-Ray Diffraction

In situ high temperature X-ray studies were done in XRK-900 (Fig. 2.1). As-synthesised Pt/SBA-15 was calcined and XRD was taken at various temperatures during the calcination (Fig. 2.16). No peaks corresponding to diffraction from platinum lattice planes were observed in as-synthesized samples indicating that Pt does not exist as metal nanoparticles detectable by XRD. As temperature increases platinum peaks evolve and increase in intensity showing the increase in particle size and crystallinity. These results show that platinum nanoparticle formation occurs primarily during calcination.

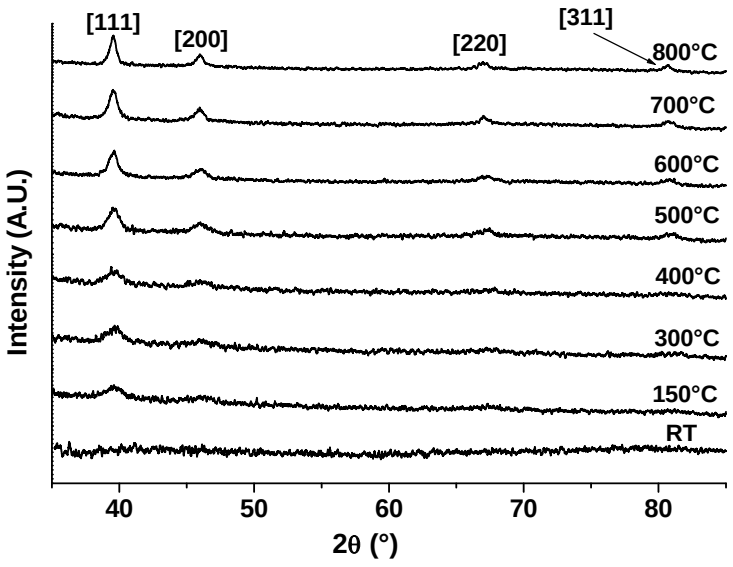

Fig. 2.16. Variable temperature XRD patterns of Pt/SBA-15 from 25 to 800°C.

2.5.2. *In Situ* UV-Visible Studies

As-synthesized Pt/SBA-15 was calcined in the high temperature Harrick Praying Mantis accessory under gas flow as described in section 2.3 and UV spectra were recorded at various temperatures. All the three absorption bands (i.e. one ligand to metal charge transfer and two d-d transitions) shown by as-synthesized Pt/SBA-15 disappear with increase in temperature indicating that metal salts slowly get reduced to platinum particles (Fig. 2.17 left). Here, plasmon resonance band due to Pt particles cannot be seen in the final calcined SBA-15 which may be due to the decreased energy of UV radiation caused by the increased path length before falling on the material kept in the *in situ* chamber. Similarly, variable temperature treatment was also given to the Pt/SiO_2 (SiO_2 impregnated with $H_2PtCl_6.6H_2O$) and *in situ* UV-Visible studies show the same pattern (Fig. 2.17 right).

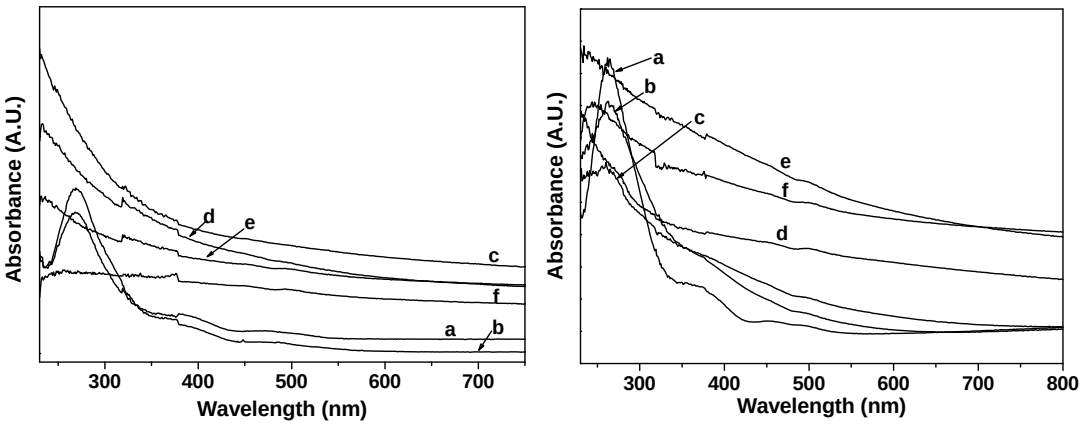

Fig. 2.17. UV-Visible spectra of as-synthesized Pt/SBA-15 (left) and Pt/SiO_2 (right) during calcinations at various temperatures; a) Room Temperature, b) 100°C, c) 200°C, d) 300°C, e) 400°C and f) 500°C.

2.6. CHARACTERIZATION OF Au/SBA-15 AND Pt-Au /SBA-15

Au/SBA-15 and Pt-Au/SBA-15 were characterized using XRD, UV-Visible studies and HRTEM.

2.6.1. Powder X-Ray Diffraction

Wide angle XRD pattern of Au/SBA-15 shows the presence of Au particles in both as-synthesized as well as calcined SBA-15 (Fig. 2.18). This behavior is typical to gold as we did not observe this in case of platinum. This shows that Au salt gets reduced during the synthesis itself. This also indicates that the interaction of Pt and

Au salts with CTAB and subsequent ion pair formation is inherently different. It is also possible that the ion pair aggregates seen in case of Pt stabilize it against reduction and agglomeration in the initial stages. Calcined, Au/SBA-15 show much intense and sharper peaks than as-synthesized one which indicates that there is sintering of Au particles to some extent during calcination process.

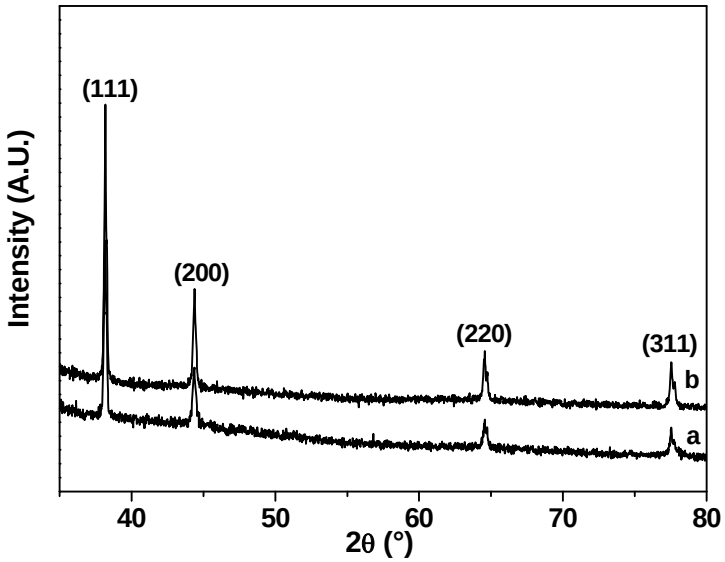

Fig. 2.18. XRD pattern; a) as-synthesized and b) calcined Au/SBA-15.

Wide angle XRD pattern of calcined Pt-Au/SBA-15 shows the presence of both Au and Pt nanoparticles separately ruling out any alloy formation (Fig. 2.19). This also confirms that mechanism of formation of Au and Pt nanoparticle formation is quite different.

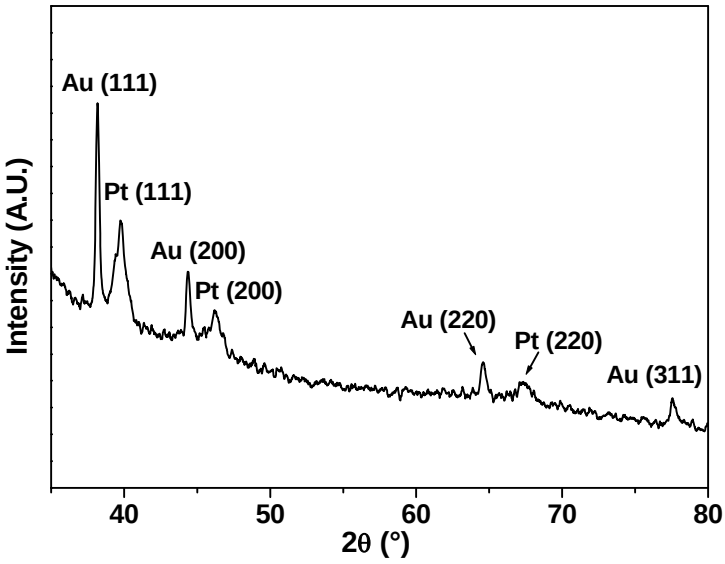

Fig. 2.19. XRD pattern of calcined Pt-Au/SBA-15.

2.6.2. UV-Visible Studies

UV-Visible studies of Au/SBA-15 shows broad absorption band which is due to plasmon resonance of Au nanoparticles around 450 nm in as-synthesized samples and it gets shifted to 500 nm in calcined samples (Fig. 2.20 left). This may be due to the sintering process and increase in size.

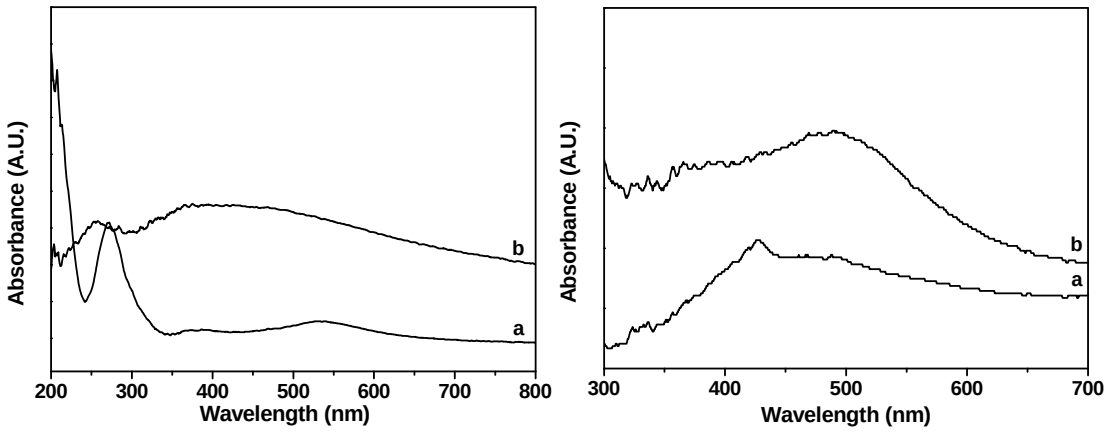

Fig. 2.20. UV-Visible spectra of Pt-Au/SBA-15 (left) and Au/SBA-15 (right); a) as-synthesized, b) calcined.

As-synthesized, Pt-Au/SBA-15 shows the ligand to metal charge transfer peaks due to platinum precursor and broad maximum around 550 nm due to plasmon resonance of gold nanoparticles (Fig. 2.20 right). While calcined sample shows broad absorption band from 350 to 500 nm and one more at 266 nm due to plasmon resonance of gold and platinum nanoparticles respectively.

2.6.3. High Resolution Transmission Electron Microscopy

HRTEM images of calcined Pt-Au/SBA-15 shows the presence of metal nanoparticles both inside and outside the channels (Fig. 2.21). It is very difficult to differentiate between Au and Pt nanoparticles since the particles are embedded in silica and does not give clear picture of lattice fringes even at high magnifications which otherwise can be used to distinguish the particles by calculating the d-spacing. But bigger particles which are present outside the channels must be of Au as indicated by wide angle X-ray diffraction also.

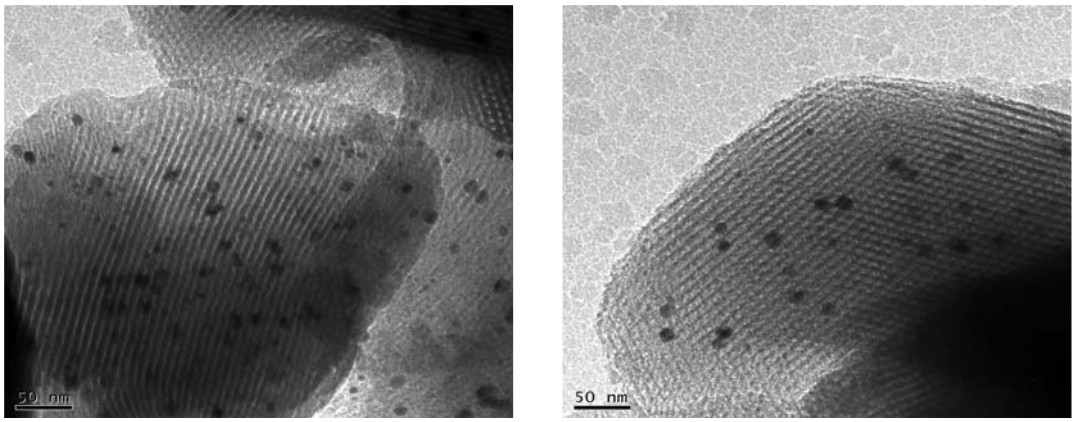

Fig. 2.21. HRTEM images of Pt-Au/SBA-15.

2.7. SUMMARY

In present chapter a novel *in situ* method has been described to synthesize metal nanoparticles in the mesoporous channels of SBA-15. Cationic surfactant CTAB is added to the aqueous solution of triblock copolymer P123 to disperse the negatively charged metal precursors (e.g. $H_2PtCl_6.6H_2O$) in polymer corona since this surfactant forms mixed micelle with polymer. Negatively charged metal salt precursor ($[PtCl_6]^{2-}$) gets dispersed in the mixed micelle composite of CTAB and P123 because of electrostatic interaction with the positive head of CTAB. When silica precursor is added to acidic solution of metal precursor mixed micelle composite, it condenses around the composite and forms silica wall after the hydrothermal treatment. This on calcination gives fairly monodispersed metal particles mostly in the mesoporous channels of SBA-15. To optimise the conc. of CTAB to incorporate Pt, SBA-15 has been synthesized with various concentrations of CTAB in P123. All the materials have been characterized by XRD, N_2 adsorption and SEM. Addition of higher concentration of CTAB (> 4 mM) results in the loss of mesoporous order, hence 1 mM CTAB is selected to incorporate platinum. Pt/SBA-15 has been characterized by XRD, N_2 adsorption, UV-Visible spectroscopy, SEM and TEM. The Pt incorporated mesoporous material has highly enhanced surface area and adsorption capabilities in comparison to parent materials without any pore blockage. *In situ* XRD and UV-Visible studies show that Pt particles are formed during the calcination. In a similar way, we have tried to synthesize Au and Pt-Au nanoparticles inside the channels. But characterization by XRD and TEM shows that method does not work for Au in SBA-15.

2.8. REFERENCES

1. D. Y. Zhao, Q. Huo, J. Feng, B. F. Chmelka, G.D. Stucky, *J. Am. Chem. Soc.* **1998**, *120*, 6020.

2. D. Y. Zhao, J. Feng, Q. Huo, N. Melosh, H. G. Fredrickson, B. F. Chmelka, G. D. Stucky, *Science* **1998**, *279*, 548.

3. C. T. Kresge, M. E. Leonowicz, W. J. Roth, J. C. Vartuli, J. S. Beck, *Nature* **1992**, *359,* 710.

4. K. Moller, T. Bein, *Chem. Mater.* **1998**, *10*, 2950.

5. H. Li, J. Chen, Y. Wan, W. Chai, F. Zhang, Y. Lu, *Green Chem.* **2007**, *9*, 273.

6. L. M. Bronstein, *Top. Curr. Chem.* **2003**, *226,* 55, and references therein.

7. R. S. Mulukutla, K. Asakura, T. Kogure, S. Namba, Y. Iwasawa, *Phys. Chem. Chem. Phys.* **1999**, *1*, 2027.

8. M. H. Haung, A. Choudrey, P. Yang, *Chem. Commun.* **2000**, 1063.

9. Z. Zhang, S. Dai, X. Fan, D. A. Blom, S. J. Pennycook, Y. Wei, *J. Phys. Chem. B* **2001**, *105*, 6755.

10 Z. Kónya, V. F. Puntes, I. Kiricsi, J. Zhu, J. W. Ager III, M. K. Ko, H. Frei, P. Alivisatos, G. A. Somorjai, *Chem. Mater.* **2003**, *15*, 1242.

11. P. Mukherjee, M. Sastry, R. Kumar, *PhysChemComm.* **2004**, 4.

12. R. P. Hodgkins, A. Ahniyaz, K. Parekh, L. M. Belova, L. Bergström, *Langmuir* **2007**, *23*, 8838.

13. H. Song, M. R. Rioux, D. J. Hoefelmeyer, R. Komor, K. Niesz, M. Grass, P. Yang, G. A. Somorjai, *J. Am. Chem. Soc.* **2006**, *128*, 3027.

14. A. K. Prashar, R. P. Hodgkins, R. Kumar, R. N. Devi, *J. Mater. Chem.* **2008**, *18*, 1765.

15. L. M. Bronstein, D. M. Chernyshov, G. T. Timofeeva, L. V. Dubrovina, P. M. Valetsky, E. S. Obolonkova, A. R. Khokhlov, *Langmuir* **2000**, *16*, 3626.

16. J. Jansson, K. Schillen, G. Olofsson, R. Cardoso da Silva, W. Loh, *J. Phys. Chem. B* **2004**, *108*, 82.

17. M. Antonietti, S. Heinz, M. Schmidt, C. Rosenauer, *Macromolecules* **1994**, *27*, 3276.

18. E. Hecht, H. Hoffmann, *Langmuir* **1994**, *10*, 86.

19. S. Dai, K. C. Tam, L. Li, *Macromolecules* **2001**, *34*, 7049.

20. G. C. Papavassiliou, *Prog. Solid State Chem.* **1980**, *12*, 185.

21. C. Burda, T. Green, C. Landes, S. Link, R. Little, J. Petroski, M. A. El-Sayed, in: *Characterization of Nanophase Materials*, Ed: Z. L. Wang, Wiley-VCH, Weinheim, 2000, *Chapter 7.*

22. T. Mang, B. Breitscheidel, P. Polanek, H. Kniizinger, *Appl. Catal., A* **1993**, *106,* 239.

23. S. Chytil, W. R. Glomm, E. Vollebekk, H. Bergem, J. Walmsley, J. Sjöblom, E. A. Blekkan, *Microporous and Mesoporous Mater.* **2005**, *86,* 198.

24. J. A. Creighton, D. G. Eadont, *J. Chem. Soc., Faraday Trans*. **1991**, *87(24),* 3881.

CHAPTER 3

FINE TUNING OF SIZE AND MORPHOLOGY OF PLATINUM NANOPARTICLES IN MESOPOROUS CHANNELS

PART A

FINE TUNING OF MORPHOLOGY OF PLATINUM NANOPARTICLES

3A.1. INTRODUCTION

Giant leaps have been made in the synthesis of metal nano architectures with different morphologies like nanorods, spheres, discs etc [1-10]. These nanostructured metals show unique properties and potential applications in optics, electronics, magnetism and catalysis. Various solution as well as template methods have been developed to synthesize nanoform of noble metals with specific architectures. There are various rigid templates such as porous anodic alumina membrane [11], zeolites [12], and mesoporous materials [13-21] which have been mainly used as host. Mesoporous silica has more advantages than others because along with providing chemical and mechanical stability, their pore size, geometry and alignment can be tuned with varying synthesis conditions so different metal structures can be prepared by selecting desirable mesoporous silica [16-18]. Nanostructures like nanowires and nanorods of noble metals in mesoporous silica are generally prepared by pore filling using wet or vapor infiltration of high concentrations of metal precursor into channels, which on further reduction by various means give these structures [19-21]. But all these methods require very high loading of metals to form these structures and also do not ensure the presence of nanoparticles exclusively inside the mesoporous channels.

In this context we further explored our *in situ* method [22] for platinum metal and found that by modifying the synthesis conditions, morphologies of platinum nanoparticles can be tuned in the final SBA-15 material. Platinum nanoparticles of different morphologies viz. spheres, rugby balls and nanorods have been obtained by merely changing the contact time of metal precursor with the mixed micelle before the addition of silica source. It seems to be an oscillatory phenomenon because small spherical nanoparticles are formed with less contact time (15 minutes) but when contact time is increased further (4 h) rugby balls are predominant morphologies (13-30 nm length). After 8 h, most of particles have nanorods like morphology (30-200 nm) but a stirring duration of 24 h leads to the formation of again spherical particles in the SBA-15 channels. This fine control over the morphology of platinum nanoparticles especially the formation of nanorod type morphology with very small loading of Pt (~ 0.5 wt%) has not been reported earlier.

3A.2. SYNTHESIS

Typically, CTAB was added to 100 g of 1 wt% solution of block copolymer Pluronic P123 so that the final composition was 1 mM of CTAB and this mixture was stirred for 24 h at room temperature. 2.6 mL of 1% solution of $H_2PtCl_6.6H_2O$ was added to this polymer-surfactant composite solution and stirred for another 15 min (S1), 4 h (S2) and 8 h (S3) at 40°C. This solution was made acidic (pH < 2) by adding 6.25 mL conc. HCl (37%) and then 2.08 g TEOS was added under stirring. This solution was heated at 40°C under stirring for 24 h and autoclaved at 95°C for 48 h. The product was filtered, washed and dried at 70°C for 24 h. The as synthesized material was calcined to remove the polymer and surfactant by heating with a rate of 0.8°C/min from room temperature to 450°C under nitrogen flow. Then temperature was increased to 500°C with the same heating rate under air flow and material was kept at this temperature for 12 h.

3A.3. INSTRUMENTS FOR CHARACTERIZATION

Details of instruments used for XRD, N_2 adsorption, HRTEM, SEM, UV-Visible and ICP-OES has already been described in chapter 2 section 2.3. All the NMR measurements were carried out on a Bruker AV400 NMR spectrometer operating at 400 MHz for ^1H at 30°C using a 5 mm broadband observe gradient probe. All the samples were prepared in 99.98% D_2O and the chemical shifts were referred to TSP at 0 ppm. The self diffusion measurements were conducted in the same probe at 30°C using a standard Bruker pulse sequence incorporating longitudinal eddy current delay [23]. Data were acquired with a 50 ms diffusion delay, 2 or 1.8 ms bipolar gradient pulses, 1 ms spoil gradient pulse and 5 ms eddy current delay. The bipolar pulse gradient strength was varied incrementally from 2 to 95%. The experimentally observed diffusion coefficients were then determined by on line processing of the data using the Bruker T1/T2 analytical tool. The data were fitted to the following equation

$$I = I_0 \exp [-D (G\delta\gamma)^2 (\Delta - \delta/3)]$$

Where, I is the observed intensity, I_0 is the signal intensity or integral in the absence of gradient pulse, D the diffusion coefficient, γ is the gyro magnetic ratio of proton, G the magnetic gradient pulse amplitude, δ the length of the gradient pulse and Δ is

the diffusion delay time. IR spectra were recorded on Thermo Nicolet Nexus 870 FT-IR and Shimadzu FTIR-8300 spectrometers.

3A.4. CHARACTERIZATION

All the mesoporous materials were characterized by XRD, N_2 adsorption, HRTEM, SEM, EDAX and elemental mapping.

3A.4.1. Powder X-Ray Diffraction

Powder XRD studies show that the mesoporous nature is intact in all the compounds (Fig. 3A.1).

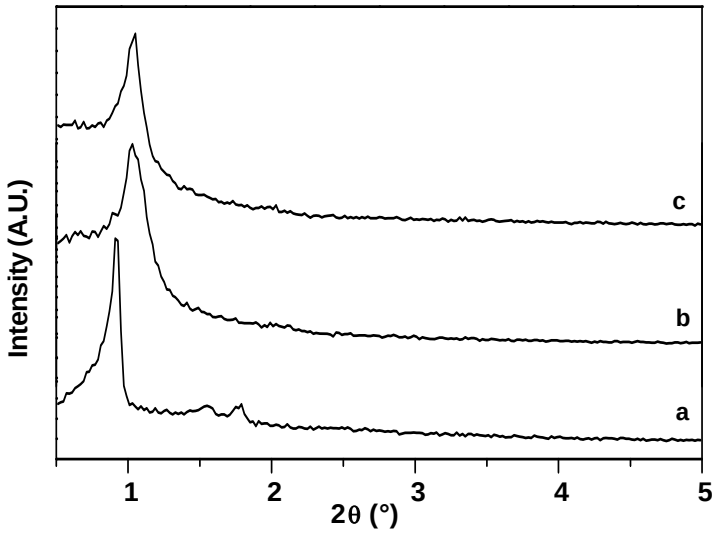

Fig. 3A.1. Low angle XRD patterns of Pt/SBA-15 samples synthesized with different contact times; a) 15 min, b) 4 h and c) 8 h.

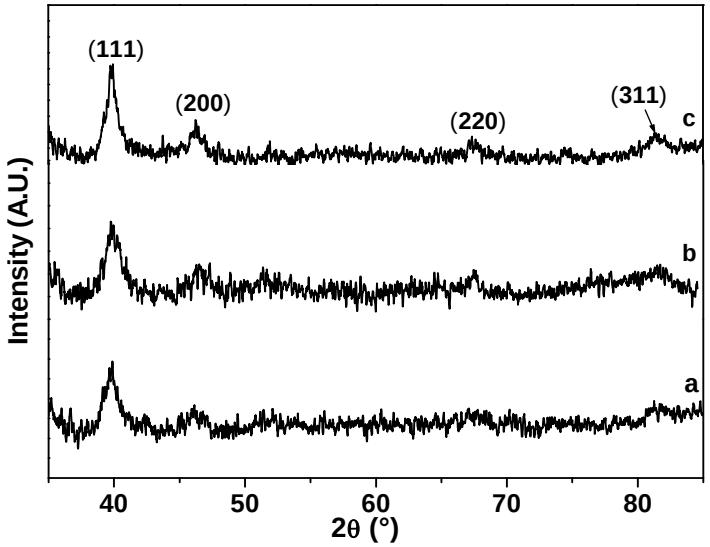

Fig. 3A.2. Wide angle XRD patterns of Pt/SBA-15 synthesized with different contact times; a) 15 min, b) 4 h and c) 8 h.

However, the long range order is less pronounced in case of S2 and S3 when compared to S1. Wide angle XRD studies indicated the presence of platinum particles and the crystallinity of platinum was enhanced with an increase in contact time as clear from the increase in intensity and the narrowing of the peaks which may be indicative of a change in size (Fig. 3A.2).

3A.4.2. High Resolution Transmission Electron Microscopy

HRTEM of S1 showed only spheroid nanoparticles with size in the range of 6-9 nm (Fig. 3A.3. left). As observed earlier, all the nanoparticles were isolated exclusively inside the mesochannels. The pore diameter of the mesoporous silica in this material was measured to be ~10 nm. However, the morphology distribution changed as the contact time was increased to 4 h. A majority of the particles were more elongated rugby ball shaped with only a small number of spheroids, the elongation of the rugby balls being along the direction of the channels (Fig. 3A.3. middle). The length of the rugby balls was in the range 13-30 nm and the average diameter was ~9 nm. The spheroid size remained more or less unaltered in comparison to the 15 min sample. As the time was increased to 8 h, morphology of the majority of particles was found to be rod like with lengths ranging from 35 nm to 200 nm (average diameter ~9 nm), however, a very small number of rugby balls (length <30 nm) were also observed (Fig. 3A.3. right). The number of spheroids remained more or less same as in the case of 4 h sample.

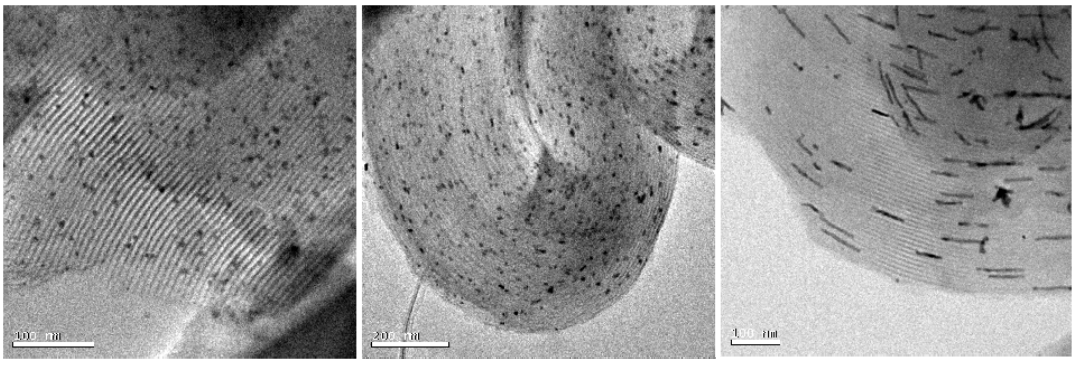

Fig. 3A.3. HRTEM images of Pt/SBA-15 synthesized with contact times of 15 min (left), 4 h (middle) and 8 h (right).

Quantitative analysis showed that the amount of Pt was more or less same in all the three samples (0.5 – 0.54 wt %). This indicates that we can control the particle

morphology based entirely on the time for which Pt ions and micelles are in contact and there seems to be an optimum duration for a particular morphology. Statistical analysis over a spread of TEM images showed a gradual change in morphology depending on the contact time (Fig. 3A.4). At 15 min, 95% of the particles were spheroids and only 5% of rugby balls were observed. When the contact time was increased to 4 h, the distribution changed to 25% spheroids, 61% rugby balls and 14% nanorods. However, after 8 h, the spheroid number remained at 29% whereas the number of rugby balls reduced to 3% and that of nanorods increased to 68%. We would like to mention here that the dispersion of nanoparticles in all the three samples was not uniform over the whole sample; silica domains with only negligible number of Pt nanoparticles were also observed.

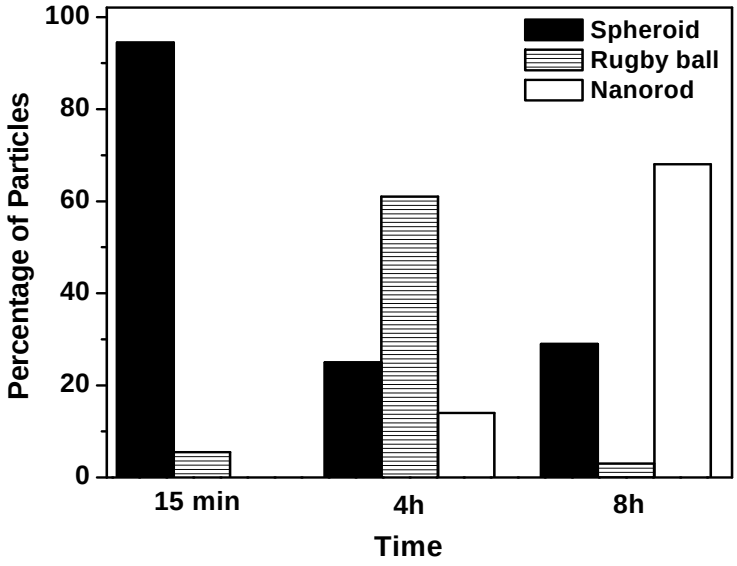

Fig. 3A.4. Particle morphology distribution of Pt/SBA-15 samples at various contact times.

3A.4.3. N_2 Adsorption Studies

N_2 adsorption isotherms also indicated a change in textural properties depending on the contact times (Fig. 3A.5). The mesoporosity of S1 is retained without any pore blockage as indicated by the sharp rise in the capillary condensation step. However, this was not the case in S2 and S3 with much flatter step which may be due to the presence of pockets not accessible to adsorbate thereby blocking the pores.

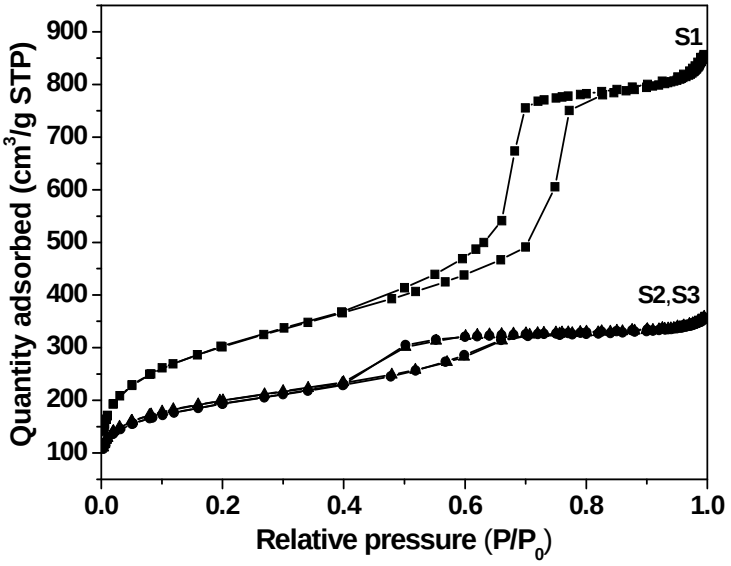

Fig. 3A.5. N_2 adsorption isotherms of samples S1, S2 and S3.

Table 3A.1. Unit cell (from XRD) and adsorption measurements of S1, S2 and S3.

Material	Unit cell (Å)	Pore size (Å)	BET (m^2g^{-1})	N_2 uptake (cm^3g^{-1} STP)	Total pore volume (cm^3g^{-1})	Micropore volume (cm^3g^{-1})
S1	110.8	101	1088	857	1.32	0.18
S2	98.5	~71	684	358	0.55	0.09
S3	97.2	~71	705	358	0.55	0.11

These observations can be attributed merely to the elongated particles inside the channels affecting the long range order of the mesoporous silica leading to lower adsorption. High surface area of S1 when compared to S2 and S3 (Table 3A.1) also reflects this observation. Even though the XRD studies show that the mesopore long range order is less pronounced in case of elongated particle incorporated samples, the phenomena mentioned below also can be major contributors in the reduction in textural properties.

The presence of nanospheres does not deter the movement of adsorbate molecules but particles elongated along the channel direction probably leads to their blockage. This is also supported by the observation from XRD that the unit cell is larger for the spheroid incorporated samples than the other morphologies. We have

already observed highly localized expansion of the silica walls around the particles [22]. Since the spheroids are more uniformly dispersed and the area of contact of the spheroid to the silica wall is less, it is feasible to have an averaged expansion of the unit cell. However, in case of elongated particles, it may be difficult to sustain an expansion in the order of tens of nanometers. Here we would like to draw attention to the pore sizes measured for S2 and S3 (~7.1 nm) when compared to the diameters of the rugby balls and rods present inside the channels (diameter measured from TEM to be ~9 nm). This is possible if the metal precursor penetrates the PEO region of the micelle responsible for micropores within the silica walls, presenting a fuzzy boundary in the nanoparticles formed after calcination – the elongated particles appearing to be bigger than the channel dimension. For a sphere with a large curvature, the area of contact of the spheroid to the silica wall is less in comparison to morphologies with elongation parallel to the pore as in the rugby ball morphology. Hence when the Pt precursors are locally concentrated giving rise to rugby ball morphology after calcination, there is more penetration of Pt within the micropores of a single SBA-15 pore channel. If there are a series of elongated Pt nanoparticles in close vicinity within the same channel and in adjacent channels, then the micropore blockage is increased and voids inaccessible to adsorbate molecules are formed leading to lower uptake.

3A.4.4. SEM and EDAX Analysis

It is known that synthesis conditions can affect the overall morphology of mesoporous silica. Under the conditions employed in this work, SBA-15 is reported to adopt a coiled tubular structure. This overall morphology was found by SEM analysis to be intact after the incorporation of Pt of various shapes (Fig. 3A.6-3A.8). Elemental analysis by ICP showed that Pt is present as 0.5 wt% in silica. However, the distribution of metal particles observed in some TEM images appears to be much more than 2 wt%. This raises the question of uniformity of the dispersion of nanoparticles. To address this issue, elemental mapping by EDAX was carried out on all the three samples. The distribution of Pt and Si was observed in the area of 200 μm^2. The platinum mapping clearly shows that the distribution is uniform within a resolution of 1-3 μm. This was the case with S2 and S3 also. Hence we can conclude that even though the distribution may be non-uniform in nm scale, but overall Pt distribution is highly uniform.

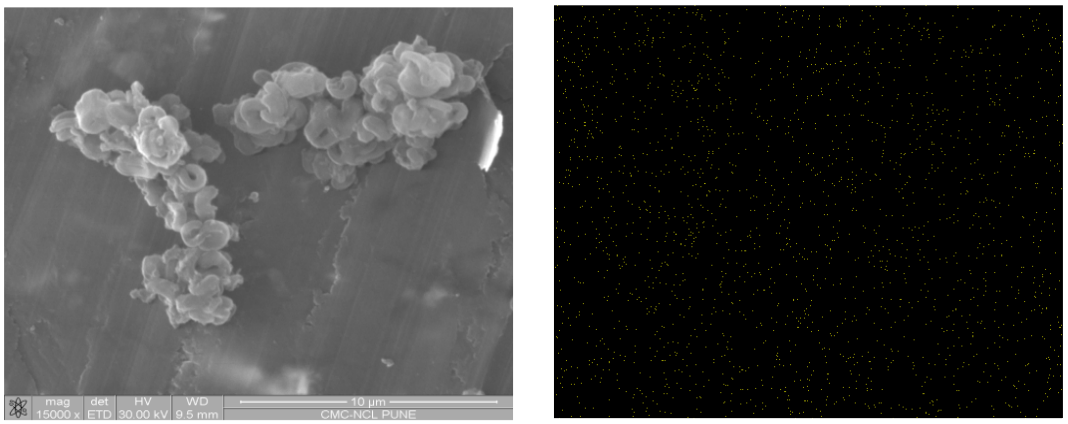

Fig. 3A.6. SEM image and Pt mapping of S1.

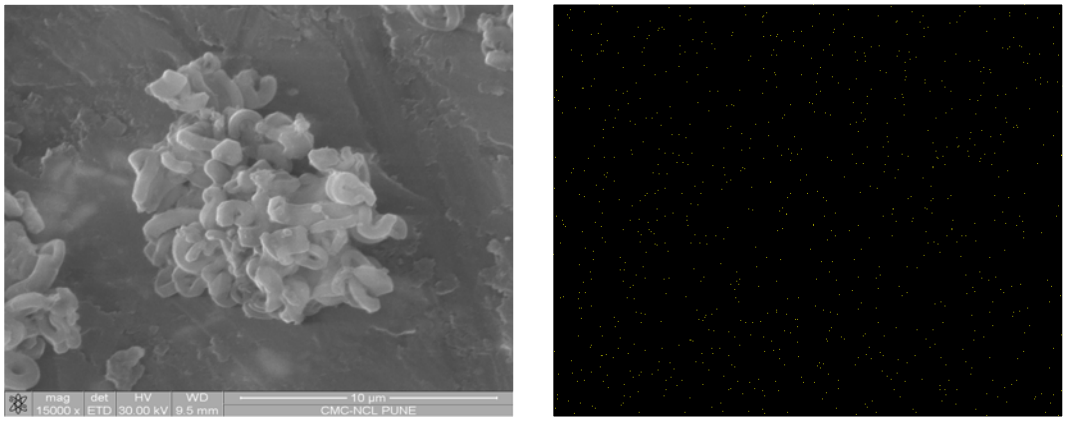

Fig. 3A.7. SEM image and Pt mapping of S2.

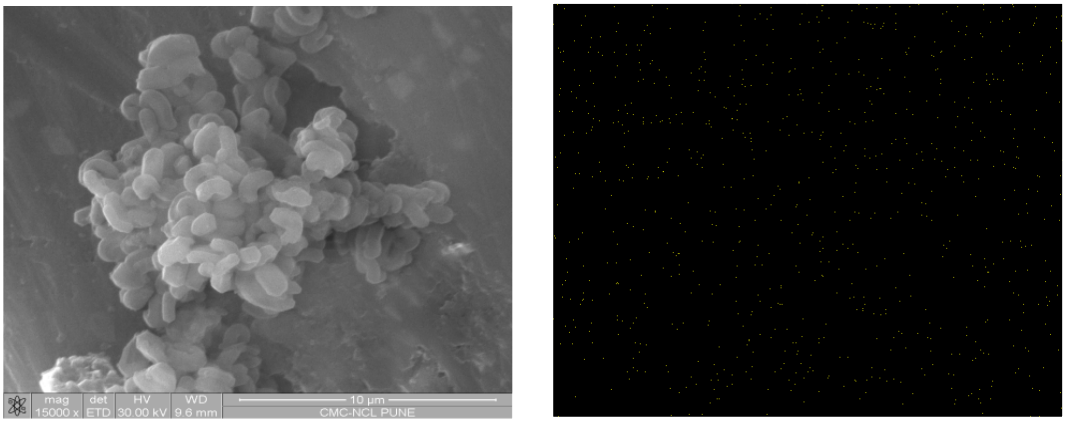

Fig. 3A.8. SEM image and Pt mapping of S3.

3A.5. PLAUSIBLE MECHANISM FOR EFFECT OF DIFFERENT CONTACT TIMES ON THE MORPHOLOGIES OF PLATINUM IN FINAL MATERIAL

The unique observation of formation of elongated nano morphologies leads to further question regarding the mechanism of their formation. Two possibilities can be suggested (i) sintering of the platinum at higher temperature leading to elongated particles, (ii) formation of elongated shapes in the precursor stage itself. To answer this, S1 with spherical Pt particles was heated to 800°C and change in shape was observed by TEM (Fig. 3A.9). Sintering effects of platinum is very severe at temperature > 600°C. So logically, if sintering plays a part, we should have observed the presence of nanorods at high temperature. Since this was not the case and it shows sintered particles retaining their spheroid structure but bigger than the diameter of mesochannels. A closer look suggests that the sintering effect even at higher temperature is very minimal. This means that sintering mechanism does not support the lateral growth of particles (along the channel direction), whereas nanorods grow along the channel direction.

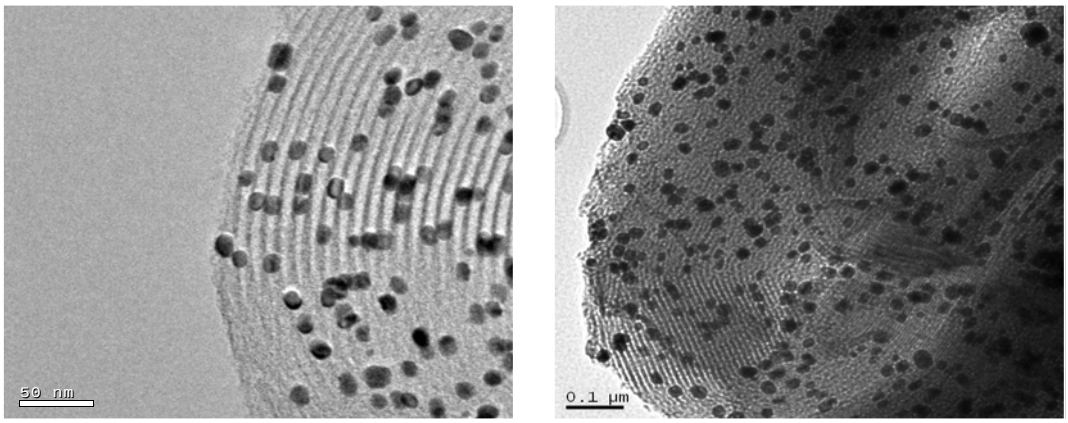

Fig. 3A.9. TEM images of S1 heated to 800^{o}C.

Moreover, TEM images of S3 sample calcined at 300°C show the presence of nanorods in the channels (Fig 3A.10). Since elongation was detected at temperature below severe sintering, we suggest that the morphology got shaped at precursor stage itself. This cannot be due to sintering process because S1 sample does not show the presence of nanorods even after heating up to 800°C.

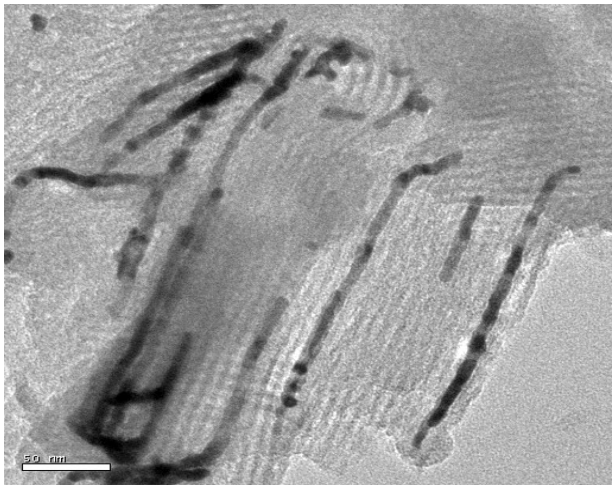

Fig. 3A.10. TEM image of S3 heated at 300^{o}C.

Hence among the two possibilities, the latter appears to be more fitting to the observation. A plausible explanation for the formation of different morphologies is as follows: the Pt ion local concentration, at 15 min, is highly dispersed conducive for the formation of spherical particles on calcination – as in the case of any conventional ion-exchange or impregnation methods. As contact time increases, the local concentration profile of Pt ions is shaped so that it facilitates the formation of progressively elongated particles. This may be due to an agglomeration of the Pt ions in the form of some precursor structure, yet to be determined, along the axis of the micelle; the polymer template somehow molding the shape and preventing agglomeration perpendicular to the micelle axis. During calcination this local concentration profile is retained and the final particle morphology reflects this. In other words, the final particle morphology is shaped in the precursor stage. Since the only parameter which was changed during synthesis was the duration for which the metal ion was kept in contact with the modified micelle, the morphology change can be attributed to a local concentration profile variation brought about by precursor diffusion or agglomeration along the micelle. At this stage, the structure of the precursor state is not evident. To follow the concentration profile of the precursor with time, the reaction was arrested at particular durations and $NaBH_4$ was employed for reduction of the precursors. These samples were observed by TEM; however, no useful information could be obtained out of it due to agglomerated particles (Fig. 3A.11).

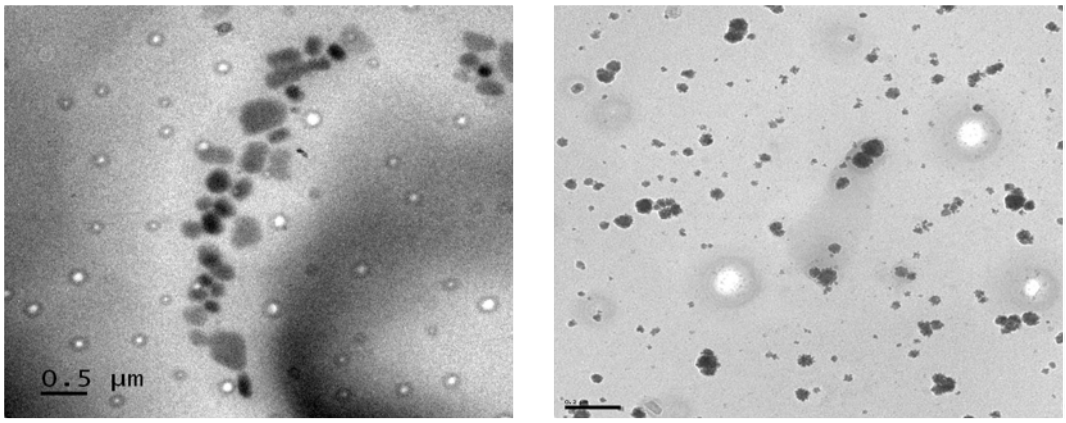

Fig. 3A.11. TEM images of agglomerated Pt particles when the synthesis was arrested at different durations and reduced with $NaBH_4$.

Due to limitations set by the nano size scale of the micelles, no concentration profile mapping techniques also could be used. However, a series of experiments were carried out by UV-Vis spectroscopy and NMR spectroscopy to investigate the state of precursor and its interaction with polymer and surfactant.

3A.5.1. UV-Visible Studies of Precursor Mixed Micelle Composite

UV-Vis spectroscopic studies were carried out by changing different parameters to see the effect of contact time as well as CTAB concentration on the chemical environment of platinum. The concentration of CTAB in 1 wt% P123 was progressively increased from 0.25 mM to 2 mM and 0.5 mM H_2PtCl_6 was added to each of these solutions before measuring UV-Vis spectra (Fig. 3A.12). These spectra were compared with that of pure $H_2PtCl_6 .6H_2O$ in 1 wt% P123 which had a peak at 259 nm attributed to ligand to metal charge transfer [24-25]. We could see a definite shift in this peak position to 285 nm as CTAB concentration increased to 1 mM.

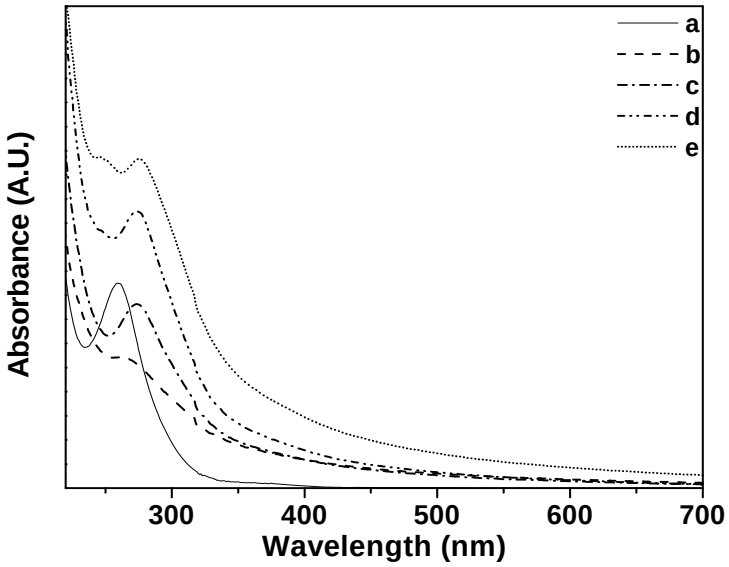

Fig. 3A.12. UV-Vis spectra of a) 0.5 mM H_2PtCl_6 and its mixture with 1 wt% P123 and b) 0.25 mM, c) 0.5 mM, d) 1 mM and e) 2 mM CTAB.

But this shift was not seen when the precursor was added to unmodified polymer and hence this may be due to a stronger interaction of $[PtCl_6]^{2-}$ with the ionic groups of CTAB. However, UV spectra of the $[PtCl_6]^{2-}$ dispersed in polymer surfactant composite micelle did not show any variation with time (Fig. 3A.13).

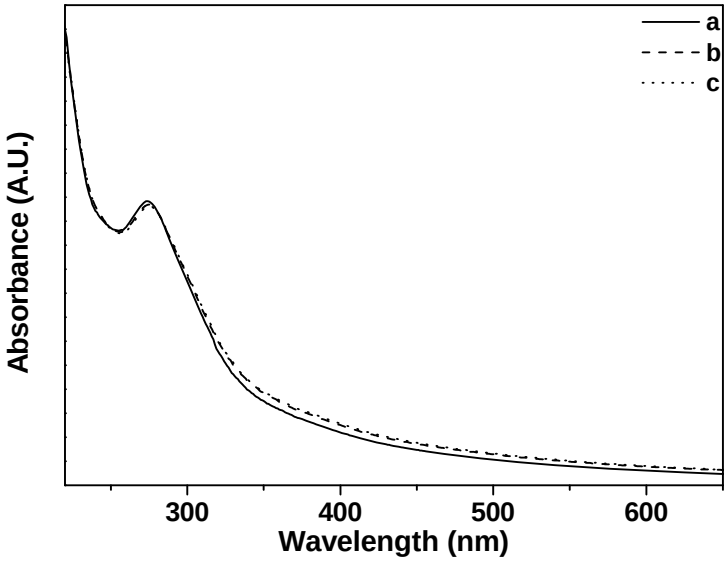

Fig. 3A.13. UV-Vis spectra of 1wt% P123, 1 mM CTAB and 0.5 mM H_2PtCl_6 composite at varying contact times; a) 15 min, b) 4 h and c) 8 h.

This indicates that there is definitely a change in the chemical environment of Pt immediately on addition to the composite micelle which remains unaltered with time. Hence it is clear that there is an instant dispersion of $[PtCl_6]^{2-}$ due to the

electrostatic interaction with CTAB. With time, the environment of $[PtCl_6]^{2-}$ does not change since it is still interacting with CTAB. This important observation gives credence to the possible mechanism for the Pt precursor concentration profile; the formation of $[PtCl_6]^{2-}$-CTAB cluster complexes inside the polymer micelle which diffuse and agglomerate with time. The large time scales in which the morphology change is observed may be due to this cluster diffusion rather than Pt ion diffusion.

3A.5.2. NMR Studies of Precursor Mixed Micelle Composite

A comparison of the ^1H NMR spectra of P123 and P123-CTAB composite micelle showed an overall broadening of the CTAB protons indicating an interaction of CTAB with P123 (Fig. 3A.14). In addition, the chemical shift of the protons of the CTAB undergoes changes which can clearly been seen in the Fig. 3A.15. The concentration of CTAB in solution studied (1 mM) is just above its CMC (0.95 mM) and hence the molecules are expected to be in the micelle from. On addition of P123, both the head and that tail methyl groups of CTAB showed low field shift due to the formation of mixed micelles (Fig. 3A.15).

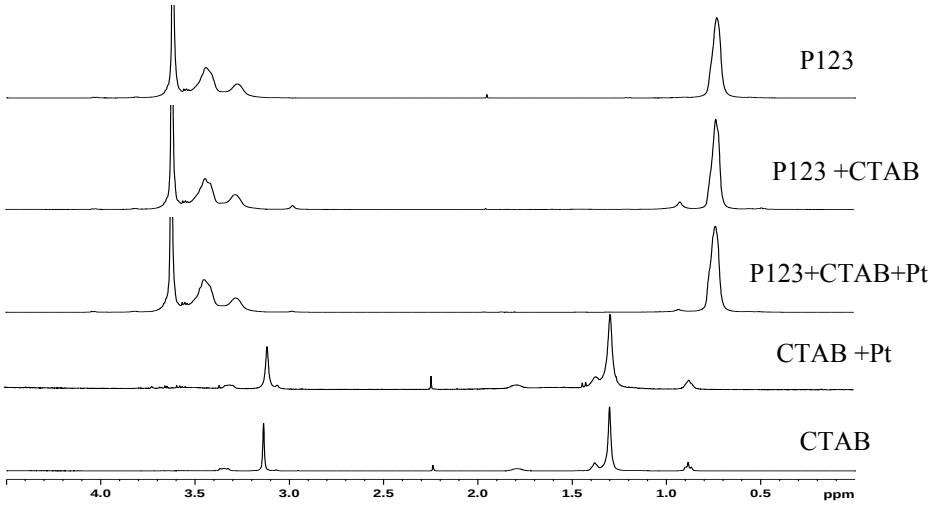

Fig. 3A.14. Comparison of 400 MHz ^1H NMR spectrum of CTAB in presence of P123 and H_2PtCl_6.

The changes occurring to the head (hydrophilic) and tail (hydrophobic) methyl groups were followed to understand the nature of the interaction of CTAB with P123 as well as $[PtCl_6]^{2-}$. Addition of H_2PtCl_6 to the 1mM CTAB solution causes an upfeild shift for both these groups which seem to suggest weakening of the hydrophobic

association of the CTAB molecules and hence the CTAB molecules present are may be below its CMC (Fig. 3A.15).

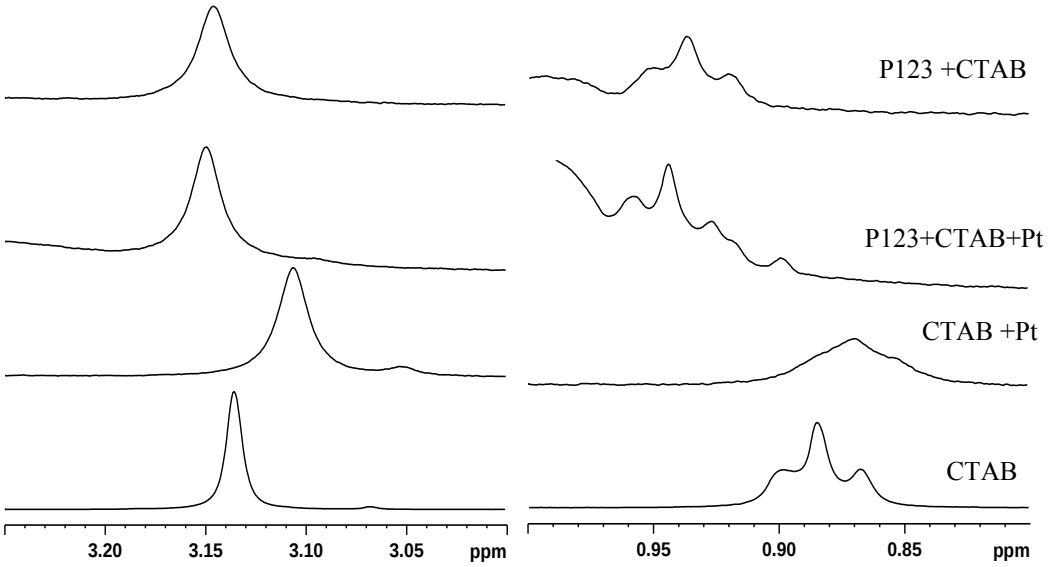

Fig. 3A.15. ^{1}H Chemical shift changes observed for the head and tail methyl protons of CTAB in presence of P123 and H_2PtCl_6.

The CTAB solution becomes turbid on addition of H_2PtCl_6. Besides, the proton signals of CTAB are also found to be weaker in presence of H_2PtCl_6 which is evident from Fig. 3A.16-18. Fig. 3A.16 depicts comparison of the ^{1}H spectrum of neat CTAB with that in presence of H_2PtCl_6. On addition of excess H_2PtCl_6 a complete disappearance of CTAB signals were noticed as the entire CTAB comes out of the solution as a yellow precipitate.

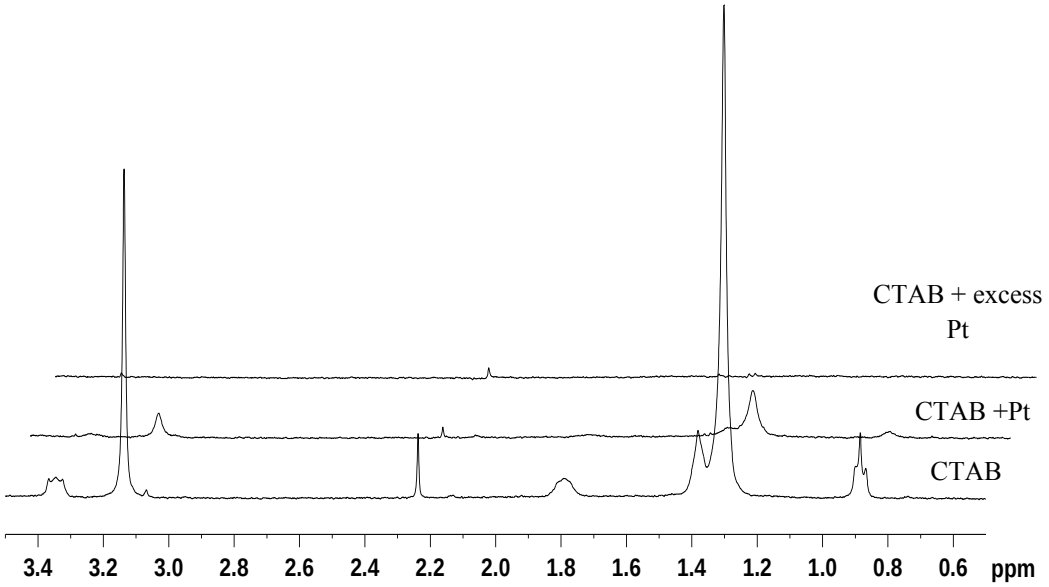

Fig. 3A.16. Effect of addition of H_2PtCl_6 to CTAB: ^{1}H spectrum of CTAB with and without H_2PtCl_6.

It is likely that the Br^- anions of CTAB are replaced by aqua-complex of $(PtCl_6)^{2-}$ and thus resulting in a CTAB complex that phase separates out from the solution are not detected by the window of ^1H NMR. This is in accordance with the turbidity observed in the NMR tube on addition of H_2PtCl_6 solution to CTAB solution. A similar observation has also been noticed on adding H_2PtCl_6 to the mixed micelle of 1wt% P123 and 1 mM CTAB. This is depicted in Fig. 3A.17. Nearly 70% of CTAB signals disappeared on addition of 0.5 mM solution of H_2PtCl_6. The solubilised portion of the total CTAB concentration still in solution behaves similar to the CTAB-P123 system, showing that it is still interacting with P123.

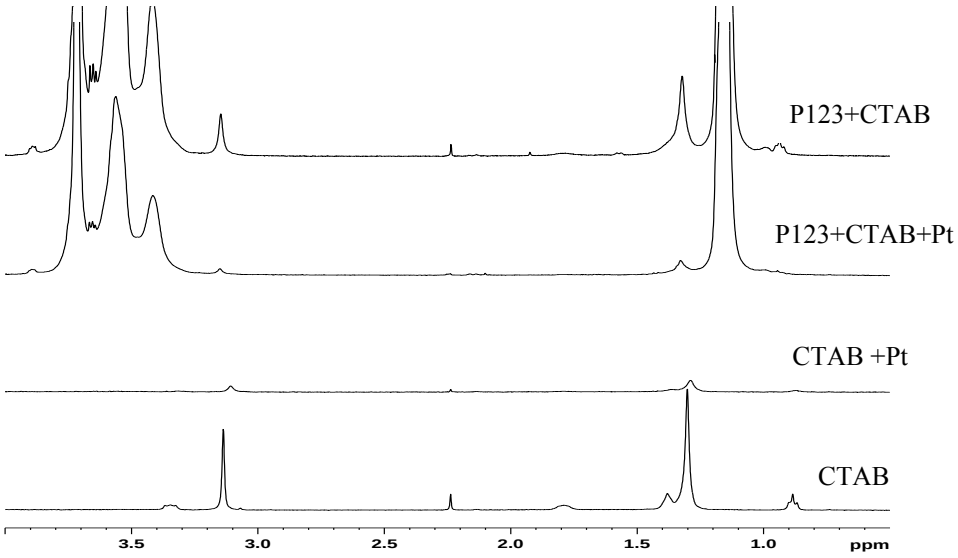

Fig. 3A.17. Effect of addition of H_2PtCl_6 to CTAB: Comparison of ^1H spectrum of CTAB with H_2PtCl_6 and P123.

This shows that most of the CTAB molecules now exists in a rigid solid like complex with Pt which give rise to broad lines and are not detected in the spectral window (~8000 Hz) used for the observation of the narrow signals of the molecules in solution. The free CTAB in solution state decreases slightly as contact time increases, indicating more and more CTAB being part of the rigid complex (Fig. 3A.18). However, addition of excess H_2PtCl_6 also resulted in an immediate and significant decrease in this CTAB concentration (Fig. 3A.16). This shows that there is excess of CTAB not interacting with $[PtCl_6]^{2-}$ in solution and this excess solubilised CTAB becomes part of the rigid CTAB-$[PtCl_6]^{2-}$ complex with time.

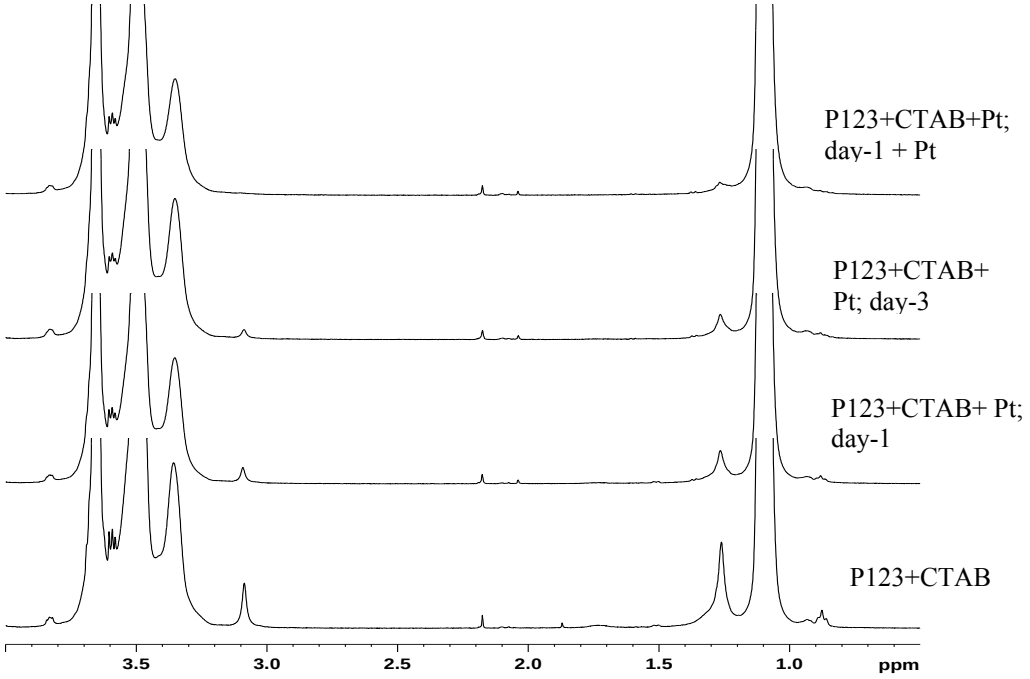

Fig. 3A.18. Effect of addition of $H_2PtCl_6.6H_2O$ to P123-CTAB mixed micelles: Comparison of ^1H spectrum of CTAB with H_2PtCl_6 and P123.

Further insight into the state of the precursor was sought by ^1H self diffusion studies using PFGNMR. The CTAB molecules showed only a single self diffusion coefficient for the 1 mM solution, in CTAB-P123 mixed micelle and also in presence of $[PtCl_6]^{2-}$ (Table 3A.2). The self diffusion coefficient decreases nearly by an order on formation of mixed micelles. On addition of H_2PtCl_6 to this mixed micelle, the diffusion coefficient of CTAB molecules remaining in the solution was very close to that of CTAB-P123 system. In general, a decrease in self diffusion coefficient can be attributed either to stronger binding or longer life times in the bound form.

Table 3A.2. NMR self diffusion coefficients of CTAB.

Sr. No.	System	NMe $x10^{-10}$ m^2/s	NCH_2 $x10^{-10}$ m^2/s	$(CH_2)_n$ $x10^{-10}$ m^2/s	ω Me $x10^{-10}$ m^2/s
1	CTAB	3.59	3.76	3.45	3.40
2	CTAB+Pt	3.05	--	3.39	--
3	P123+CTAB	0.47	-	0.43	0.48
4	P123+CTAB+Pt	0.37	-	0.33	0.32

The diffusion coefficient data for the P123 pluronics, as reported, could only be explained on the basis of a bicomponent model. The faster components are arising from the 'unimers' of the polymeric surfactant present in the 1% solution while the slower one form the aggregated polymeric surfactant (Table 3A.3 and 3A.4). The slower component of the PPO and PEO chains of P123 showed nearly the same diffusion coefficient which is slower by an order approximately. The faster components of PPO part and the PEO part showed slightly different values. Addition of H_2PtCl_6 to P123 has led to some increase in the population of the faster components of PEO units of P123.

Table 3A.3. NMR self diffusion coefficients of PEO part of P123.

Sr. No.	System	D_{fast} x10^{-10} m^2 /s	D_{slow} x10^{-10} m^2 /s	M% fast	M% slow
1	P123 (PEO)	1.55	0.19	37	63
2	P123+Pt	1.53	0.17	58	42
3	P123+CTAB	1.55	0.22	34	66
4	P123+CTAB+Pt	1.73	0.23	45	55

Table 3A.4. NMR self diffusion coefficients of PPO part of P123 (methyl group).

Sr. No.	System	D_{fast} x10^{-10} m^2 /s	D_{slow} x10^{-10} m^2 /s	M% fast	M% slow
1	P123(PPO)	1.09	0.18	21	79
2	P123+Pt	1.01	0.16	24	76
3	P123+CTAB	1.40	0.22	15	85
4	P123+CTAB+Pt	1.63	0.23	21	79

Unfortunately, further study into the nature of precursor structure could not be performed by NMR due to practical difficulties of simulating the conditions used for the nanoparticle formation for the measurements. The fact that we consistently observe the presence of nanoparticles of varying morphology exclusively within the channels of the mesoporous silica and also that the CTAB in solution may not be interacting with $[PtCl_6]^{2-}$ indicates that the rigid complex exists within the polymer micelle.

3A.5.3. IR Studies of Precursor Mixed Micelle Composite

To understand the factors affecting this phenomenon, a mixture of P123, CTAB, and H_2PtCl_6 was ultracentrifuged and the colloid and liquid phases were separated and a qualitative characterization of the phases was attempted by IR spectroscopy (Fig. 3A.19 and 3A.20). A quantification and comparison of the spectra is not attempted due to practical instrumental errors of changes in liquid and solid spectra. It was observed that the particulate phase was a composite of P123 as well as CTAB, whereas the filtrate was mostly P123 with a reduced amount of CTAB present. This is very much in agreement with NMR results indicating a rigid solid like $[CTA]_2[PtCl_6]$ complex but still interacting with P123. During silica formation, the P123-CTAB-$PtCl_6$ composite micelle as well as free P123 act as templates; the in homogeneity of the samples with respect to Pt dispersion in nanometre scale may have risen from this factor. These extensive studies have shown that the formation of nanoparticles with different morphologies occurs with different contact times, which may be due to varying extents of agglomeration of a rigid CTAB-$PtCl_6$ complex precursor. This also supports large time scales in which morphology variation is observed.

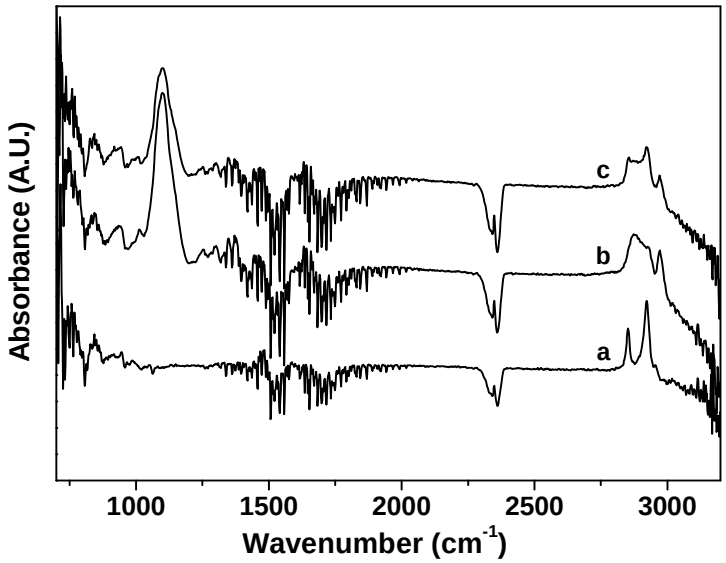

Fig. 3A.19. IR spectra; a) pure CTAB, b) P123 and c) mixture of P123 and CTAB.

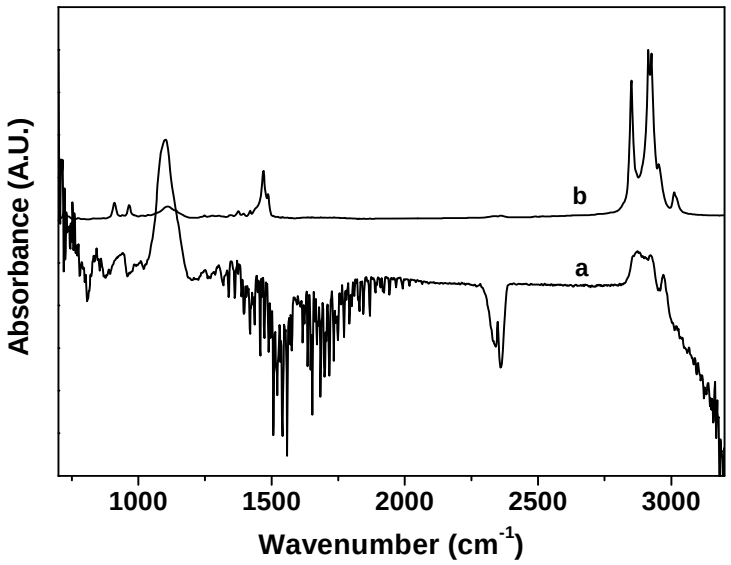

Fig. 3A.20. IR spectra; a) filtrate separated by centrifugation, b) colloid phase.

3A.6. SUMMARY

It has been found that change in stirring time of platinum precursor with polymer-CTAB mixed micelle composite results in different morphologies of platinum in the final material. TEM studies of the synthesized material showed that predominant morphology of platinum particles changes from spherical (95%) (stirring time 15 min) to rugby ball (61%) at 4 h stirring time and stirring for longer duration (8 h) results in nanorods morphology (68%). There are two possibilities either (i) sintering at higher temperature leads to elongated morphologies or (ii) formation of elongated shapes at the precursor stage itself. We did not observe the formation of nanorods in the samples synthesised with 15 min stirring time even after calcination up to 800°C. But the samples synthesized with 8 h contact time show the presence of nanorods even at 300°C. This rules out the possibility of sintering playing a role at high temperature in the formation of different morphologies. UV-Visible studies of precursor mixed micelle composite show that there is shift of ligand to metal charge transfer band with change in CTAB concentration. This indicates that $[PtCl_6]^{2-}$-CTAB cluster complex diffuse and agglomerate with time and set the stage for the formation of different morphologies in the final material. This is also supported by NMR and IR studies.

3A.7. REFERENCES

1. B. Wiley, Y. Sun, B. Mayers, Y. Xia, *Chem.--Eur. J*. **2005**, *11*, 454.
2. B. J. Wiley, Y. Chen, J. M. McLellan, Y. Xiong, Z-Y. Li, D. Ginger, Y. Xia, *Nano Lett*. **2007**, *7*, 1032.
3. C. K. Kan, X. Zhu, G. Wang, *J. Phys. Chem. B* **2006**, *110*, 4651.
4. T. M. Whitney, J. S. Jiang, P. C. Searson, C. L. Chien, *Science* **1993**, *261*, 1316.
5. T. K. Sau, C. J. Murphy, *J. Am. Chem. Soc*. **2004**, *126*, 8648.
6. S. Shiv Shankar, A. Rai, B. Ankamwar, A. Singh, A. Ahmad, M. Sastry, *Nat. Mater.* **2004**, *3*, 482.
7. V. F. Puntes, K. M. Krishnan, A. P. Alivisatos, *Science* **2001**, *291*, 2115.
8. Y. Sun, Y. Xia, *Science* **2002**, *298*, 2176.
9. Y. Yin, R. M. Rioux, C. K. Erdonmez, S. Hughes, G. A. Somorjai, A. P. Alivisatos, *Science* **2004**, *304*, 711.
10. M. P. Pileni, *J. Phys. Chem. C* **2007**, *111*, 9019.
11. a) B. R. Martin, D. J. Dermody, B. D. Reiss, M. Fang, A. Lyon, M. J. Natan, T. E. Mallouk, *Adv. Mater.* **1999**, *11*, 1021. b) W. Lee, R. Scholz, K. Nielsch, K. Go¨sele, *Angew. Chem., Int. Ed.* **2005**, *44*, 6050. c) F. Liu, J. Y. Lee, W. J. Zhou, *Small* **2006**, *2*, 121. d) C. Xu, H. Wang, P. K. Shen, S. P. Jiang, *Adv. Mater.* **2007**, *19*, 4256.
12. a) M. Vaarkamp, B. L. Mojet, M. J. Kappers, J. T. Miller, D. C. Koningsbergert, *J. Phys. Chem.* **1995**, *99*, 16067. b) A. H. Lu, F. Schu¨th, *Adv. Mater.* **2006**, *18*, 1793.
13. R. Ryoo, J. M. Kim, C. H. Ko, C. H. Shin, *J. Phys. Chem.* **1996**, *100*, 17718.
14. H. J. Shin, R. Ryoo, Z. Liu, O. Terasaki, *J. Am. Chem. Soc.* **2001**, *123*, 1246.
15. M. H. Huang, A. Choudrey, P. Yang, *Chem. Commun.* **2000**, 1063.
16. Y. Kumai, H. Tsukada, Y. Akimoto, N. Sugimoto, Y. Seno, A. Fukuoka, M. Ichikawa, S. Inagaki, *Adv. Mater.* **2006**, *18*, 760.
17. a) D. Wang, H. Luo, R. Kou, M. P. Gil, S. Xiao, V. O. Golub, Z. Yang, C. J.

Brinker, Y. Lu, *Angew. Chem., Int. Ed.* **2004**, *43*, 6169. b) H. J. Shin, R. Ryoo, Z. Liu, O. Terasaki, *J. Am. Chem. Soc.* **2001**, *123*, 1246.

18. Y. Sakamoto, A. Fukuoka, T. Higuchi, N. Shimomura, S. Inagaki, M. Ichikawa, *J. Phys. Chem. B* **2004**, *108*, 853.

19. a) C. H. Ko, R. Ryoo, *Chem. Commun.* **1996**, 2467. b) C. Yang, P. Liu, Y. Ho, C. Chiu, K. Chao, *Chem. Mater.* **2003**, *15*, 275. c) C. Yang, H. Sheu, K. Chao, *Adv. Funct. Mater.* **2002**, *12*, 143.

20. Y. Zhang, F. L.-Y. Lam, X. Hu, Z. Yan, P. Sheng, *J. Phys. Chem. C* **2007**, *111*, 12536.

21. A. Fukuoka, Y. Sakamoto, S. Guan, S. Inagaki, N. Sugimoto, Y. Fukushima, K. Hirahara, S. Iijima, M. Ichikawa, *J. Am. Chem. Soc.* **2001**, *123*, 3373.

22. A. K. Prashar, R. P. Hodgkins, R. Kumar, R. N. Devi, *J. Mater. Chem.* **2008**, *18*, 1765.

23. S. J. Gibbs, C. S. Johnson, *J. Magn. Reson.* **1991**, *93*, 395.

24. J. Jansson, K. Schillen, G. Olofsson, R. Cardoso da Silva, W. J. Loh, *J. Phys. Chem. B* **2004**, *108*, 82.

25. B. Veisz, Z. Kiraly, *Langmuir* **2003**, *19,* 4817.

PART B

FINE TUNING OF SIZE OF PLATINUM NANOPARTICLES

3B.1. INTRODUCTION

As mentioned in chapter 1 section 1.2, developing methods for synthesizing nanoparticles has been the mainstay of nanotechnology. However, fine tuning size is also equally important, especially for exploiting size dependent properties of nanoparticles. Various methods to control the size of nanoparticles are reported in literature involving micelles (surfactant and polymers) [1-4], Langmuir-Blodgett [5], zeolites [6], two-phase liquid-liquid systems [7] and organometallic techniques [8]. Polyol method is one of the most efficient methods for controlling the size and shape of noble metal nanoparticles. This method involves reduction of metal salts by refluxing in a mixture of water and alcohol in the presence of PVP [9-11]. Here the size of the nanoparticles is controlled by changing the amount of PVP and the type or concentration of alcohol in solvent. In the *in situ* method we have developed for the synthesis of metal nanoparticles in SBA-15, channel size is the limiting factor for control of metal nanoparticle size by acting as moulds for their formation [12]. A logical extension is to employ mesoporous silica compounds with different channel/cavity size as moulds for controlling and fine tuning the size of nanoparticles. Various other SBA type materials like SBA-11, SBA-12, SBA-14 etc. which are templated by nonionic poly(ethylene oxide) surfactants, e.g. Brij 56 ($C_{16}EO_{10}$), Brij 76 ($C_{18}EO_{10}$) etc. are reported with pore size in the range of 3-5 nm which is smaller than SBA-15 [13]. These materials would be ideal for fine tuning the size of metal nanoparticles encapsulated within the channels. In these materials channel size is engineered by varying the template sizes.

The non-ionic copolymer Brij 76 ($C_{18}EO_{10}$) is used to synthesize mesoporous SBA-12 which was first reported by GD Stucky's group [13]. It was synthesized in acidic silica precursor of TEOS at room temperature. It was observed as hexagonal intergrowth with cubic close packing. The structure was found to be hexagonal when synthesized at higher temperatures. Later electron microscopy studies revealed that it has face centered cubic structure with each cage connected to adjacent one by twelve small windows [14]. We have synthesized Pt nanoparticles in the channels of SBA-12 using same strategy as in the case of SBA-15 [12]. To disperse the metal precursor inside the channels, Brij 76 is mixed with the cationic surfactant CTAB which helps in retaining the metal precursor in the mixed micelle composite because of electrostatic interaction of positively charged head group of ionic surfactant with the

negatively charged metal precursor. SBA-12 has been synthesized with different concentrations of CTAB in 4 wt% Brij 76 to study the effect of CTAB concentration on mesoporous SBA-12 and to find out the optimum concentration to incorporate platinum. To increase the loading of Pt in the mesoporous SBA-12, it has been synthesized with different concentrations of Pt precursor and CTAB. Effect of different concentration of CTAB on the retention of Pt and size of Pt nanoparticles has also been studied.

As described in chapter 2 section 2.5, Au tends to get reduced and agglomerated during the hydrothermal treatment (at 100°C) in the case of SBA-15. Final calcined Au/SBA-15 shows sintered Au nanoparticles as indicated by the XRD. To avoid the formation of nanoparticles in as-synthesized samples, we also synthesized Au/SBA-12 at room temperature without any hydrothermal treatment at higher temperature.

In addition to SBA-12, we also synthesized Pt nanoparticles in the three dimensional mesoporous material FDU-12 which has cubic macrostructure (Fm3m) with a large cavity of about 5 nm interconnected by smaller windows without the intergrowth of 3D hexagonal mesostructure [15,16]. Mesoporous FDU-12 samples were synthesized in acidic solutions by using nonionic block copolymer $EO_{106}PO_{70}EO_{106}$ also known as Pluronic F127 as a template, 1, 3, 5-trimethylbenzene (TMB) together with inorganic salts (e.g. KCl), as additives, and TEOS as the silica source. FDU-12 has been synthesized with different concentrations of CTAB in 1 wt% F127 to study the effect of CTAB concentration on mesoporous FDU-12 and to find out the optimum concentration to incorporate platinum.

3B.2. SYNTHESIS

3B.2.1. Synthesis of SBA-12 with Different Concentrations of CTAB

SBA-12 was prepared using Brij-CTAB composite with varying concentrations of CTAB in fixed amount of Brij 76 (Aldrich). The final molar composition of the reaction gel was 1 TEOS : 0.13 Brij 76 : 1.5 HCl : 139 H_2O : 0-0.16 CTAB. Typically, CTAB was added to 50 g of 4 wt% solution of nonionic surfactant Brij 76 and this mixture was stirred for 24 h at 35-40^oC and kept overnight for stabilization at room temperature. This solution was made acidic (pH < 2) by adding 3 g of conc. HCl (37%). After 3 h, 4.25 g of TEOS was added under stirring.

Stirring was continued for another 24 h at 40^{o}C and then autoclaved at 100^{o}C for 48 h. The product was filtered, washed and dried at 70^{o}C for 24 h. The CTAB concentration was progressively increased to 64 mM in 4 wt% Brij 76 for different samples. As-synthesized material was calcined to remove the polymer and surfactant by heating with a rate of 0.8^{o}C/min from room temperature to 450^{o}C under nitrogen flow. Then temperature was increased to 500^{o}C with the same heating rate under air flow and material was kept at this temperature for 12 h.

3B.2.2. Synthesis of Pt/SBA-12

The final molar composition of the reaction gel used for Pt/SBA-12 was 1 TEOS : 139 H_2O : 1.5 HCl : 0.13 Brij 76 : 0.005-0.08 CTAB : 0.0025-0.0125 H_2PtCl_6. Typically, CTAB was added to 50 g of 4 wt% solution of nonionic surfactant Brij 76 so that the final concentration was 2 mM of CTAB and this mixture was stirred for 24 h at 40^{o}C and kept overnight for stabilization at room temperature. For Pt incorporation, 2.6 mL of 0.019 M solution of $H_2PtCl_6.6H_2O$ was added to the Brij–surfactant composite solution and stirred for 24 h at 40°C. This solution was made acidic (pH < 2) by adding 3 g of conc. HCl (37%). After 3 h, 4.25 g of TEOS was added under stirring. Stirring was continued for another 24 h at 40^{o}C and then the whole gel was autoclaved at 100^{o}C for 48 h. The product was filtered, washed, dried and calcined by the same procedure as mentioned in section 3B.2.1. Similarly, Pt/SBA-12 was synthesized with different wt% loading of platinum by varying the concentration of $H_2PtCl_6.6H_2O$ and CTAB.

3B.2.3. Synthesis of Au/SBA-12

The final molar composition of the gel was 1 TEOS : 139 H_2O : 1.5 HCl : 0.13 Brij 76 : 0.005 CTAB : 0.0025 $HAuCl_4$**.** Typically, CTAB was added to 50 g of 4 wt% solution of nonionic surfactant Brij 76 so that the final concentration was 2 mM of CTAB and this mixture was stirred for 24 h at 35-40^{o}C and kept overnight for stabilization at room temperature. For Au incorporation, 3.58 mL of 0.027 M solution of $HAuCl_4.H_2O$ was added to the Brij–surfactant composite solution and stirred for 24 h at 40^{o}C. This solution was made acidic (pH < 2) by adding 3 g of conc. HCl (37%). After 3 h, 4.25 g of TEOS was added under stirring. Stirring was continued for another 24 h at 40-45^{o}C. The product was filtered, washed, dried and calcined

(procedure mentioned in section 3B.2.1.) at 500^{o}C for 12 h for enabling the template removal.

3B.2.4. Synthesis of FDU-12 with Different Concentrations of CTAB

FDU-12 was prepared using F127-CTAB composite with varying concentrations of CTAB in fixed amount of triblock copolymer Pluronic F127 (Aldrich). The final molar composition of the reaction gel was 1 TEOS : 0.0039 F127 : 0.55 TMB : 1.7 KCl : 5 HCl : 275 H_2O : 0-0.08 CTAB. Typically, CTAB was added to 100 g of 1 wt% solution of Pluronic F127 and this mixture was stirred for 24 h at 35-40^{o}C and kept overnight for stabilization at room temperature. To this solution, 2.5 g of KCl and 1 g TMB was added after small gap of time while stirring at 40^{o}C. This solution was made acidic (pH < 2) by adding 10 g of conc. HCl (37%). After 24 h, 4.25 g of TEOS was added under stirring. Stirring was continued for another 24 h at 40^{o}C and then autoclaved at 100^{o}C for 72 h. The product was filtered, washed, dried and calcined (procedure mentioned in section 3B.2.1) at 500^{o}C for 12 h for enabling the template removal. The CTAB concentration was progressively increased to 32 mM in 1 wt% F127 for different samples.

3B.2.5. Synthesis of Pt/FDU-12

The final molar composition of the gel was 1 TEOS : 275 H_2O : 1.7 KCl : 0.55 TMB : 5 HCl: 0.0039 F127: 0.005 CTAB: 0.0025 H_2PtCl_6. Typically, CTAB was added to 100 g of 1 wt% solution of Pluronic F127 so that the final concentration was 2 mM of CTAB and this mixture was stirred for 24 h at 35-40^{o}C and kept overnight for stabilization at room temperature. For Pt incorporation, 2.6 mL of 0.019 M solution of $H_2PtCl_6.6H_2O$ was added to the F127–surfactant composite solution and stirred for 24 h at 40°C. To this solution 2.5 g of KCl and 1 g TMB was added after small gap of time while stirring at 40^{o}C. This solution was made acidic (pH < 2) by adding 10 g of conc. HCl (37%). After 24 h, 4.25 g of TEOS was added under stirring. Stirring was continued for another 24 h at 40^{o}C and then autoclaved at 100^{o}C for 72 h. The product was filtered, washed, dried and calcined (procedure mentioned in section 3B.2.1) at 500^{o}C for 12 h for enabling the template removal.

3B.3. CHARACTERIZATION

3B.3.1. Characterization of Precursor Mixed Micelle Composite

Nonionic surfactants like Brij 76 are known to form mixed micelles with ionic surfactants (e.g. CTAB) in aqueous solution. They are arranged in such a way that charged head groups of ionic surfactants with three alkyl groups are located in the corona among the oxyethylene groups of the nonionic surfactants and the hydrophobic alkyl chains of both are co-aggregated in the mixed micellar core [17, 18]. For the ionic surfactants the micelle formation is governed by the balance between the tendency of alkyl chain to avoid contact with water and electrostatic repulsion between the head groups, whereas for nonionic surfactant the tendency of alkyl chain to avoid contact with water is balanced by hydration and space requirement of the poly (ethylene oxide) chains [18]. Intermiceller interactions also play role in the stability of mixed micelle with increase in ionic surfactant concentration in the mixed micelle. On addition of the platinum precursor H_2PtCl_6, the electrostatic interaction directs the $[PtCl_6]^{2-}$ towards the cationic head groups and an ion exchange with the counter anions of the surfactant are possible. These interactions are similar to that of P123-CTAB mixed micelle. However, the main difference lies in the enhanced hydrophobicity of alkyl chains in Brij 76 when compared to PPO chains in P123. This is advantageous since it can be envisaged that the solubility of CTAB alkyl chains is higher in Brij 76 core than in P123 core. Hence more amounts of CTAB can be expected to be entrapped in the mixed micelle system, forming a more stable system than P123-CTAB mixed micelle. This system can also be expected to be more stable towards addition of Pt salts. These aspects are further investigated by ^{1}H NMR and UV-Vis spectroscopic studies.

3B.3.1.1. NMR Studies

We studied the changes, i.e. addition of Brij 76 to CTAB and addition of platinum precursor to the mixed micelle system with NMR spectroscopy. ^{1}H NMR studies were done with 2 mM solution of CTAB which is above its CMC value (0.8 mM), mixed micelle system containing 4 wt% Brij 76 and 2 mM CTAB and H_2PtCl_6-Brij-CTAB system containing 2 mM CTAB, 4 wt% Brij 76 and 1 mM $H_2PtCl_6.6H_2O$. To confirm that obtained chemical shifts are due to the changes in chemical environment, all the solutions were made in D_2O containing 1% standard 3-

(Trimethylsilyl) propionic acid (d_4) sodium salt which have fixed chemical shift value for its protons. A comparison of ^{1}H NMR spectra of neat CTAB, neat Brij 76, Brij-CTAB and H_2PtCl_6-Brij-CTAB system is given in Fig. 3B.1. To study the changes occurring in CTAB environment after the addition of Brij 76, we closely observed the head methyl groups of CTAB (Fig. 3B.2).

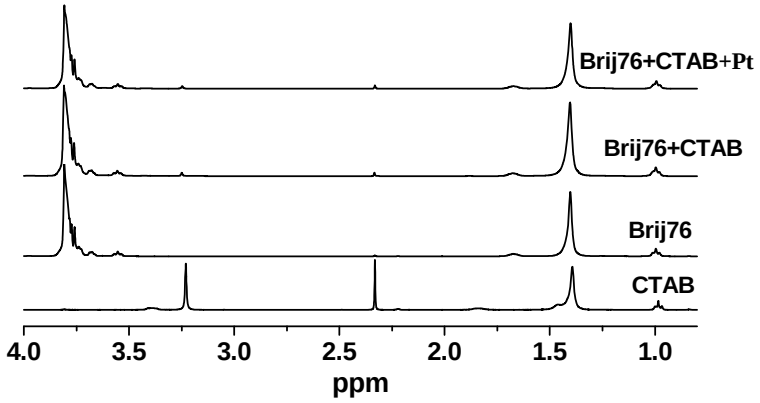

Fig. 3B.1. Comparison of 400 MHz ^{1}H NMR spectrum of CTAB, Brij 76, CTAB-Brij 76 mixed micelle and H_2PtCl_6-Brij-CTAB system.

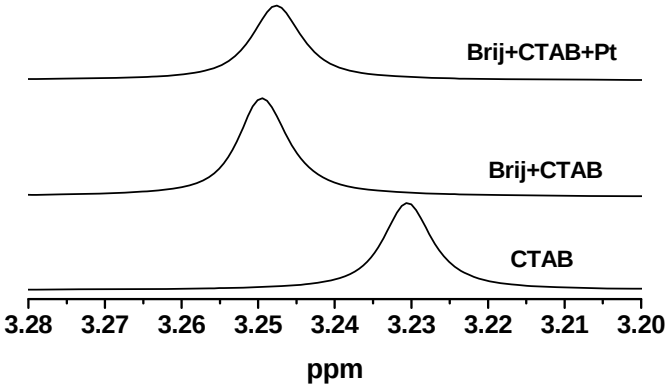

Fig. 3B.2. ^{1}H Chemical shift changes observed for the protons of head methyl groups of CTAB in neat CTAB, CTAB-Brij 76 mixed micelle and H_2PtCl_6-Brij-CTAB system.

There is small downfield shift from 3.23 ppm to 3.25 ppm indicating that the molecules are not present in the micelle form anymore but assumes a cooperative structure interacting with the hydrophobic region of Brij 76. Changes in tail methyl group could not be followed because there is overlap in signals coming from methyl group of both CTAB and Brij 76. Addition of H_2PtCl_6, however, does not lead to any substantial change but only a slight up field shift. This shows that the CTAB-Brij 76

composite structure is unchanged by the addition of the Pt precursor and that the precursor is interacting with CTAB.

3B.3.1.2. UV-Vis Spectroscopic Studies

To understand the interaction of Pt precursor with CTAB-Brij76 composite further, UV-Vis spectroscopic studies were carried out. The concentration of CTAB in 4 wt% Brij 76 was progressively increased from 0.25 mM to 4 mM and 0.5 mM H_2PtCl_6 was added to each of these solutions before measuring UV absorption. It is found that the peak at 259 nm attributed to ligand to metal charge transfer in $[PtCl_6]^{2-}$, decreases with increase in CTAB concentration (Fig. 3B.3). Above 1 mM, this band completely disappears and at 4 mM, a new red shifted band at 280 nm appears which is indicative of interaction with CTAB and the formation of CTAB-$PtCl_6$ ion pairs.

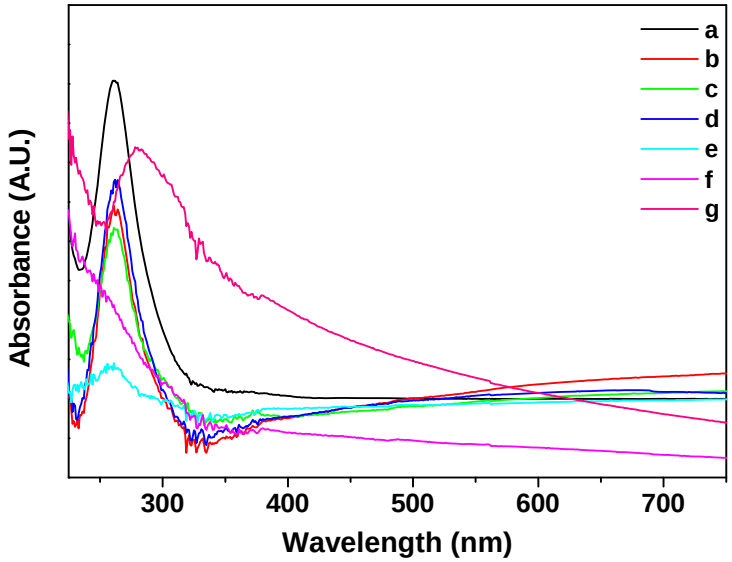

Fig. 3B.3. UV-Vis spectra of a) 0.5 mM $H_2PtCl_6.6H_2O$ and its mixture with b) 4 wt% Brij 76, and c) 0.25 mM, d) 0.5 mM, e) 1 mM, f) 2 mM and g) 4 mM CTAB.

3B.3.2. Effect of Different Concentrations of CTAB on SBA-12

As these studies indicate a definite cooperative interaction of CTAB with the polymer and show that Pt precursor exists in bound state to CTAB in the mixed micelle, these composite micelles could be regarded as ideal for utilizing as templates for mesoporous silica formation. However, the formation and pore structure of the mesoporous silica is highly sensitive to the stability and structure of the template micelles. It is known that increasing concentrations of the ionic surfactant deteriorates

the polymer micelle structure which in turn affects the porous structure and crystallinity of the final mesoporous silica. To optimize the concentration of CTAB to be used, composite micelles of 4 wt% Brij 76 and 2, 4, 8, 16, 32 and 64 mM CTAB were prepared and these composite micelles were used as templates for the synthesis of mesoporous SBA-12. All the materials were characterized by XRD, N_2 adsorption and SEM.

3B.3.2.1. Powder X-Ray Diffraction

XRD studies were carried out to study the effect of CTAB concentration on the mesoporous structure of SBA-12 materials. The mesopore order of the materials was surprisingly intact even at a CTAB concentration of 32 mM, although, there is disappearance of higher angle reflections (110 and 200) in SBA-12 samples synthesized with CTAB concentration more than 2 mM (Fig. 3B.4). A gradual shift in (100) reflection peak position is observed at 2θ value 1.77 for SBA-12 samples synthesized without CTAB to a 2θ value 2.2 for SBA-12 synthesized with 64 mM CTAB (Table 3B.1).

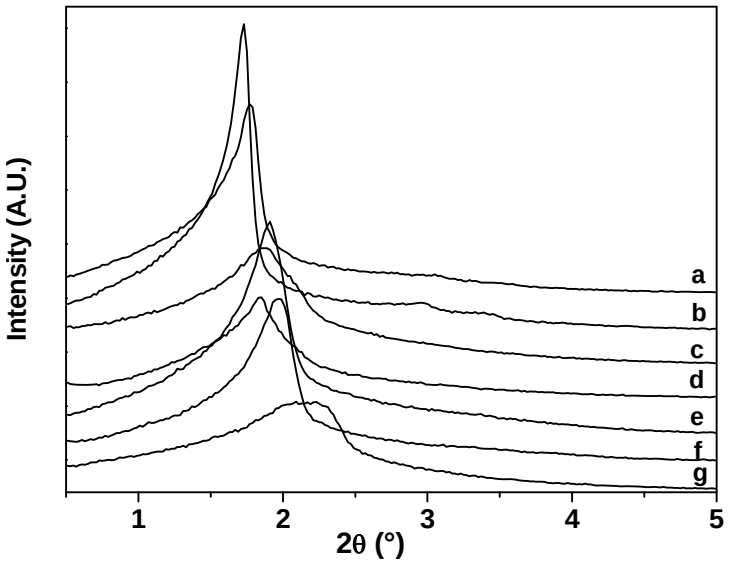

Fig. 3B.4. Low angle XRD pattern of SBA-12 samples with different concentrations of CTAB; a) without CTAB, b) 2 mM CTAB, c) 4 mM CTAB, d) 8 mM CTAB, e) 16 mM CTAB, f) 32 mM CTAB and g) 64 mM CTAB.

Table 3B.1. Lattice parameters and unit cell values for SBA-12 materials synthesized with different concentrations of CTAB in 4 wt% Brij 76.

CTAB Concentration (mM)	2θ (°)	d_{100} (Å)	Unit Cell (Å)
-	1.77	49.91	57.40
2	1.72	51.36	59.06
4	1.86	47.49	54.62
8	1.84	48.01	55.21
16	1.91	46.25	53.19
32	1.99	44.39	51.05
64	2.2	40.16	46.18

Unit cell values were calculated from (100) reflections based on hexagonal lattice parameters, $a = \sqrt{4/3}\, d_{100}$ and found to decreases with increase in CTAB concentration. We decided to index the reflections in hexagonal system since no evidence of a cubic cell could be observed in XRD pattern or in TEM (given in section 3.3.3.4). We did not observe any particular trend in intensity of materials. Retaining of mesoporous structures even in the samples with higher conc. of CTAB can be attributed to the stability of the Brij-CTAB mixed micelle composite which may be due to the greater hydrophobicity of the hydrocarbon chain of Brij 76 which can accommodate higher concentration of CTAB. This, we did not observe in case of SBA-15 in which CTAB destabilizes P123 micelle at very low concentrations.

3B.3.2.2. N_2 Adsorption Studies

All the mesoporous SBA-12 materials show type IV isotherms which is the characteristic of mesoporous solids (Fig. 3B.5). The steep increase in N_2 adsorption (in the p / p_o range of 0.3 to 0.5) corresponds to capillary condensation within uniform cylindrical pores. As clear from the adsorption isotherms, steepness of the curves decreases with increase in CTAB concentration indicating much uneven distribution of pores as CTAB concentration increases in the mixed micelle composite.

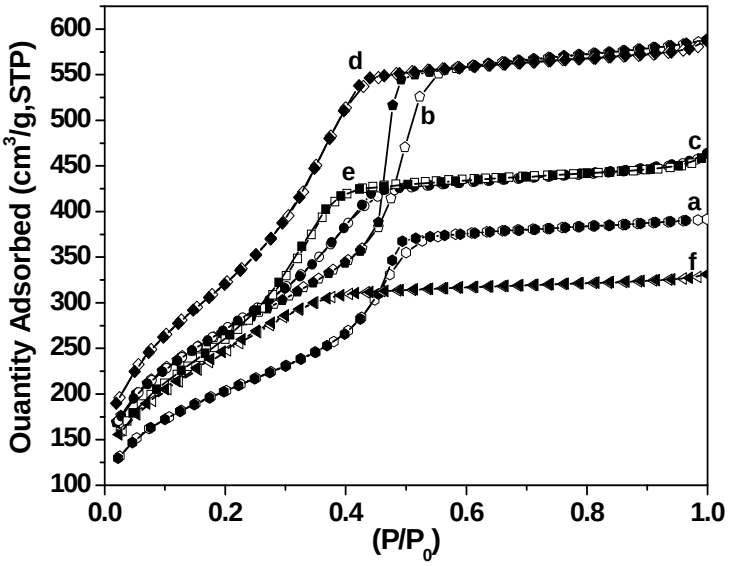

Fig. 3B.5. Adsorption isotherms of SBA-12 materials synthesized with different conc. of CTAB in 4 wt% Brij 76; a) without CTAB, b) 2 mM CTAB, c) 8 mM CTAB, d) 16 mM CTAB, e) 32 mM CTAB and f) 64 mM CTAB.

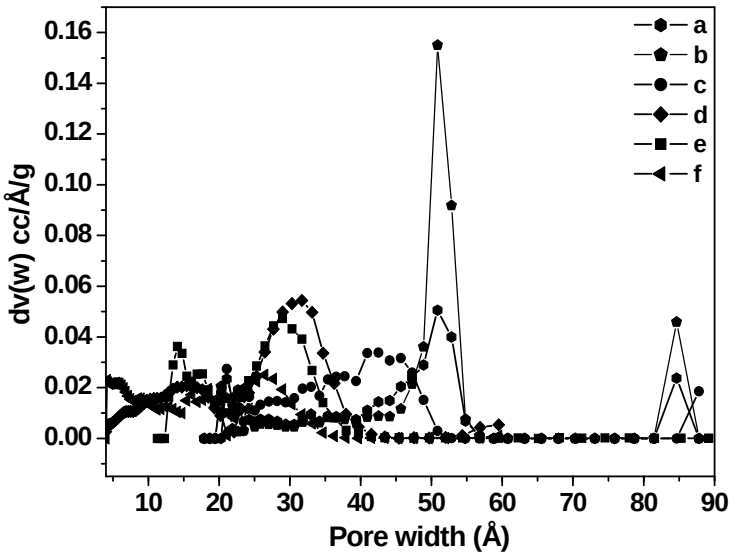

Fig. 3B.6. Pore size distributions of SBA-12 materials synthesized with different concentrations of CTAB in 4 wt% Brij 76; a) without CTAB, b) 2 mM CTAB, c) 8 mM CTAB, d) 16 mM CTAB, e) 32 mM CTAB and f) 64 mM CTAB.

This is also clear from the pore size distribution in Fig. 3B.6. Overall pore size distribution in the materials calculated by DFT method shows that there is decrease in pore size with increase in CTAB concentration in the mixed micelle composite (Table 3B.2). However the surface area of the samples shows no trend.

Table 3B.2. Unit cell values (from XRD) and N_2 adsorption measurements of SBA-12 materials synthesized with different concentrations of CTAB in 4 wt% Brij 76.

CTAB Concentration (mM)	Unit Cell (Å)	Pore size (Å)	BET (m^2/g)	N_2 Uptake (cm^3/g STP)	Total Pore Volume (cm^3/g)	Micropore Volume (cm^3/g)
-	57.4	50.8	739	392	0.6	0.023
2	59.06	50.8	972	588	0.91	0.867
8	55.21	42.5	972	463	0.72	0.65
16	53.19	31.7	1094	587	1.01	-
32	51.05	28.9	908	458	0.73	-
64	46.18	26.4	856	331	0.51	0.45

3B.3.2.3. Scanning Electron Microscopy

SBA-12 materials were characterized by SEM to study the effect of different concentration of CTAB in mixed micelle on the final morphology of the materials. Calcined SBA-12 materials do not show any particular morphology. Particle size varies from 0.5 to 10 μm in all samples. Some bigger particles are also observed. Particle size distributions of SBA-12 samples synthesized with different concentration of CTAB in Brij 76 are given in Fig. 3B.7. It is very difficult to say whether varying concentration of CTAB has any impact on the final morphology of the materials. But SBA-12 synthesized with 64 mM CTAB also shows some spherical particles along with irregular shaped particles with size varying from 1-4 μm.

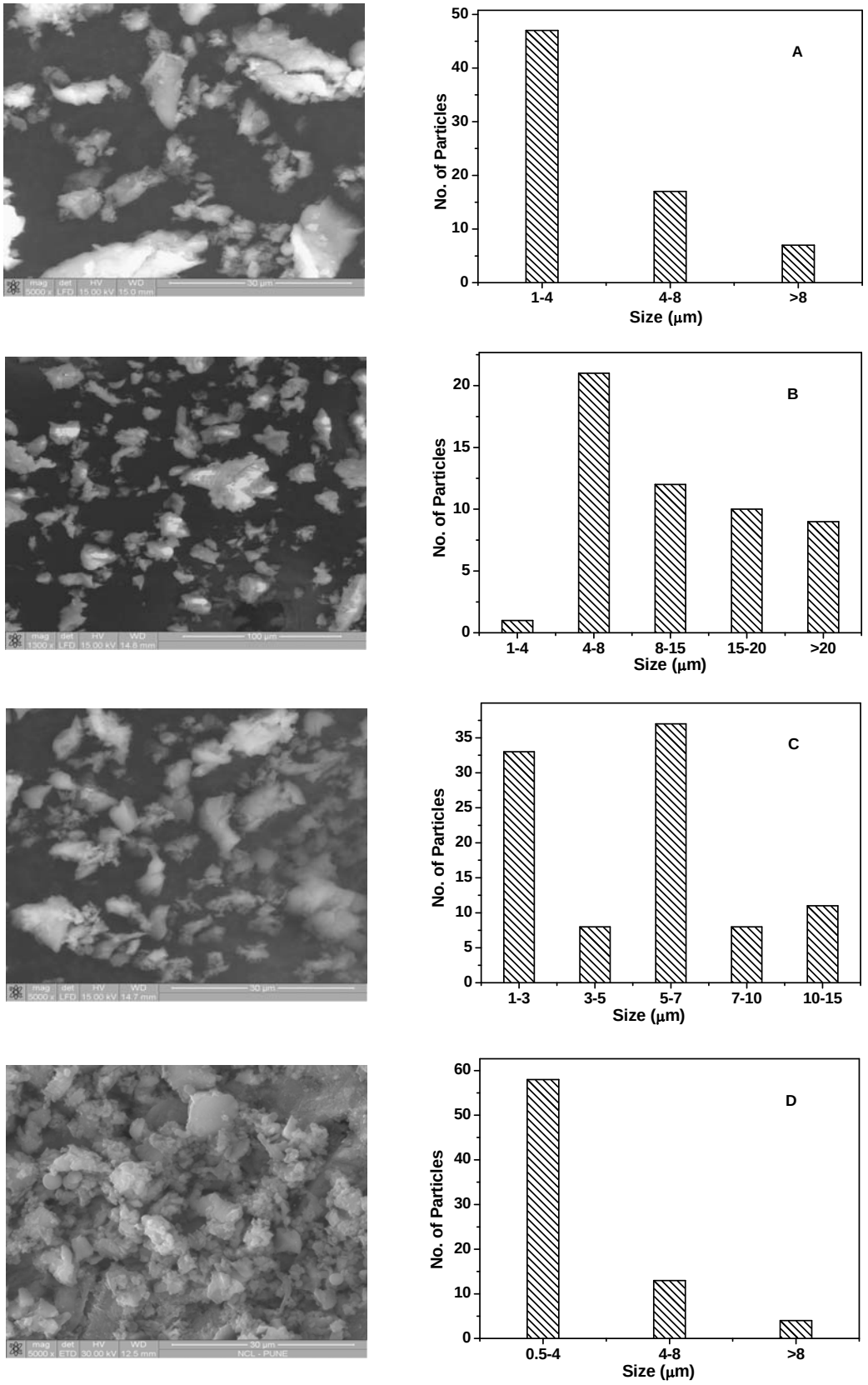

Fig. 3B.7. SEM images and particle size distribution of various SBA-12 materials synthesized with different concentration of CTAB in 4 wt% Brij 76; A) w/o CTAB, B) 16 mM CTAB, C) 32 mM CTAB and D) 64 mM CTAB.

3B.3.3. Effect of Incorporation of Pt in SBA-12

As we observed a decrease in pore size of final SBA-12 materials with increase in CTAB concentrations it is logical to assume that size of platinum particles can be further controlled just by increasing the CTAB concentration. To study the effect of CTAB concentration on the particle size, Pt/SBA-12 was synthesized with varying concentrations of CTAB and more or less same concentrations of platinum precursor. As we saw in section 3.3.2 that mesoporous order of SBA-12 is retained even up to 32 mM CTAB, so we also studied the effect of increased loading of platinum on the particle size. To study this effect, we synthesized Pt/SBA-12 with increased concentration of CTAB and platinum precursor in mixed micelle composite. Since we expected an electrostatic interaction between CTAB and $[PtCl_6]^{2-}$, so CTAB/H_2PtCl_6 molar ratio was always kept more than 2. For this study, we synthesized Pt/SBA-12 with 8 mM CTAB and 16 mM CTAB containing 2.7 mM and 5.25 mM platinum precursor respectively in precursor mixed micelle composite. All the materials containing Pt dispersed in mesoporous channels of SBA-12 were characterized by XRD, N_2 adsorption, TEM, SEM, EDAX and elemental mapping. Platinum content in all samples was analyzed by ICP technique.

3B.3.3.1. Powder X-Ray Diffraction

Low angle XRD studies show that mesoporous order of the SBA-12 remains intact after the incorporation of Pt (Fig. 3B.8). A slight shift of the mesoporous unit cell parameters occurred by the inclusion of Pt when compared to the mesoporous materials prepared without platinum (Table 3B.1 and 3B.3). Unit cell values were calculated from hexagonal lattice parameter; $a = \sqrt{4/3}\, d_{100}$ where d_{100} was calculated from Bragg's equation. All the samples containing Pt show crystallinity and mesoporous order comparable to samples synthesized with mere CTAB in Brij 76. Scanning at high angles show reflections at 2θ value 39.7, 46.2, 67.5 and 81.2 corresponding to (111), (200), (220) and (311) planes indicative of Pt(0) (Fig. 3B.9). The peaks become less broad as Pt loading increases. This is an indication of increase in Pt particle size with increase in loading of Pt.

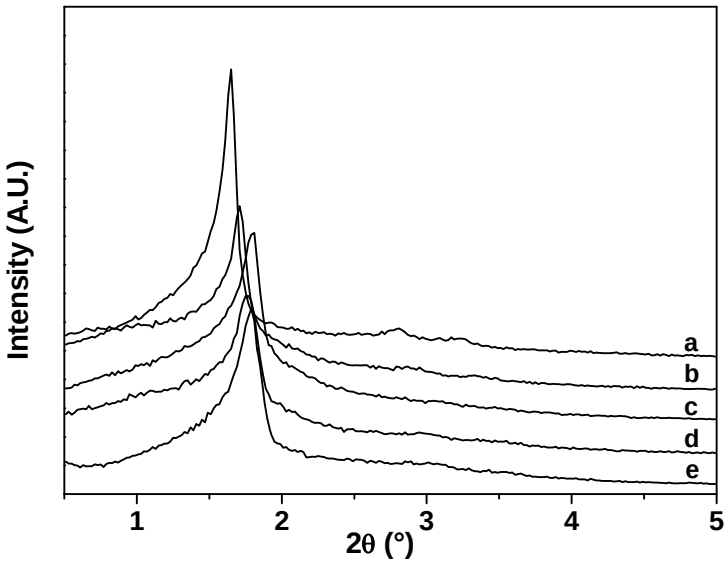

Fig. 3B.8. Low angle XRD of calcined SBA-12 samples synthesized with different concentrations of CTAB and Pt; a) 2 mM CTAB with 1 mM Pt, b) 8 mM CTAB with 2.7 mM Pt, c) 16 mM CTAB with 0.62 mM Pt, d) 16 mM CTAB with 5.25 mM Pt and e) 32 mM CTAB with 1.32 mM Pt.

Table 3B.3. Lattice parameters and unit cell values for SBA-12 materials synthesized with different concentrations of CTAB and Pt in 4 wt% Brij 76.

CTAB (mM)	Pt (mM)	2θ (°)	d_{100} (Å)	Unit Cell (Å)
2	1	1.65	53.54	61.57
8	2.7	1.7	51.96	59.76
16	0.61	1.79	49.35	56.76
16	5.25	1.74	50.77	58.39
32	1.32	1.79	49.35	56.76

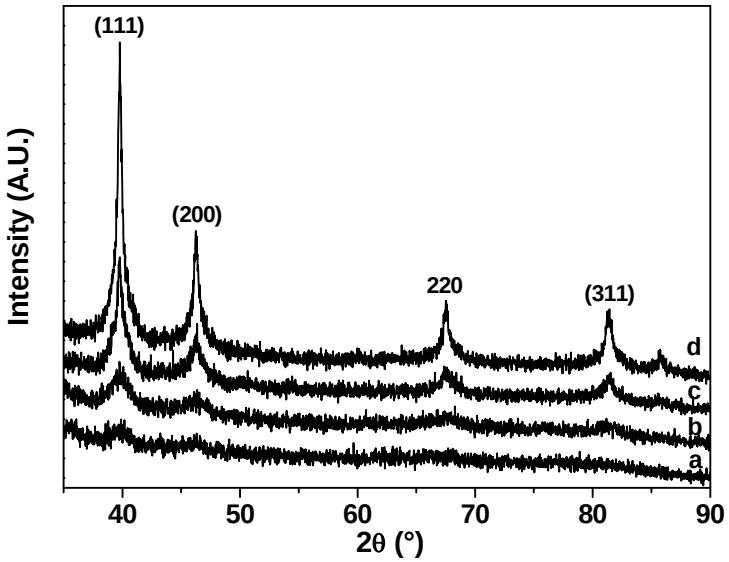

Fig. 3B.9. Wide angle XRD of calcined SBA-12 samples synthesized with different concentration of CTAB and Pt; a) 2 mM CTAB with Pt (0.42%), b) 32 mM CTAB with Pt (0.72%), c) 8 mM CTAB with Pt (1.49%), d) 16 mM CTAB with 5.25 mM Pt (3.6%).

3B.3.3.2. N_2 Adsorption Studies

All the materials show type IV isotherms with H1 hysteresis loop confirming the presence of cylindrical mesopores. Adsorption isotherms and DFT pore size distribution of SBA-12 materials synthesized with 2 mM CTAB and 1 mM Pt, with 8 mM CTAB and 2.7 mM Pt, with 16 mM CTAB and 5.25 mM Pt and with 32 mM CTAB and 1.32 mM Pt are given in Fig. 3B.10 and 3B.11, respectively. A comparison of Pt incorporated samples with only CTAB modified SBA-12 samples shows that Pt incorporation has led to increased surface area and overall adsorption capability (Table 3B.2 and 3B.4).There is increase in pore size also with incorporation of Pt. This expansion of pores with incorporation of Pt is an indication that platinum has been incorporated in the pores.

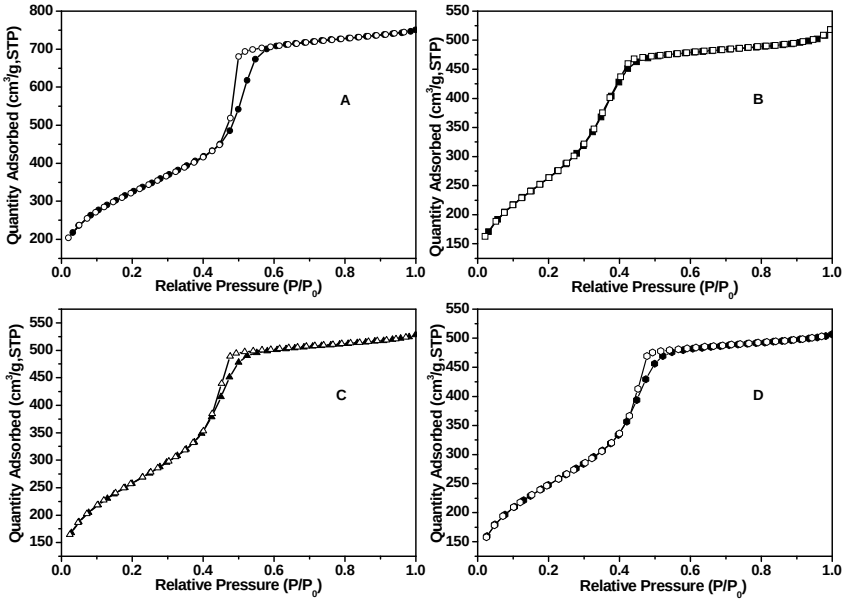

Fig. 3B.10. Nitrogen adsorption isotherms of SBA-12 samples synthesized with different concentrations of CTAB and Pt; A) 2 mM CTAB with 1 mM Pt, B) 8 mM CTAB with 2.7 mM Pt, C) 16mM CTAB with 5.25 mM Pt, D) 32 mM CTAB with 1.32 mM Pt.

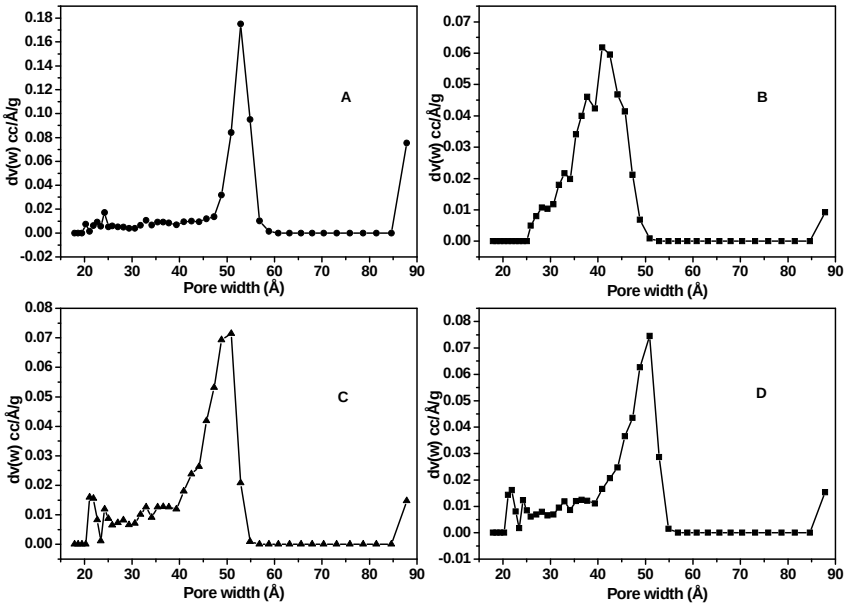

Fig. 3B.11. Pore size distribution of SBA-12 samples synthesized with different concentrations of CTAB and Pt; A) 2 mM CTAB with 1 mM Pt, B) 8 mM CTAB with 2.7 mM Pt, C) 16 mM CTAB with 5.25 mM Pt, D) 32 mM CTAB with 1.32 mM Pt.

Table 3B.4. N_2 adsorption measurements of SBA-12 materials synthesized with different concentrations of CTAB and Pt in 4 wt% Brij 76.

CTAB (mM)	Pt (mM)	Pore size (Å)	BET (m^2/g)	N_2 Uptake (cm^3/g STP)	Total Pore Volume (cm^3/g)	Micropore Volume (cm^3/g)
2	2	52.8	1172	750	1.2	-
8	2.7	40.9	936	518	0.86	0.71
16	5.25	50.8	935	527	0.87	0.73
32	32	50.8	892	506	0.84	0.68

3B.3.3.3. ICP Analysis: Effect of CTAB Concentration on Platinum Retention

Platinum amount in all the Pt containing samples was analyzed by ICP-OES technique. CTAB helps in retaining the Pt in the mesoporous SBA-12 as compared to samples synthesized with neat Brij 76. As clear from the table, there is very small retention (16%) of Pt in samples synthesized without CTAB as compared to samples synthesized with CTAB. Increase in CTAB concentration increases the percentage of Pt retention (Table 3B.5); it increases from 50% in case of 2 mM CTAB and 1 mM Pt to 68% in case of 32 mM CTAB and 1.32 mM Pt and 96% in case of 16 mM CTAB and 0.61 mM Pt.

Table 3B.5. Loading of Pt (wt %) on various Pt/SBA-12 materials synthesized with different concentration of CTAB and Pt.

CTAB (mM)	Pt (mM)	Theoretical (Wt %)	ICP analysis Actual (Wt %)	% Retention
-	0.5	0.4	0.065	16
2	1	0.8	0.4	50
2	1.3	1.05	0.71	68
16	0.61	0.49	0.47	96
32	1.32	1.05	0.72	69
8	2.7	2.13	1.49	70
16	5.25	4.1	3.6	88

3B.3.3.4. High Resolution Transmission Electron Microscopy

All the Pt containing SBA-12 materials were characterized by HRTEM. TEM images of Pt containing samples show nice distribution of Pt particles in the channels of mesoporous materials. Pt/SBA-12 synthesized with 2 mM CTAB and 1 mM Pt shows the presence of Pt particles varying from size 4-4.5 nm. A small number of particles (20%) with bigger size (from 4.5 to 5.5 nm) are also observed (Fig. 3B.12). Average size of particles was found to be 4.4 nm. In the Pt/SBA-12 samples synthesized with 32 mM CTAB, size of 90% of the particles is within the range of 3.5 to 5.5 nm but particles with size > 5.5 nm are also present while average size was 4.9 nm (Fig. 3B.15). But samples with higher loading of platinum synthesized with more amount of CTAB in Brij 76 shows particles of various sizes outside the channels also (Fig. 3B.13 & 14). This may be due to the reason that at higher concentration of CTAB, some independent micelle structure is formed along with the mixed micelle and this leads to formation of poorly ordered silica. Platinum interacting with these CTAB molecules may lead to formation of agglomerated Pt particles which are seen outside the channels.

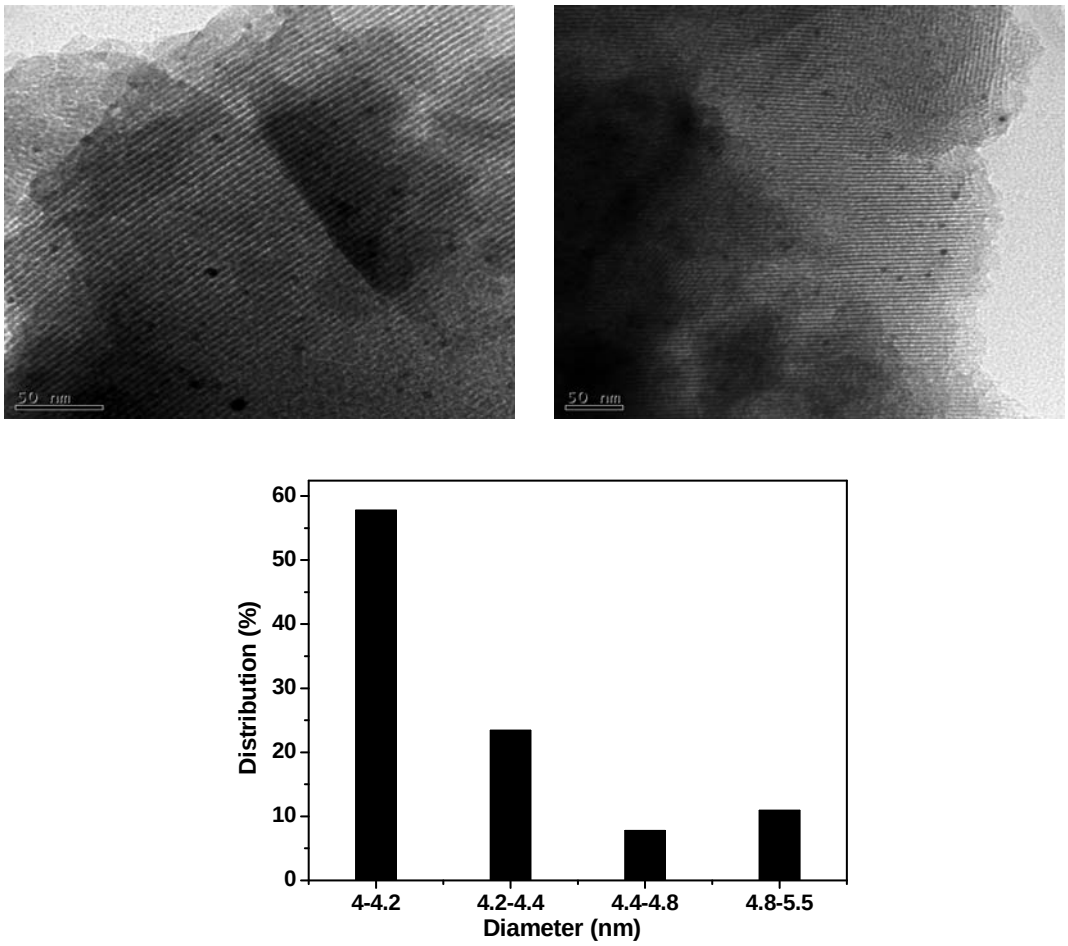

Fig. 3B.12. TEM images and particle size distribution of Pt/SBA-12 (0.41 wt%) with 2 mM CTAB and 1 mM Pt in 4 wt% Brij 76.

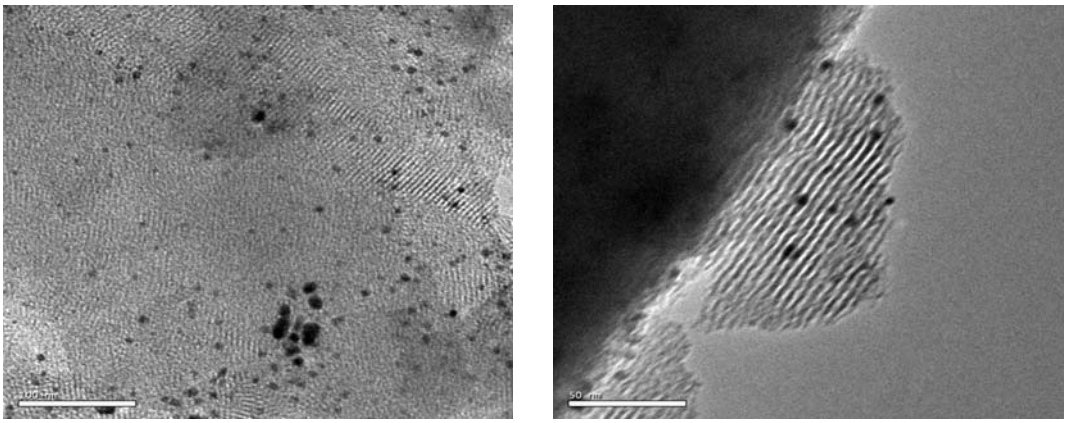

Fig. 3B.13. TEM images of Pt/SBA-12 (1.49 wt%) with 8 mM CTAB and 2.7 mM Pt in 4 wt% Brij 76.

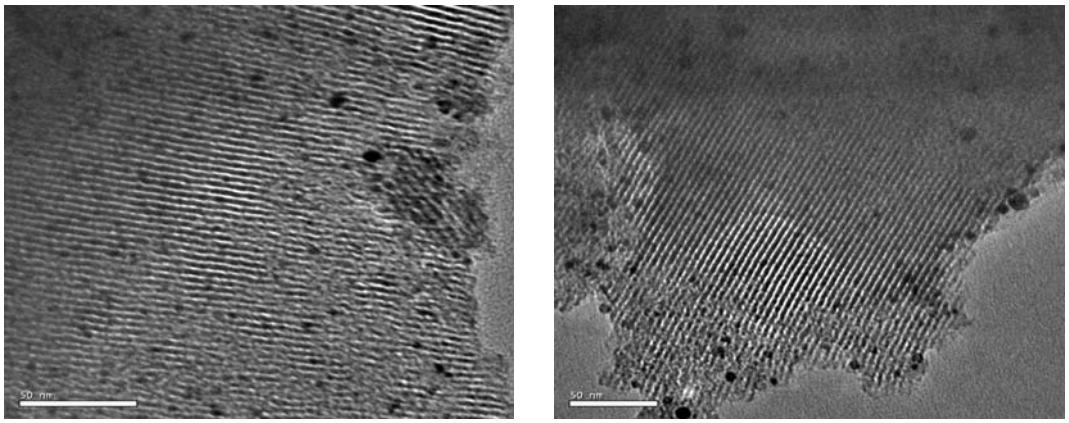

Fig. 3B.14. TEM images of Pt/SBA-12 (3.6 wt%) with 16 mM CTAB and 5.25 mM Pt in 4 wt% Brij 76.

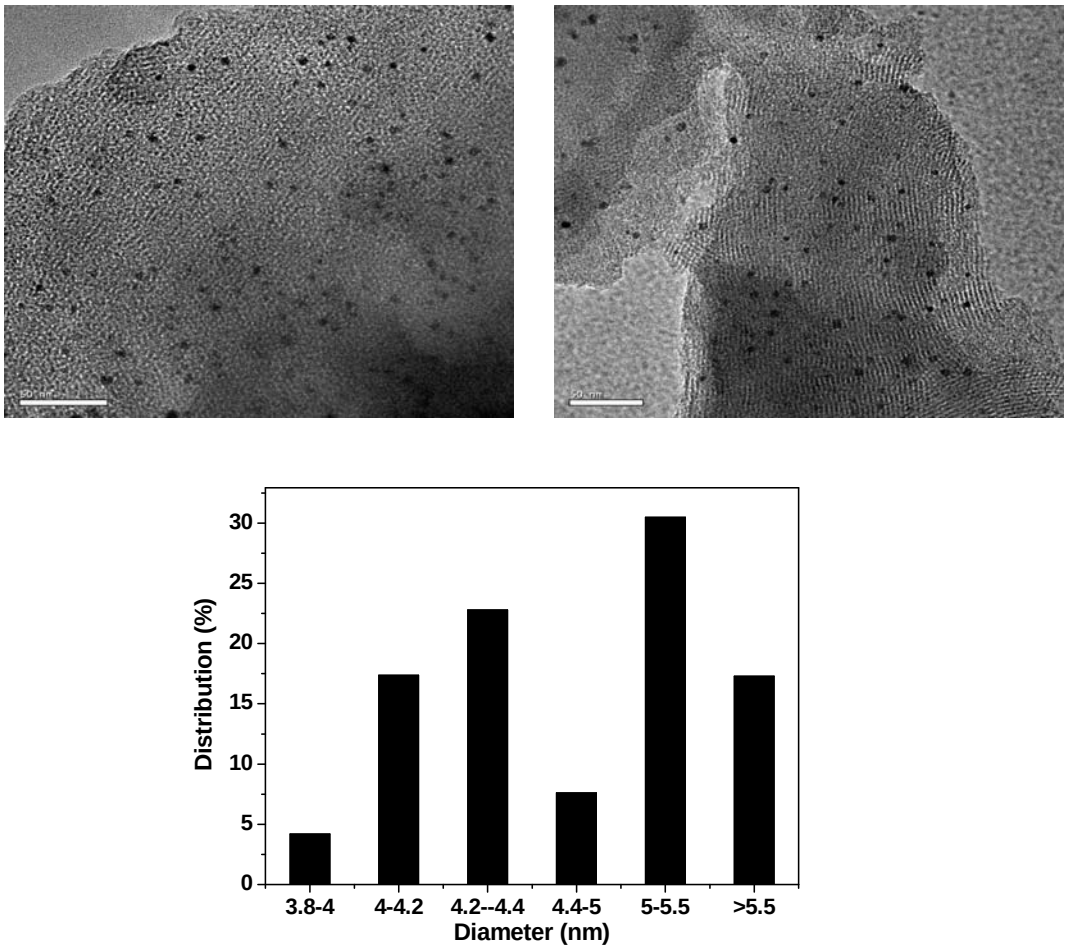

Fig. 3B.15. TEM images and particle size distribution of Pt/SBA-12 (0.72 wt%) with 32 mM CTAB & 1.32 mM Pt in 4 wt% Brij 76**.**

3B.3.3.5. Scanning Electron Microscopy and EDAX Analysis

Morphology of the samples does not show any particular trend as in case of samples without platinum. Particles are of irregular morphology with size varying from 0.5 to 9 μm are observed in Pt/SBA-12 samples. SEM images are given in Fig. 3B.16 and Fig. 3B.17 for Pt/SBA-12 materials synthesized with 2 mM CTAB and 32 mM CTAB, respectively.

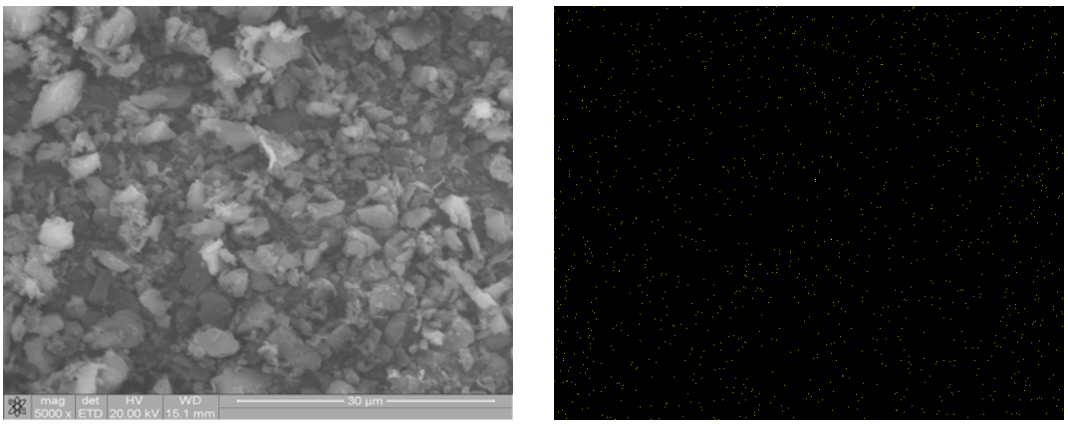

Fig. 3B.16. SEM image and Pt mapping of Pt/SBA-12 synthesized with 2 mM CTAB and 1 mM Pt.

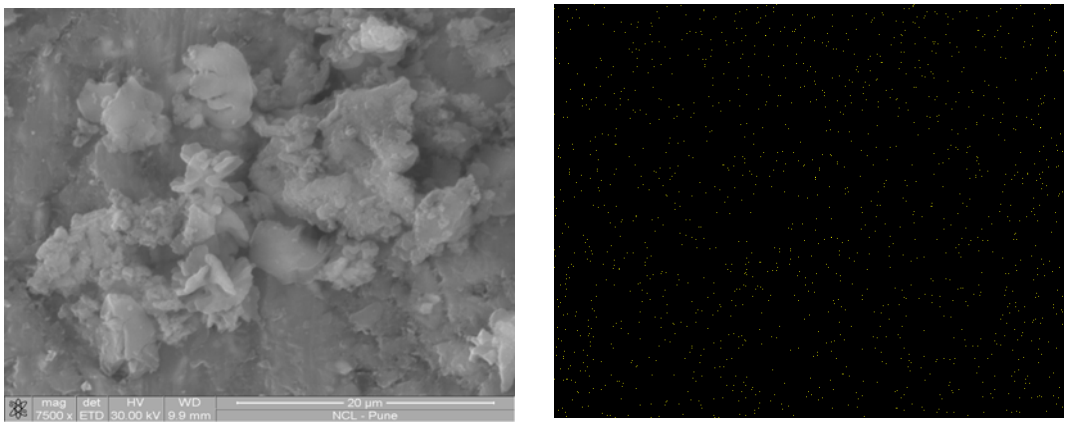

Fig. 3B.17. SEM image and Pt mapping of Pt/SBA-12 synthesized with 32 mM CTAB and 1.32 mM Pt.

It was observed in TEM that from some of the images of Pt/SBA-12 samples, loading of Pt appeared to be larger than the overall loading which we observed with ICP analysis. This raises the question of uniformity of the dispersion of Pt nanoparticles. To address this issue, elemental mapping by EDAX was carried out on some Pt containing SBA-12 samples (Fig. 3B.16 &17).The distribution of Pt and Si was observed in the area of 200 μm^2. The platinum mapping clearly shows that the

distribution is uniform within a resolution of 1-3 μm. Hence we can conclude that even though the distribution may be non-uniform in nm scale, overall Pt distribution is highly uniform.

3B.3.4. Characterization of Au/SBA-12

As described in chapter 2 section 2.5, our attempts to incorporate Au in SBA-15 by *in situ* method resulted in agglomeration and particles larger than the channel size. The reason for this could be hydrothermal treatment at 100°C. To test this hypothesis Au/SBA-12 was synthesized by giving the hydrothermal treatment to the gel at 40°C for 24 h. The material synthesized is characterized by XRD and TEM.

3B.3.4.1. Powder X-Ray Diffraction

Low angle shows that mesoporous order is well maintained even after the Au loading (Fig. 3B.18 I). Unit cell values for calcined Au/SBA-12 is 59 Å (d_{100}= 51.36 Å) which is 66.4 Å (d_{100}= 57.39Å) for as synthesized sample based on hexagonal lattice parameters ($a = \sqrt{4/3}\, d_{100}$). Wide angle XRD of calcined sample shows quite intense reflections at 2θ value 38.1, 44.38, 64.58 and 77.5 corresponding to (111), (200), (220) and (311) planes of Au (0) respectively (Fig.3B.18 II).

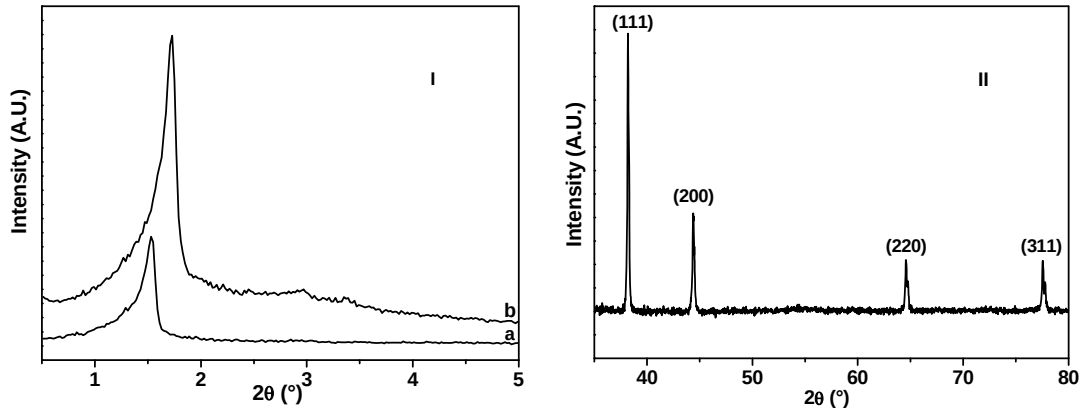

Fig. 3B.18. XRD patterns Au/SBA-12 materials; I) Low angle XRD where a) As synthesized, b) calcined, II) Wide angle XRD.

3B.3.4.2. Transmission Electron Microscopy

TEM studies were done to find out the distribution and size of Au nanoparticles in SBA-12. It showed very small particles of Au in the channels which are not clearly visible due to poor quality of silica matrix (Fig 3B.19). But some agglomerated particles were also seen outside the silica matrix.

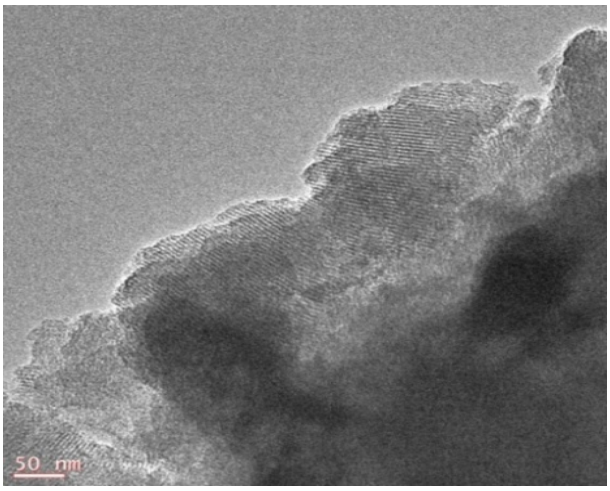

Fig. 3B.19. TEM Image of Au/SBA-12

3B.3.5. Characterization of FDU-12

Similar to P123 as described in chapter 2, this triblock copolymer i.e. F127 also forms stable mixed micellar system [19-21]. At 40^{o}C, F127 associates in to micelles with PPO forming hydrophobic core and PEO forming water swollen corona. When cationic surfactant CTAB is added to the copolymer system, its molecules get associated with copolymer micelle forming a large copolymer rich complex at low concentrations of CTAB. But increase in CTAB concentration leads to formation of smaller surfactant rich complexes with few molecules of copolymer along with the large copolymer rich complexes [19]. With further increase in CTAB concentration, it forms its own micelle leading to disruption of copolymer micelle in to single molecules randomly distributed in solution. So, to find out the optimum concentration of CTAB in F127 for a stable mixed micellar system to obtain ordered mesoporous FDU-12, we synthesized FDU -12 with different concentration of CTAB in 1 wt% F127. All the synthesized materials were characterized by XRD, N_2 adsorption and SEM.

3B.3.5.1. Powder X-Ray Diffraction

FDU-12 was synthesized with varying amounts of the surfactant CTAB in the polymer F127 and XRD studies of calcined FDU-12 materials were carried out to follow the effect on mesoporous order (Fig. 3B.20). It indicates a clear effect of the surfactant on the F127 micelle and hence the mesoporous structure. There is shift in

(111) reflections from 2θ value 0.77 in case of FDU-12 synthesised without CTAB to 0.99 in material synthesised with 32 mM CTAB.

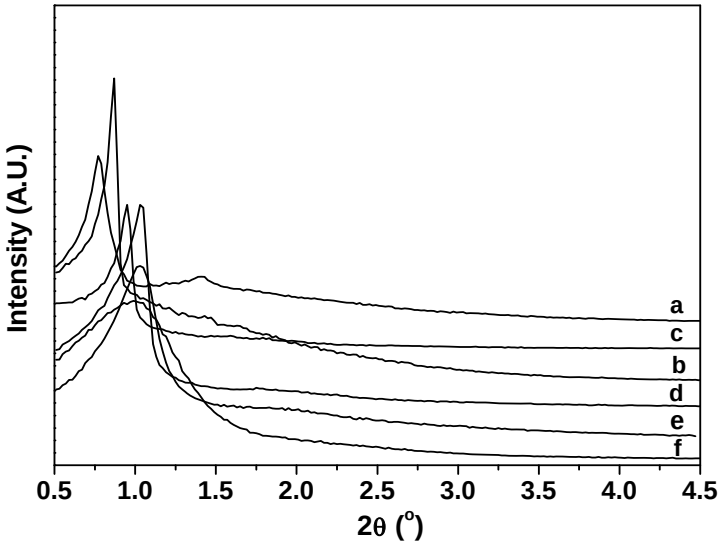

Fig. 3B.20. Low angle powder XRD pattern of FDU-12 samples synthesized with different concentrations of CTAB in 1 wt% F127; a) without CTAB, b) 2 mM CTAB, c) 4 mM CTAB, d) 8 mM CTAB, e) 16 mM CTAB and f) 32 mM CTAB.

Table 3B.6. Lattice parameters and unit cell values for FDU-12 materials synthesized with different concentrations of CTAB in 4 wt% Brij 76.

CTAB Concentration (mM)	2θ (°)	d_{100} (nm)	Unit Cell (nm)
-	0.77	11.5	19.8
2	0.86	10.3	17.8
4	0.94	9.4	16.2
8	1.03	8.57	14.8
16	1.03	8.57	14.8
32	0.99	8.92	15.4

Unit cell values were calculated from (111) reflection assuming it to be Fm3m cubic system (Table 3B.6). Thus, a decrease in unit cell value from 19.8 to 15.2 is observed. Although there is no change as we go from 4 mM to 8 mM, there is an obvious decrease in mesoporous order after 8 mM CTAB which is indicated by broadening of peaks.

3B.3.5.2. N_2 Adsorption Studies

N_2 adsorption studies were carried out to study the effect of surfactant concentration on the surface area, pore size and pore volume of the materials. It is clear from Fig. 3B.21 that all materials show type IV isotherms with H2 type hysteresis loop which is observed for 3D mesoporous materials with big cavities connected to each other by small windows [17, 22-24]. Various physiochemical characteristics measured by N_2 adsorption are given in Table 3B.7. The average pore sizes did not show any particular trend, which may be due to the 3D nature of the pores and the effect of CTAB on the self assembly of the template.

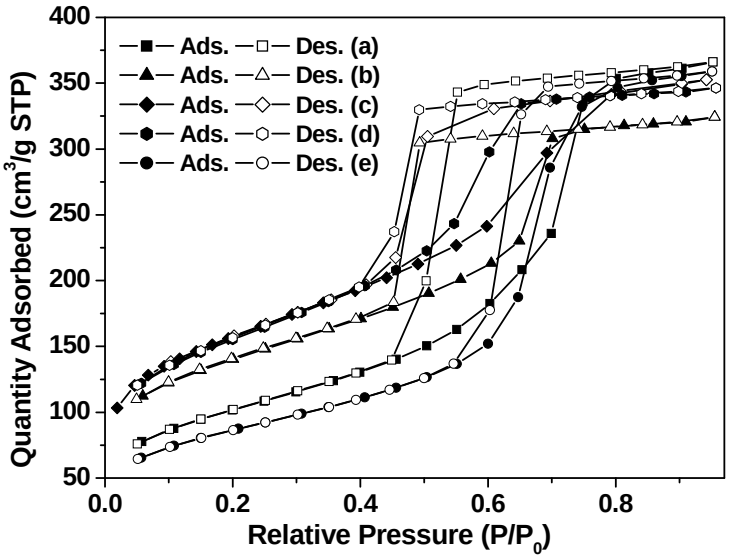

Fig. 3B.21. Adsorption isotherms of FDU-12 materials synthesized with different concentrations of CTAB in 1 wt% F127; a) without CTAB, b) with 4 mM CTAB, c) 8 mM CTAB, d) 16 mM CTAB, e) 32 mM CTAB (Here Ads. is adsorption and Des. is desorption branch of isotherm).

Table 3B.7. N_2 adsorption measurements of FDU-12 materials synthesized with different concentrations of CTAB in 1 wt% FDU-12.

CTAB concentration (mM)	Unit Cell (nm)	Pore Size (Å)	BET (m^2/g)	N_2 Uptake (cm^3/g STP)	Total Pore Volume (cm^3/g)	Micropore Volume (cm^3/g)
-	19.8	56.8	368	366	0.56	0.008
4	17.8	50.8	498	324	0.5	0.05
8	16.2	87	562	352	0.54	0.05
16	14.8	50.8	555	346	0.54	0.03
32	15.4	70	312	358	0.55	.009

3B.3.5.3. Scanning Electron Microscopy

Scanning electron microscopy studies were done to find out the morphology of the materials. FDU-12 materials synthesised without CTAB (Fig. 3B.22A) show polygonal particles with size varying from 5 to 10 μm for most of particles. Some particle with smaller size 0.5-5μm and bigger size varying from 10-15μm were also observed. The materials synthesized with 4 mM CTAB in 1 wt% F127 show similar morphologies but particle size lies in comparatively broader range of 5-15μm (Fig. 3.22B). Some spherical particles are also found in the FDU-12 synthesised with 16 mM CTAB (Fig. 3B.22C) along with polygonal particles. Particle size varies from 1-10μm. In the FDU-12 synthesised with highest concentration of CTAB i.e. 32 mM CTAB, no particular morphology is found and particle sizes varies in a broader range (Fig. 3B.22D). Most of the particles are of size greater than 10 μm.

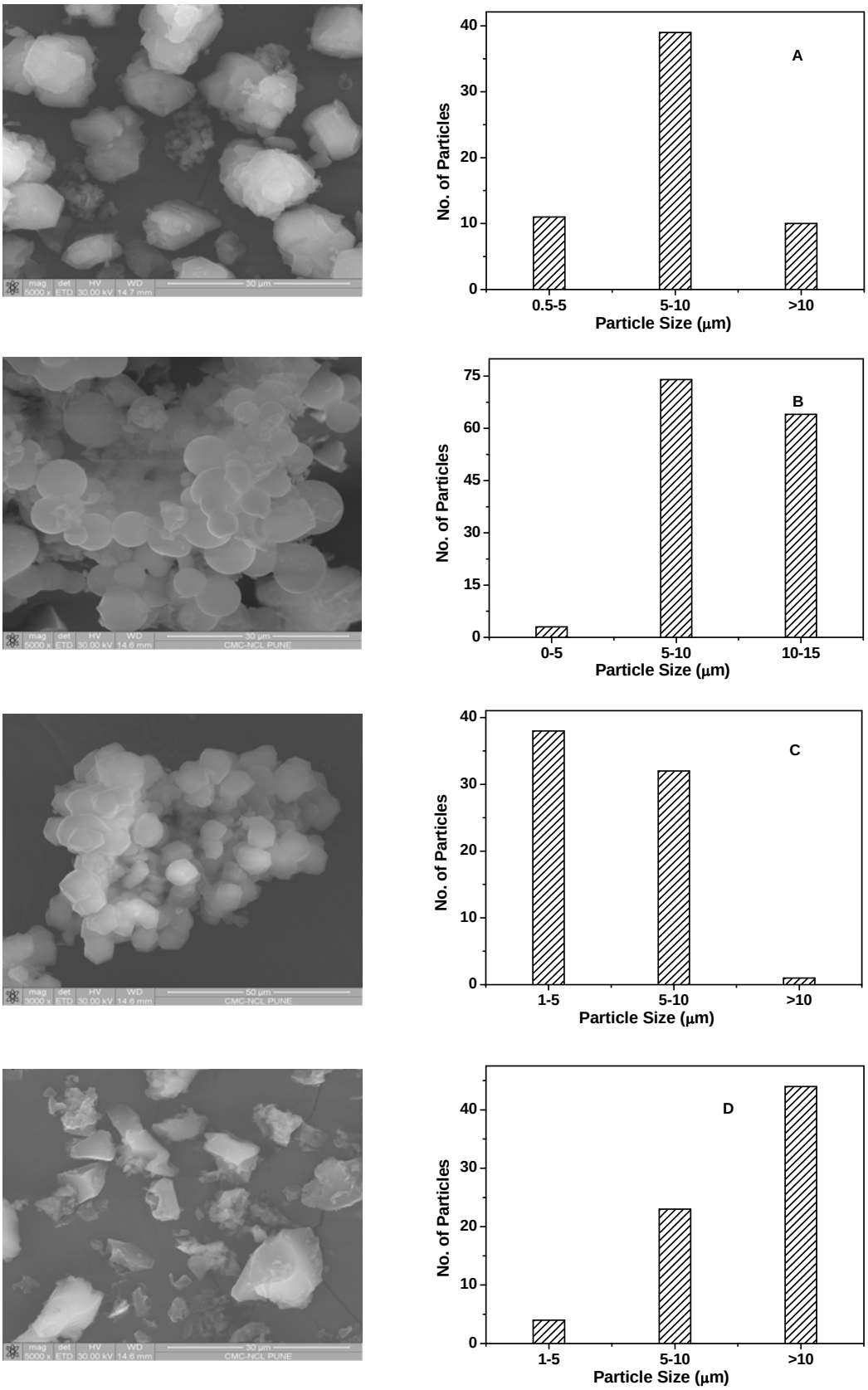

Fig. 3B.22. SEM images and particle size distribution of various FDU-12 materials synthesized with different concentration of CTAB in 1 wt% F127; A) w/o CTAB, B) 4 mM CTAB, C) 16 mM CTAB and D) 32 mM CTAB.

3B.3.6. Characterization of Pt/FDU-12

An optimum concentration of 2 mM CTAB in the final mixed micelle composite was chosen to incorporate platinum since higher concentration results in decrease in order of the final mesoporous material. Since we expected an electrostatic interaction of CTAB and $[PtCl_6]^{2-}$, the molar ratios of CTAB/H_2PtCl_6 was kept 2:1. Hence concentration of platinum was fixed at 1 mM which amounts to a Pt loading of 1-2 wt% in the final mesoporous compound. Pt/FDU-12 was characterized by XRD, N_2 adsorption, SEM and HRTEM and compared with FDU-12.

3B.3.6.1. Powder X-Ray Diffraction

Low angle XRD shows that mesoporous order is well maintained after the incorporation of Pt. There is shift in 2θ value of (111) reflection from 0.86 to 0.78 after the incorporation of Pt. Unit cell value for FDU-12 and Pt incorporated FDU-12 are 17.8 nm and 19.6 nm respectively. Wide angle XRD shows reflections at 2θ value 39.7 and 46.4 corresponding to (111) and (200) planes of Pt (0).

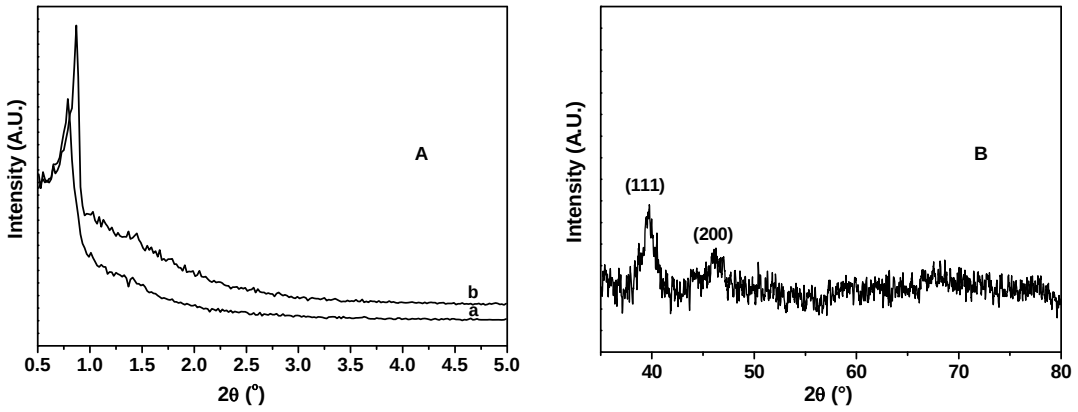

Fig. 3B.23. X-Ray diffraction pattern of FDU-12 materials; A) Low angle XRD of a) FDU-12 synthesised with 2 mM CTAB in F127 and b) Pt incorporated FDU-12; B) Wide angle XRD of Pt incorporated FDU-12.

3B.3.6.2. Transmission Electron Microscopy

TEM images clearly show the cubic nature of the material. Fig. 3B.24 shows TEM images recorded along the (110) (right) and (211) (left) planes [16]. It clearly shows the platinum particles in the cavities of the material. Pt loading was found to be 0.38% from ICP analysis.

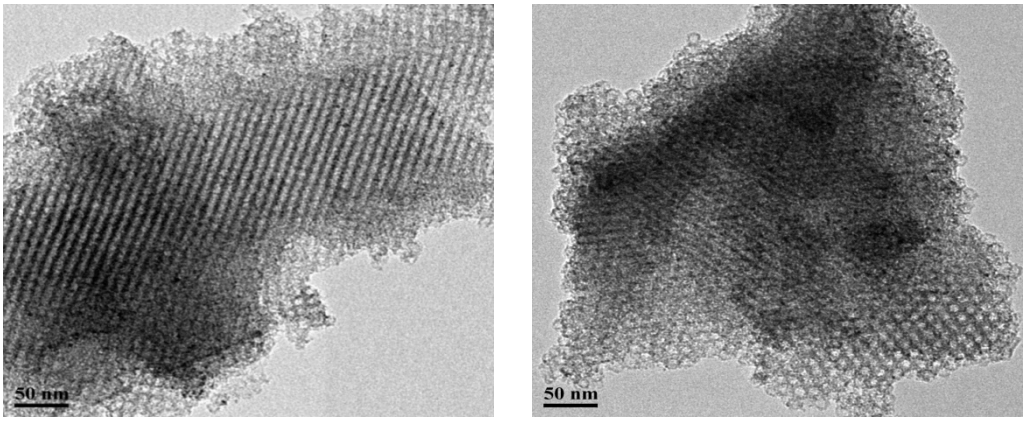

Fig. 3B.24. TEM image of platinum incorporated FDU-12.

3B.4. SUMMARY

In situ method which gives fine control over the morphology of platinum nanoparticles from spherical, rugby ball to nanorods morphology has been used to reduce the size of Pt nanoparticles by using the mesoporous SBA-12 with comparatively smaller channel size. SBA-12 has been synthesised with various concentration of CTAB in 4 wt% Brij 76 to find out the optimum concentration of CTAB to incorporate platinum. Platinum nanoparticle of size distribution of 4-5.5 nm could be synthesised in channels of mesoporous SBA-12. Since increase in CTAB concentration reduces the pore size of SBA-12, we also synthesised Pt/SBA-12 with various concentrations of CTAB to find out the effect of concentration of CTAB on Pt particle size. But this does not lead to further reduction in the size of Pt particles. We also studied the effect of increasing the loading on the size of Pt particles by synthesising Pt/SBA-12 by varying the conc. of Pt precursor in mixed micelle composite template. It results in the formation of some larger size particles outside the channels also. Effect of CTAB concentration on the retention of Pt has been studied by ICP analysis which shows that increase in CTAB concentration increases the % retention of platinum in the final material. Platinum has also been incorporated in to FDU-12, a three dimensional cubic mesoporous material. Effect of different concentration of CTAB on the mesoporous order of FDU-12 also has been studied by varying the concentration of CTAB in 1 wt% F127 during the synthesis. All synthesised materials i.e. SBA-12, Pt/SBA-12, FDU-12 and Pt/FDU-12 have been characterized by XRD, N_2 adsorption, SEM and TEM.

3B.5. REFERENCES

1. M. P. Pileni, *J. Phys. Chem.* **1993**, *97*, 6961.
2. A. Taleb, C. Petit, M. P. Pileni, *Chem. Mater.* **1997**, *9*, 950.
3. L. Motte, F. Billoudet, E. Lacaze, J. Douin, M. P. Pileni, *J. Phys. Chem. B* **1997**, *101*,138.
4. T. Teranishi, M. Miyake, *Chem. Mater.* **1998**, *10*, 594.
5. J. H. Fendler, F. C. Meldrum, *Ad*v. *Mater.* **1995**, *7*, 607.
6. N. Herron, Y. Wang, M. Eddy, G. D. Stucky, D. E. Cox, K. Moller, T. Bein, *J. Am. Chem. Soc.* **1989**, *111*, 530.
7. M. Brust, D. Walker, D. Bethell, D. J. Schiffrin, R. Whyman, *Chem. Commun.* **1994**, *801*.
8. C. B. Murray, D. J. Norris, M. G. Bawendi, *J. Am. Chem. Soc.* **1993**, *115*, 8706.
9. a) N. Toshima, Y. T. Yonezawa, *New J. Chem.* **1998**, *22*, 1179. b) N. Toshima, K. Hirakawa, *Polymer J.* **1999**, *31*, 1127.
10. B. Wiley, Y. Sun, B. Mayers, Y. Xia, *Chem.-- Eur. J.* **2005**, *11,* 454.
11. Y. Sun, Y. Xia, *Science* **2002**, *298*, 2176.
12. A. K. Prashar, R. P. Hodgkins, R. Kumar, R. N. Devi, *J. Mater. Chem.* **2008**, *18*, 1765.
13. D. Y. Zhao, Q. Huo, J. Feng, B. F. Chmelka, G. D. Stucky, *J. Am. Chem. Soc.* **1998**, *120*, 6020.
14. Y. Sakamoto, I. Dı´az, O. Terasaki, D. Zhao, J. P. Pariente, J. M. Kim, G. D. Stucky, *J. Phys. Chem. B* **2002**, *106*, 3118.
15. J. Fan, C. Yu, F. Gao, J. Lei, B. Tian, L. Wang, Q. Luo, B. Tu, W. Zhou, D. Zhao, *Angew. Chem., Int. Ed.* **2003**, *42,* 3146.
16. T. Yu, H. Zhang, X. Yan, Z. Chen, X. Zou, P. Oleynikov, D. Zhao, *J. Phys. Chem. B* **2006**, *110*, 21467.
17. P. Nilsson, B. Lindman, *J. Phys. Chem.***1984**, *88*, 539.
18. H. Gao, S. Zhao, S. Z. Mao, H. Yuan, J. Yu, L. Shen, Y. Du, *J. Colloid*

Interface Sci. **2002**, *249*, 200.

19. J. Jansson, K. Schille´n, M. Nilsson, O. Solderman, G. Fritz, A. Bergmann, O. Glatter, *J. Phys. Chem. B* **2005**, *109*, 7073.

20. E. Hecht, K. Mortensen, M. Gradzielski, H. Hoffmann, *J. Phys. Chem.* **1995**, *99*, 4866.

22. K. Morishige, *Adsorption* **2008**, *14*, 157.

23. K. S.W. Sing, *Colloids and Surface* **1989**, *38*, 113.

24. M. D. Donohue, G. L. Aranovich, *J. Colloid Interface Sci.* **1998**, *205*, 121.

CHAPTER 4

CO OXIDATION AND CINNAMALDEHYDE HYDROGENATION: PARTICLE SIZE EFFECT STUDY ON ACTIVITY AND SELECTIVITY

4.1. INTRODUCTION

Catalysis by nanoparticles has long been in focus due to its unique significance and considerable contributions to industry. A fundamental understanding of reactions on the nanoparticle surfaces has always been challenging, sparking interest in basic studies to throw light upon these systems. The employment of such catalysts span decades from earliest examples of Pt/Al_2O_3 in petroleum reforming to precious metals like Rh, Pt and Pd in three way catalyst for treatment of automobile exhaust which is developed recently. Since active centers in metal nanoparticles are present on the surface and the surface features of the metal nanoparticles change with shape and size, activity and selectivity can be tuned by controlling these parameters. The particle size and shape play a very important role [1-4]. The trend of catalytic activity with varying particle size and shape is because of the various molecular scale factors which include change in surface structure, electronic state, metal-support interaction and oxidation states. Particle size effect is more prominent in the range of 1-10 nm.

In the present chapter, we discuss two important reactions viz CO oxidation and cinnamaldehyde hydrogenation using Pt/SBA type materials containing Pt nanoparticles with narrow size distribution as catalysts. We have synthesized Pt nanoparticles of average size 8 nm in SBA-15 and 4-5.5 nm in the SBA-12 using the *in situ* method as described in chapter 2 and 3 respectively [5]. Since we wanted to study the effect of platinum particle size, we also synthesized the Pt metal nanoparticles of average sizes 1.8 nm and 3.6 nm in the channels of mesoporous SBA-15 by using a method reported in literature [6]. We studied the effect of particle size on the activation energies of CO oxidation using these materials. Hydrogenation of α, β-unsaturated compounds and selectivity to various products is known to be sensitive to particle size variation. Hence we have studied the hydrogenation of cinnamaldehyde over these materials to understand the effect of particle size on the selectivity.

4.1.1. CO Oxidation

CO oxidation is a benchmark reaction in heterogeneous catalysis because of its practical and fundamental importance [7-10]. It has practical utility in many industrial processes, including reduction of CO in automobile exhaust gases and

selective oxidation of fuel streams for polymer electrolyte membrane fuel cells. It is also interesting from the point of view of basic understanding, since it involves most of the fundamental steps of heterogeneous catalysis. It involves molecular adsorption/desorption of reactant ($CO \leftrightarrow CO_{ads}$), dissociative adsorption of a reactant ($O_2 \rightarrow 2O_{ads}$), surface reaction ($CO_{ads} + O_{ads} \rightarrow CO_2$), and reaction inhibition/surface poisoning (oxide formation). Seemingly simple, this reaction comprises of a complexity due to the multiple steps involved.

CO molecules adsorb on metal with carbon atom directed towards the surface and can coordinate with metal atoms with various geometries. Blyholder model is used to explain the CO bonding to the metal surface [11]. In this model the bonding occurs through a concerted electron transfer from the highest filled (5σ) molecular orbital of CO to unoccupied metal orbitals (essentially d orbital), with back-donation occurring from occupied metal orbitals to the lowest unfilled (2π) orbital of CO (Fig. 4.1). The strength of the CO-metal bond might be expected to depend upon: 1) the nature of the adsorbent metal, 2) the crystallographic orientation of the surface and 3) the geometric location of the adsorbed molecule on a given single crystal plane [12-14].

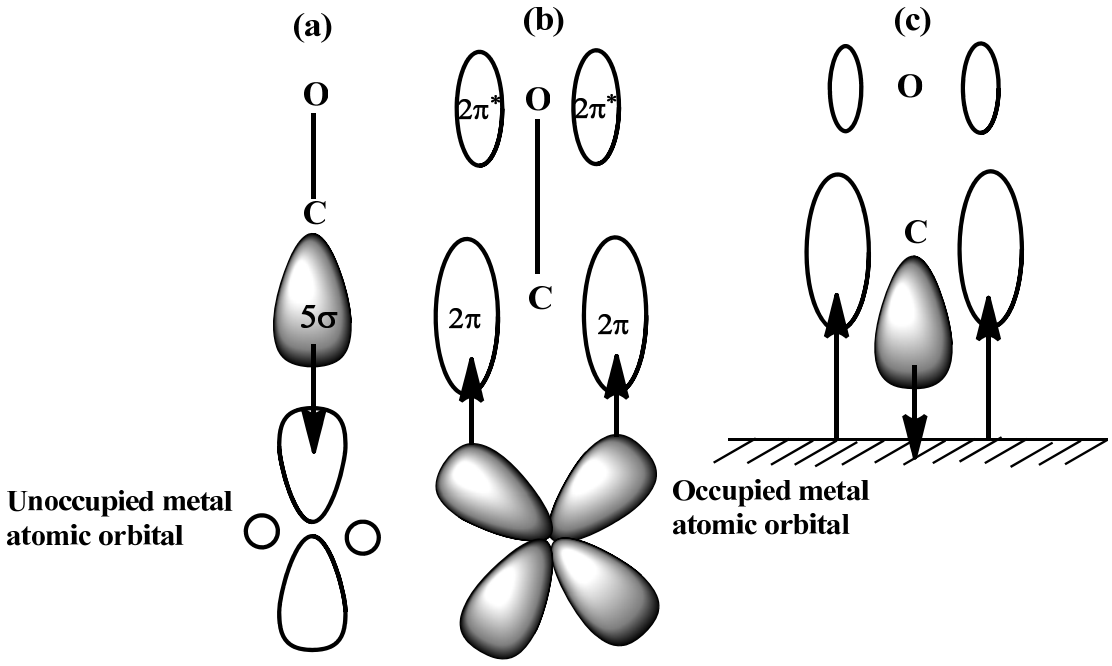

Fig. 4.1. A schematic diagram of a synergic bonding of CO to metal.

There are various mechanisms proposed for the CO oxidation on metal surfaces. Among these three most popular ones are 1) Langmuir-Hinshelwood mechanism, 2) Eley Rideal mechanism and 3) Mas van Krevelen mechanism.

Langmuir-Hinshelwood mechanism is the most widely accepted mechanism for the CO oxidation over platinum group metals [15-18]. It involves various steps 1) adsorption of reactant molecules to the metal surface, 2) dissociation of molecules on the surface, 3) reaction between the adsorbed molecules and 4) desorption of the reaction products (molecules) to the gaseous phase (Fig. 4.2).

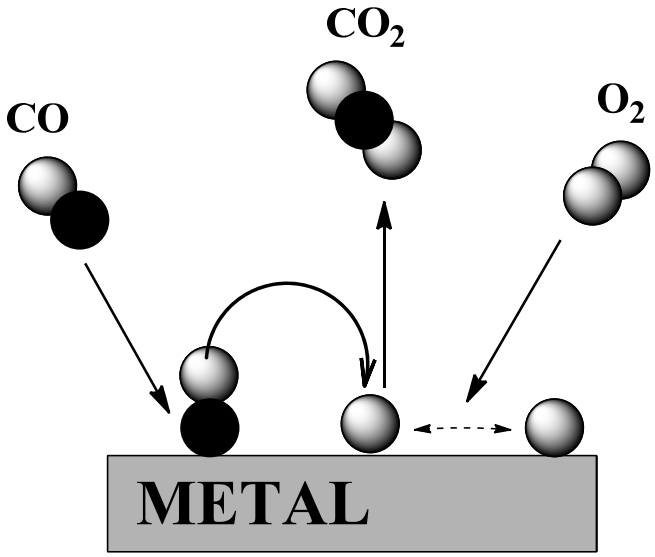

Fig. 4.2. Schematic representation of L-H mechanism for CO oxidation.

In the Eley Riedal mechanism (Fig. 4.3) oxygen molecules get adsorbed on metal surface and gaseous CO molecule strikes with the dissociated oxygen atom and escapes as CO_2 molecule in gaseous state [19, 20].

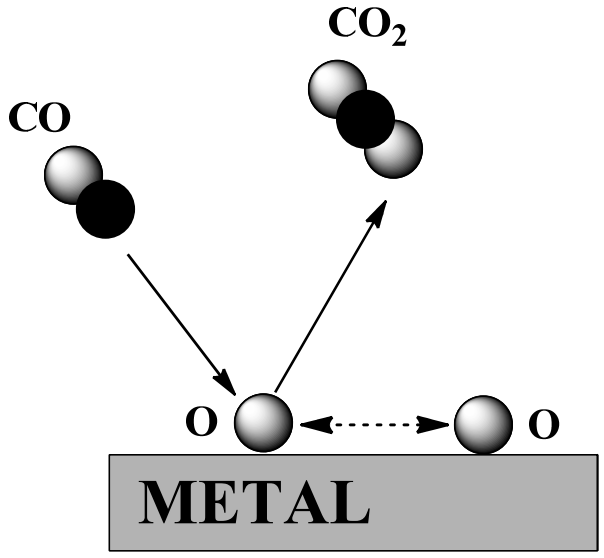

Fig. 4.3. Schematic representation of E-R mechanism for CO oxidation.

Mars Van Krevelen mechanism proposes that catalyst participate more actively in the reaction, playing the role of intermediate rather than merely a substrate [21, 22]. In an oxygen rich environment i.e. at high pressures of O_2 and at elevated temperature, the metal will oxidise. Depending upon the detailed energetic of the metal and oxide, either a thin film forms, as has been found for Pt(110) or oxidation slowly proceeds further in to metal, as seems to be the case of Pd(110) [23, 24]. CO molecule gets adsorbed on the oxide and forms CO_2 which diffuses in to atmosphere. The resulting oxygen vacancies are filled by the oxygen from the gas.

In CO oxidation studies related to particle size effect, diverse trends have been observed from different types of metals. For example, Au nanoparticles when supported on semiconducting oxide supports exhibits a marked increase in catalytic activity below 5 nm [25]. A similar trend was observed over colloidally synthesized Rh nanoparticles in the range of 5-11 nm [26]. Lennon et al [27] has done extensive studies for the oxidation of CO by O_2 over five noble metals (Ru, Rh, Pd, Ir, and Pt) supported on silica and found the activation energies, kinetic orders, and relative activities. These results were compared with the predictions of a model which used parameters derived from measurements made under UHV conditions and/or with only one reactant present in gas phase. McCarthy et al [28] studied the variation in specific activity of CO oxidation over Pt/Al_2O_3 as a function of crystallite size. They studied three different crystallite sizes of Pt (2.8, 7.8 and 10 nm) supported over alumina prepared by sintering at higher temperatures. The rate of CO oxidation was also studied as function of CO partial pressure and temperature. Their studies reveal that at low CO concentrations the oxidation rate is directly proportional while at high CO levels it is inversely proportional. The specific rate has been found to be higher for larger Pt particles in low CO partial pressure range while it becomes structure insensitive to particle size at high CO partial pressures. The reason has been assigned to the strong binding of O to the smaller particles which makes its extraction by CO difficult but in case of bigger particles O extraction is increased which results in increased specific rate.

The studies of particle size effects in most cases have been carried out using catalysts prepared by traditional methods such as impregnation and ion exchange which give very broad distribution of particle size. A lot of mechanistic studies of this reaction have been done at high vacuum at low pressures since first investigation by

Langmuir [15]. Not much is clear about the mechanism of this reaction at high pressures (atm. pressure) where this reaction has actual importance.

4.1.2. Cinnamaldehyde Hydrogenation

Selective catalytic hydrogenation of organic substrates containing a number of unsaturated functional groups is an important step in industrial preparation of fine chemicals and has been attracting much interest for fundamental research in catalysis. Especially, the selective hydrogenation of α, β-unsaturated carbonyls like cinnamaldehyde, which is a key step in the manufacture of pharmaceuticals [29] and flavours and fragrances [30, 31]. The chemoselective hydrogenation of a carbonyl bond in multi-unsaturated aldehydes and ketones (scheme 1.1) is a difficult task since thermodynamics favours C=C hydrogenation over C=O by ca. 35 kJ/mol [32] so it has been focus of much research.

Although, selective reduction can be achieved using stoichiometric amounts of reducing agents such as metal hydrides [33], these methods are useful only for small scale production because they involve costly chemicals. So the application of heterogeneous catalysts will be advantageous in this case. Moreover, the heterogeneous catalysts are environmentally more friendly and easier to separate and reuse than their homogeneous counterparts. Various supported noble metal catalysts are being extensively studied as potential heterogeneous catalyst for this purpose. It was found that adsorption energies of C=C and C=O bonds on various crystal planes of metal particles are different and this can be exploited for improving the selectivity of the catalyst [34, 35]. Since nature of planes exposed changes with change in particle size so the selectivity of various products will vary with particle size.

4.2. SYNTHESIS

Pt/SBA-15 with average size 8 nm and Pt/SBA-12 with particle sizes of 4.4 and 4.9 nm were synthesised using *in situ* method as described in Chapter 2 section 2.2.2 and 3 section 3B.2.2 respectively. Pt/SBA-15 materials with Pt particle size 1.8 nm and 3.6 nm were synthesized by known method as described in ref. [6].

4.2.1. Synthesis of Pt/SBA-15 using Pre-synthesized Pt nanoparticles

Pt particles with the size of 1.8 nm and 3.6 nm were produced by alcohol reduction method. A polymer PVP, was used to stabilize the particles by capping

them in aqueous solution. These synthesised nanoparticles were incorporated in the channels of mesoporous SBA-15 silica using low power sonication.

4.2.1.1. Pt Nanoparticles Synthesis

Pt particles of average size between 1.8 and 3.6 nm were synthesized according to procedure described in literature [6].

1.8 nm particles: To 12.5 mL of 0.48 mM $H_2PtCl_6.6H_2O$ in ethylene glycol, 12.5 mL of 0.5 M NaOH in ethylene glycol was added. The mixture was heated at 433K for 3h accompanied by N_2 bubbling. A 6 mL aliquot of the resulting solution was transferred to a vial. The particles were precipitated by adding 1 mL of 2 M HCl, and dispersed in 180 mL of ethanol containing 12.2 mg of PVP (Mw=29000). The solvent was evaporated and residue was redispersed by adding appropriate amount of water so that final concentration of Pt sol is $3x10^{-3}$ M.

3.6 nm Pt particles: PVP (133 mg) was dissolved in a mixture of 20 mL of 6 mM $H_2PtCl_6.6H_2O$ aqueous solution and 180 mL of ethanol. The mixture was refluxed for 3h. The solvent was evaporated and residue was redispersed in a water/methanol (1:9) mixture. 100 mL of this solution was mixed with 10 mL of 6 mM $H_2PtCl_6.6H_2O$ solution and 90 mL of methanol. The mixture was refluxed for 3 h. The solvent was evaporated and residue was redispersed by adding appropriate amount of water so that final concentration of Pt sol is $3x10^{-3}$ M.

4.2.1.2. Synthesis of Mesoporous SBA-15 silica

Silica SBA-15 was prepared according to the method reported in literature [36]. Pluronic P123 (6 g) was dissolved in 45 g of water and 180 g of 2 M HCl solution with stirring at 313 K for 30 min. TEOS (12.75 g) was added to the solution with stirring at 313 K for 24 h. The mixture was aged at 373 K for 48 h. The white powder was recovered through filtration, washed with water and ethanol thoroughly, and dried in air. The material was calcined at 823 K for 12 h.

4.2.1.3. Preparation of Pt/SBA-15

Pt colloid aqueous solution (25.6 mL, $3x10^{-3}$ M) was mixed with 74.4 mL of water and 100 mL of ethanol. The mixture was quickly added to 1.5 g of SBA-15, and slurry was sonicated for 3 h at room temperature by a commercial ultrasonic cleaner. Brown precipitates were separated by centrifugation, thoroughly washed with water

and ethanol and dried in an oven at 373 K. Pt/SBA-15(1.8 nm) was calcined at 623 K for 12 h and Pt/SBA-15(3.6 nm) was calcined at 723 K for 12 h with O_2 flow.

4.2.2. Synthesis of Pt/SBA-12 (4-5.5 nm)

Pt/SBA-12 materials were synthesised using metal precursor mixed micelle composite with CTAB/Pt ratio 2:1 and 32:1.32 in 4 wt% Brij 76. Synthesis procedure is same as described in Chapter 3 B section 3B.2.2.

4.2.3. Synthesis of Pt/SBA-15 (8 nm)

Pt/SBA-15 was synthesised using metal precursor mixed micelle composite with CTAB/Pt ratio 2:1 in 1wt% P123. Synthesis procedure is same as described in Chapter 2 section 2.2.2.

4.3. CHARACTERIZATION OF CATALYSTS

All the materials used for catalysis were characterised by ICP, X-Ray diffraction and HRTEM.

4.3.1. ICP-OES and Powder X-Ray Diffraction

All the samples were analysed by ICP. Sample Pt/SBA-15(1.8 nm), Pt/SBA-15(3.6 nm), Pt/SBA-12(4.4 nm), Pt/SBA-12(4.9 nm) and Pt/SBA-15(8 nm) contains 0.96 wt%, 1 wt%, 0.42 wt%, 0.72% and 0.68 wt% Pt respectively. Low angle XRD shows the presence of mesoporous order in the materials (Fig. 4.4). Scanning at high angles show reflections at 2θ value 39.7, 46.2, and 67.5 corresponding to (111), (200) and (220) planes indicative of Pt (0) (Fig. 4.5).

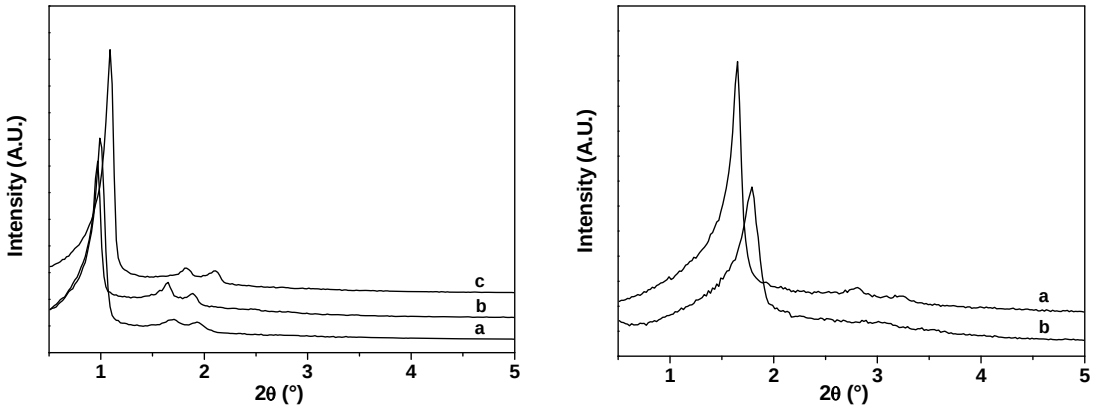

Fig. 4.4. Low angle XRD of various samples; left a) Pt/SBA-15(1.8 nm), b) Pt/SBA-15(3.6 nm), c) Pt/SBA-15(8 nm); right a) Pt/SBA-12(4.4 nm), b) Pt/SBA-12(4.9 nm).

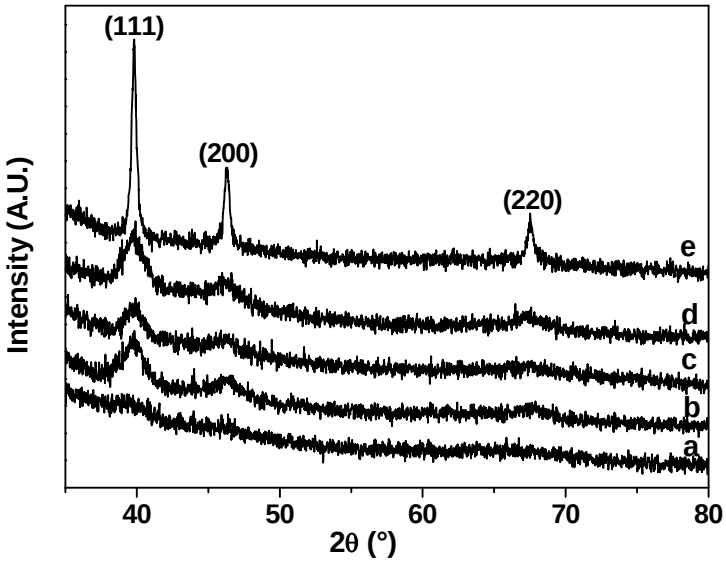

Fig. 4.5. Wide angle XRD of various samples; a) Pt/SBA-15(1.8 nm), b) Pt/SBA-15(3.6 nm), c) Pt/SBA-12(4.4 nm), d) Pt/SBA-12(4.9 nm), e) Pt/SBA-15(8 nm).

4.3.2. Transmission Electron Microscopy

TEM studies were done to find out the particle size distribution and also hexagonal ordering of mesoporous silica of all the Pt containing samples. In Pt/SBA-15(1.8 nm), which we synthesised by following the procedure as described in section 4.2.1, Pt particles with size slightly different from that reported in literature (1.7 nm) were obtained. In this sample, most of the particles i.e. almost 79% are from 1.7-2.2 nm, while some particles of 2.5 nm (6%) and 3.3 nm (15%) are also observed (Fig. 4.6). Average size of Pt nanoparticles was found to be 1.8 nm.

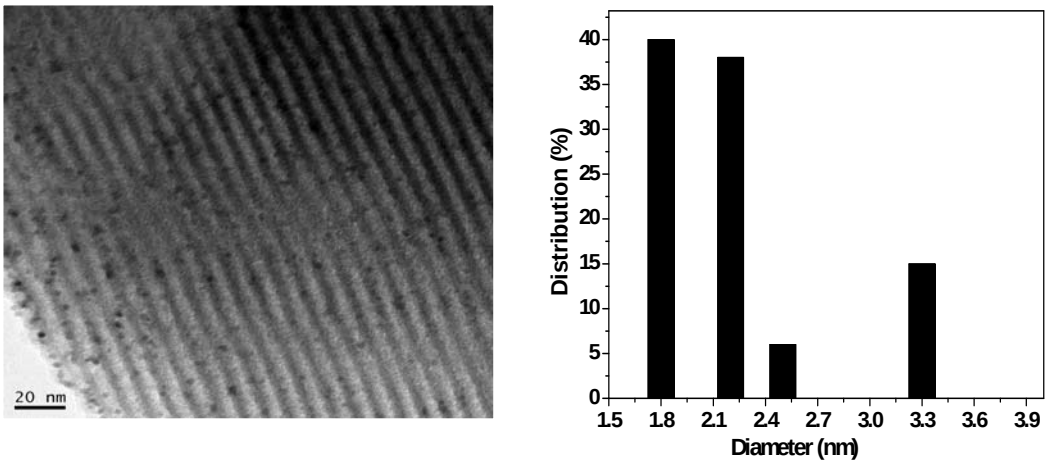

Fig. 4.6. TEM image and particle size distribution of Pt/SBA-15(1.8 nm).

In SA2, we got Pt particles mostly (78%) of size varying from 2.8-3.8 nm (Fig. 4.7). Although, Pt particles of bigger size i.e. more than 3.8 nm were also observed, average size was found to be 3.6 nm.

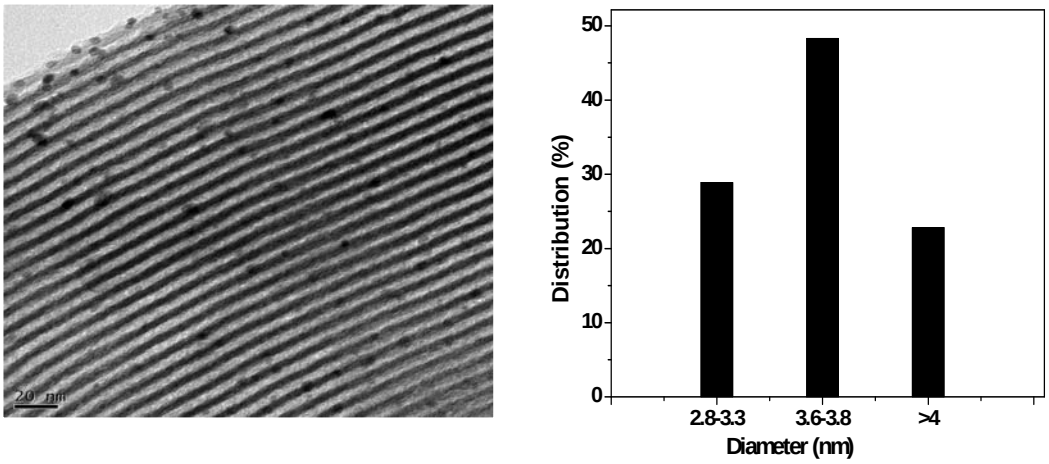

Fig. 4.7. TEM image and particle size distribution of Pt/SBA-15(3.6 nm).

TEM images and particle size distribution of Pt/SBA-12 samples are described in chapter 3B, section 3B.3.3.4 (Fig. 3B.12 & 3B.15). Pt/SBA-15 with bigger particle sizes was synthesised by *in situ* method. It contains Pt particles of average size 8 nm but Pt particle with size greater than 9 nm were also observed (Fig. 2.12).

4. 4. EXPERIMENTAL SET UP AND REACTION CONDITIONS

4.4.1. CO Oxidation

4.4.1.1. Reactor Set Up

Catalytic runs were carried out in a fixed bed down flow glass reactor at atmospheric pressure. The schematic diagram of the experimental set up is presented in Fig. 4.8 and a photograph of the actual set up is presented in Fig. 4.9. The reactor is made up of glass with inner diameter of 14 mm and is placed in a tubular furnace. The furnace temperature was controlled using Radix 6400 temperature controller and the catalyst bed temperature was measured by using K-type thermocouple. Before reaction the catalyst was pretreated in a flow of hydrogen. The reactant gases (Ultra high purity (UHP) CO and O_2) and the diluent (UHP N_2) were connected to the reactor through mass flow controllers (MFCs) for controlling the flow rates and the concentrations. The gases were pre-mixed in a 0.635 cm o.d. stainless tubing, before entering the reactor. The reactants concentrations and feed flow rates were varied by appropriate selection of the individual gas flow using MFCs. The products from the

reactor were analyzed by an on-line gas chromatograph (GC, M/s Nucon Ltd.) having molecular sieve 13X column (length: 91.4 cm) and thermal conductivity detector (TCD).

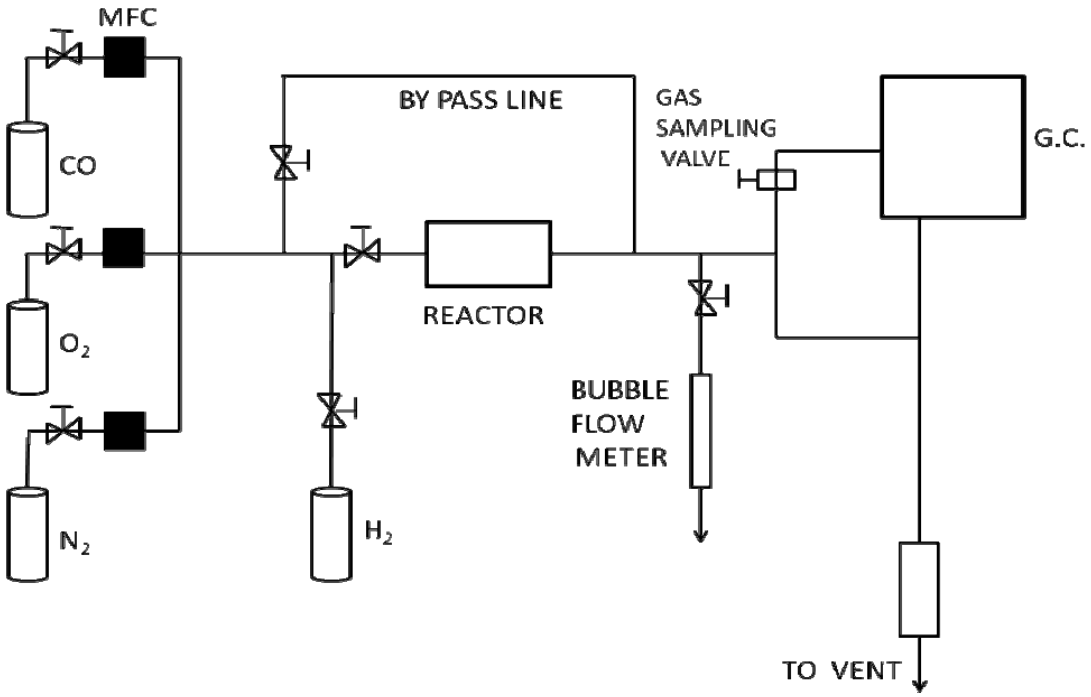

Fig. 4.8. Flow diagram of the reaction set up.

Fig. 4.9. Reaction set up and gas chromatogram.

4.4.1.2. Reaction Conditions

All the catalytic reactions were done in the temperature range of 433-571 K at atmospheric pressure. Reactant gas mixture consisted of 9.5±0.5% (v/v) CO, 6.1±0.4% (v/v) O_2 and 84.3±1.3% (v/v) N_2. Five different total flow rates i.e. 21.2±1.2, 40.3±0.8, 60.5±1.5, 80.08±1.4 and 99.7±0.7 cm^3/min of reactant gas mixture which corresponded to GHSV values of 3180(±180), 6045(±120), 9075(±225), 12012(±210) and 14955(±105) $cm^3\ h^{-1}\ g_{cat}^{-1}$ respectively were used for each catalyst. Four different catalysts i.e. Pt/SBA-15(1.8 nm), Pt/SBA-15(3.6 nm), Pt/SBA-12(4.4 nm) and Pt/SBA-15(8 nm) were studied. Catalysts Pt/SBA-15(1.8 nm) and Pt/SBA-15(3.6 nm) consist of Pt nanoparticles of average size 1.8 and 3.6 nm respectively in the channels of SBA-15. Catalyst Pt/SBA-12(4.4 nm) consists of Pt particles of average size 4.4 nm in SBA-12. This catalyst was synthesised using *in situ* method described in chapter 3 section 3B.2.1.2. Catalyst Pt/SBA-15(8 nm) consist of Pt nanoparticles of 8 nm average size, prepared by using *in situ* method as described in chapter 2 section 2.2.2. Although, originally all the catalysts contained different loadings of Pt for the sake of comparison Pt loading in each reactor charge was adjusted to the same value (0.4 wt%) by diluting the catalyst with calcined SBA-15. 0.4 g of catalyst was taken for the experiments. It was pelletized and sieved through 0.5 mm sieves before loading in the reactor. Prior to reaction, each catalyst was activated/reduced at 673 K for 2 h with 2 K/min ramp rate under H_2 flow. Then temperature was lowered to 373 K and kept at that temperature for 1 h under N_2 flow (10 cm^3/min). Subsequently the bed temperature was raised to 433 K and tested for its activity at this temperature. The bed temperature was increased in 10 K increments until the temperature of light off was reached and the steady state activity (outlet CO concentration) at each temperature was noted. For each reaction temperature, the reaction mixture was analyzed after 30 min on stream to allow the attainment of steady state conditions. The conversion of CO was calculated from change in CO concentration in the inlet and outlet gases. Each catalyst was tested at all the five flow rates without removing the catalyst from the reactor.

4.4.2.. Cinnamaldehyde Hydrogenation

Reaction was studied for four different Pt/SBA materials i.e. Pt/SBA-15(1.8 nm), Pt/SBA-15(3.6 nm), Pt/SBA-12(4.9 nm) and Pt/SBA-15(8 nm) with Pt average particle size 1.8, 3.6, 4.9 and 8 nm respectively. Since Pt loading in each material was

different, so for each catalyst, different amount was taken for reaction but reactant/catalyst (Pt) molar ratio was kept constant. A 100 mL Parr autoclave equipped with a pressure gauge, stirrer and thermocouple was used as the reaction vessel. Catalyst was pre-activated at 100°C for two hours in 35mL isopropanol under 34 bar pressure (RT) before the reaction. 1.25 g of cinnamaldehyde in 40 mL of isopropanol was charged in the reactor and heated to 60°C under a H_2 pressure of 30 bars at RT. At intervals, aliquots of the reaction mixture were taken from the reactor and GC analysis performed on Agilent Technologies 6890N Network GC system using a HP5 column.

4.5. CATALYTIC STUDY OF CO OXIDATION

A comparative study of the behaviour of the catalysts (Pt/SBA-15(1.8 nm), Pt/SBA-15(3.6 nm), Pt/SBA-12(4.4 nm) and Pt/SBA-15(8 nm)) at different GHSVs (3180±180-14955±105) $cm^3\ h^{-1}\ g_{cat}^{-1}$) and temperatures are presented in this section. As expected, the conversion increased with increase in temperature for all the catalysts. The increase in conversion was initially gradual up to a certain value (light off temperature) beyond which the conversion increased rapidly to 100%, with the further increase in temperature. The temperature at light off (T_{lo}) and 100% conversion (T_{100}) was found to be dependent on the GHSV. Both were lower at lower GHSV as the contact time of the gas with the catalyst bed was longer at low GHSVs.

4.5.1. Effect of Temperature and GHSV on the Catalyst Activity

The conversion increased with increase in temperature for all the four catalysts at all GHSVs (Fig. 4.10). T_{100} and conversion at T_{lo} were dependent on GHSV for all the catalysts. T_{lo} and T_{100} were lower at low GHSV and increased with increase in GHSV. Lower GHSVs lead to higher contact times and higher conversions. As CO oxidation is exothermic, the heat liberated during the reaction is used up in activating higher fractions of reactant molecules. At higher GHSVs, the contact times are lower, the conversions are lower; consequently the exothermic heat generated is lower leading to higher T_{lo} and higher temperatures at 100% conversions. For the same GHSV, the T_{lo} and T_{100} were also dependent on the type of catalyst. It was lowest for Pt/SBA-15(1.8 nm) and highest for Pt/SBA-15(8 nm) and followed the order: 8 nm > 4.4 nm > 3.6 nm > 1.8 nm.

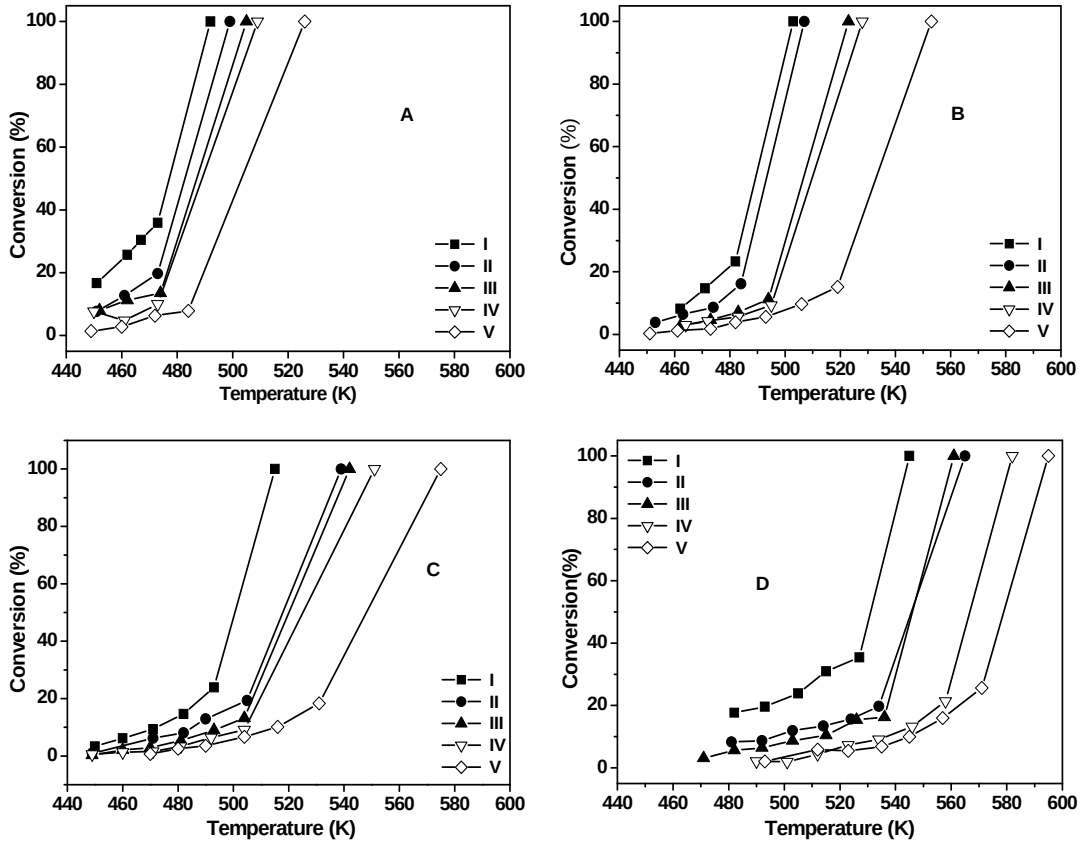

Fig. 4.10. Temperature vs. conversion graphs for various catalysts at various flow rates (I: 3180±180 $cm^3 h^{-1} g_{cat}^{-1}$, II: 6045±120 $cm^3 h^{-1} g_{cat}^{-1}$, III: 9075±225 $cm^3 h^{-1} g_{cat}^{-1}$, IV: 12012±210 $cm^3 h^{-1} g_{cat}^{-1}$, V: 14955±105 $cm^3 h^{-1} g_{cat}^{-1}$; A: Pt/SBA-15(1.8 nm), B: Pt/SBA-15(3.6 nm), C: Pt/SBA-12(4.4 nm), D: Pt/SBA-15(8 nm)).

4.5.2. Effect of Pt Particle Size on the Activity

A comparison of different catalysts for their activity at different GHSVs is presented in Fig. 4.11 (A-E). It is clear from the graphs that catalysts with smaller particle size are active at comparatively lower temperature and this activation temperature increases with increase in particle size. T_{lo} and T_{100} varies with catalyst particle size at all GHSVs. The conversion at light off temperature does not vary much with particle size < 4.4 nm. However T_{lo} is very much dependent on the particle size. Activation energy [37-39] of the reaction for all the catalysts were calculated by differential and integral analysis based on first principles.

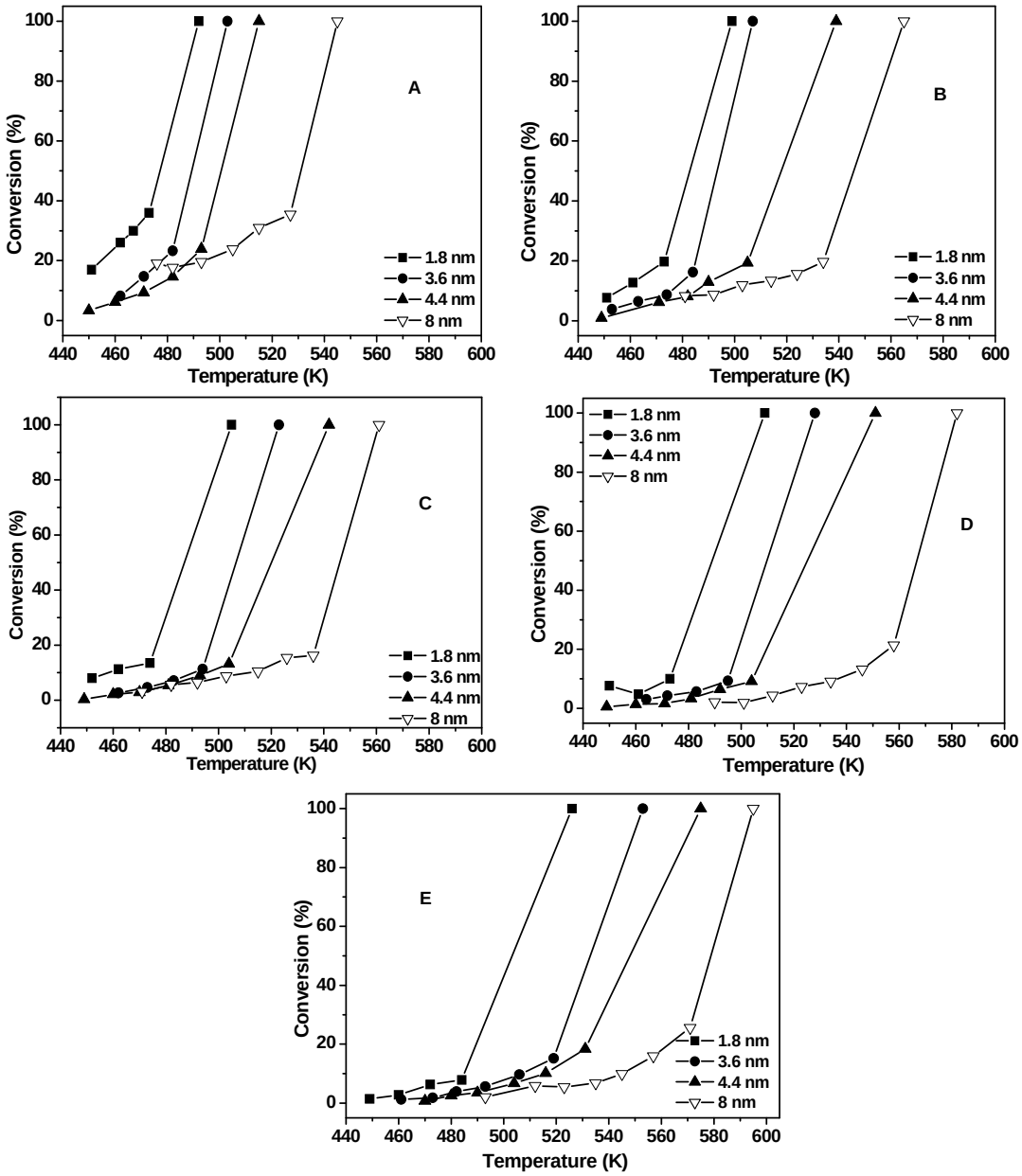

Fig. 4.11. Comparision of various catalysts with different particle sizes at various GHSVs (A=3180±180 ml $h^{-1}g_{cat}^{-1}$, B=6045±120 ml $h^{-1}g_{cat}^{-1}$, C= 9075±225 ml $h^{-1}g_{cat}^{-1}$, D=12012±210 ml $h^{-1}g_{cat}^{-1}$, and E=14955±105 ml $h^{-1}g_{cat}^{-1}$).

4.5.2.1. Activation Energy by Integral Analysis

In this method, rate constant at different temperatures is calculated from the slopes of graphs between conversion and contact time (based on catalyst volume and flow rate) according to equn. (9) (Appendix-1). From the rate constants activation energy is calculated according to equation (11) (appendix-1) (Fig. 4.12). Activation energy of Pt/SBA-15(1.8 nm), Pt/SBA-15(3.6 nm), Pt/SBA-12(4.4 nm) and Pt/SBA-15(8 nm) are found to be 31.5, 36.85, 39.7 and 35.5 Kcal/mole respectively.

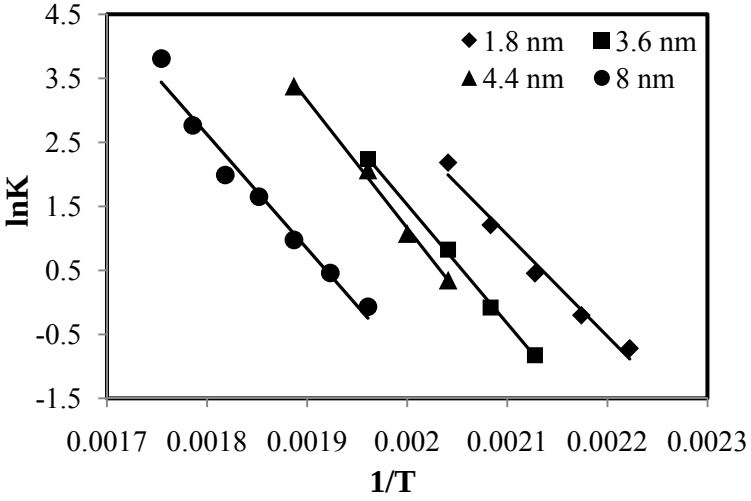

Fig. 4.12. lnK vs. 1/T graphs for different catalysts (Ea= -slope x R).

4.5.2.2. Activation Energy by Differential Analysis

The activation energy for each contact time was calculated from the slope of the plot of LHS of eqn. 14 (Appendix-1) vs. 1/T for each GHSV (contact time) for each catalyst and is presented as Fig. 4.13. As expected the slope of the graph did not vary much for each catalyst for different GHSVs. The activation energy of each catalyst was taken as the average of the activation energy obtained at different GHSVs. The average activation energy for Pt/SBA-15(1.8 nm), Pt/SBA-15(3.6 nm), Pt/SBA-12(4.4 nm) and Pt/SBA-15(8 nm) were 30.97, 37.9, 37.3 and 35.9 Kcal/mole respectively. Activation energy calculated by the two methods is compared in Table 4.1. There is good agreement between the values calculated by both methods indicating that there are no mass transfer limitations.

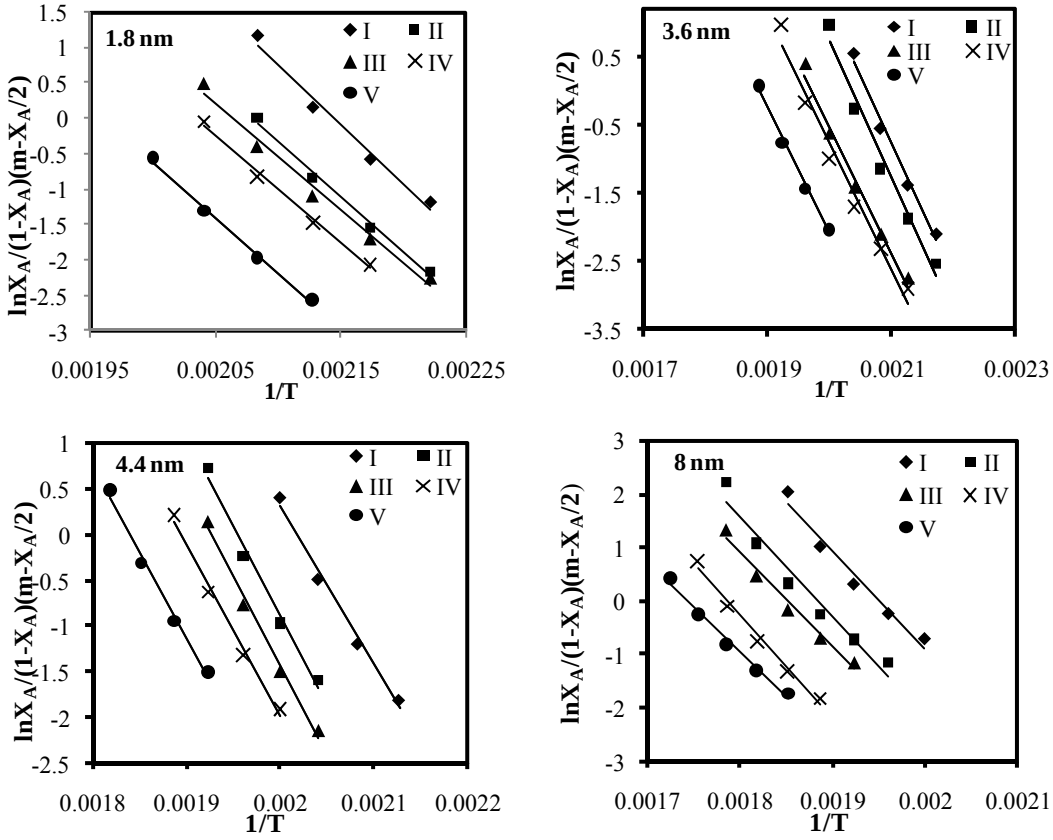

Fig. 4.13. $\ln {X_A}/{(1-X_A)(m-{X_A}/{2})}$ vs. 1/T (Ea= -slope X R) at various GHSVs (I=3180±180 $cm^3\ h^{-1}g_{cat}^{-1}$, II= 6045±120 $cm^3\ h^{-1}g_{cat}^{-1}$, III = 9075±225 $cm^3\ h^{-1}g_{cat}^{-1}$, IV = 12012±210 $cm^3\ h^{-1}g_{cat}^{-1}$, V = 14955±105 $cm^3\ h^{-1}g_{cat}^{-1}$).

Table 4.1. Comparison of activation energy of various catalysts calculated by differential and integral analysis.

Catalyst	Particle Size (nm)	Activation Energy (Kcal)	
		Integral	Differential
Pt/SBA-15(1.8 nm)	1.8	31.5	30.97
Pt/SBA-15(3.6 nm)	3.6	36.85	37.9
Pt/SBA-12(4.4 nm)	4.4	39.7	37.3
Pt/SBA-15(8 nm)	8	35.5	35.9

4.5.3. Specific Activity

We calculated the total active sites on surface of each catalyst from the average size of the Pt particles which was calculated from TEM images. Particles were assumed to be spherical for calculating the average particle size. The fact that some area may be in contact with the channel walls was not taken in to consideration. Specific activity i.e. yields per site at various temperatures for various GHSVs were calculated from the conversions at those temperatures (Fig. 4.14). For GHSVs 3180±180 cm^3 h^{-1} g_{cat}^{-1} and 6045±120 cm^3 h^{-1} g_{cat}^{-1}, specific activity does not vary with particle size. But smaller particle size (1.8 nm) show comparatively high specific activity for 9075±225 cm^3 h^{-1} $g_{cat}^{-1}$and 12012±210 cm^3 h^{-1} g_{cat}^{-1} and 14955±105 cm^3 h^{-1} g_{cat}^{-1} GHSVs at 494, 495 and 517K respectively while it does not vary change much when particle size changes from 3.6 to 8 nm.

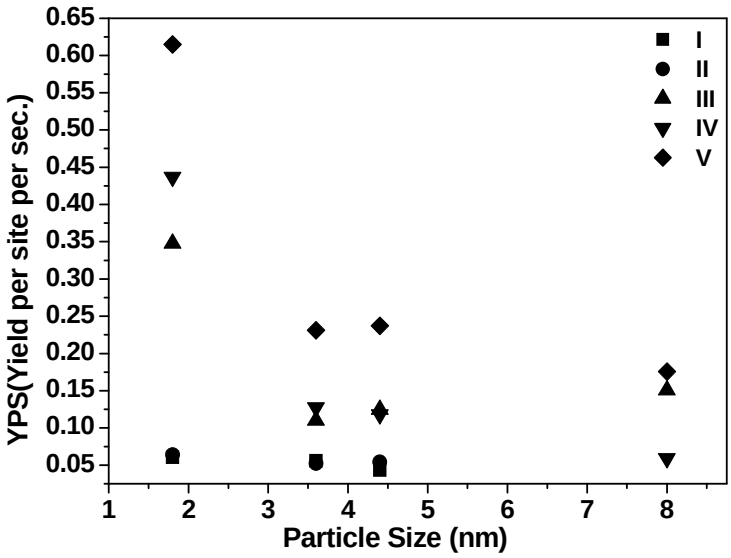

Fig. 4.14. Variation of yield per site per second with particle size at various GHSVs and temperatures (I=3180±180 cm^3 $h^{-1}g_{cat}^{-1}$, T = 473 K; II= 6045±120 cm^3 $h^{-1}g_{cat}^{-1}$, T = 473 K; III = 9075±225 cm^3 $h^{-1}g_{cat}^{-1}$, T = 494 K; IV = 12012±210 cm^3 $h^{-1}g_{cat}^{-1}$, T = 495 K; V = 14955±105 cm^3 $h^{-1}g_{cat}^{-1}$, T = 517 K).

4.6. Effect of Particle Size on Chemoselectivity in Cinnamaldehyde Hydrogenation

Cinnamaldehyde (CAL) hydrogenation was carried out at 60°C under 30 bar H_2 pressure for all the catalysts. Pt\substrate ratio was 0.001 (molar) and CAL/isopropanol ratio (by wt.) was kept 0.03 for all the catalytic reactions. In the given reaction conditions, three products were obtained i.e. cinnamyl alcohol (CA), hydrocinnamaldehyde (HCAL), and phenyl propanol (PP) (Scheme 4.1).

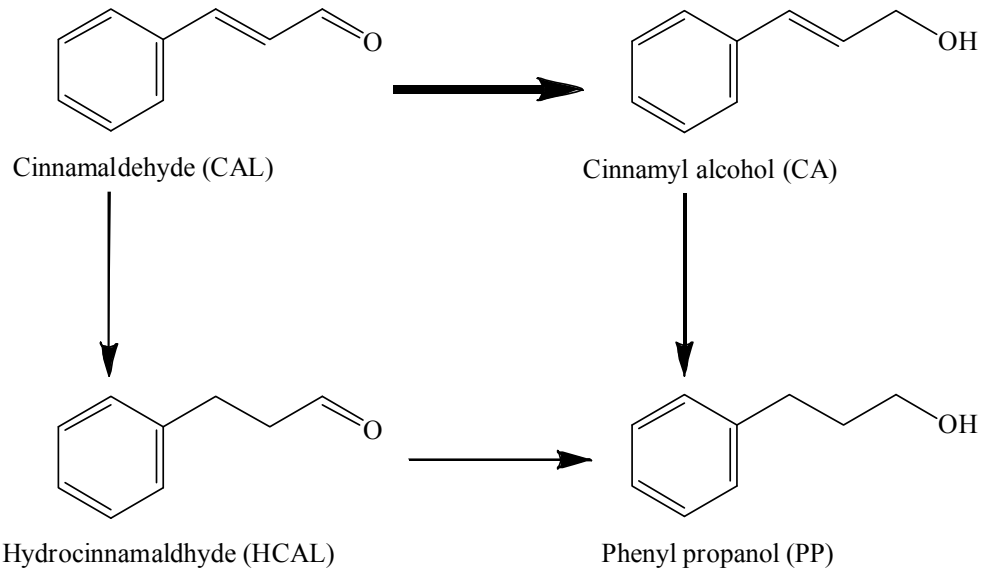

Scheme 4.1. Different pathways for the hydrogenation of cinnamaldehyde.

With all the catalysts, cinnamyl alcohol was obtained as major product. Distribution of products of the reaction with time and variation of product yield with conversion for Pt/SBA-15(1.8 nm) is given in Fig. 4.15.

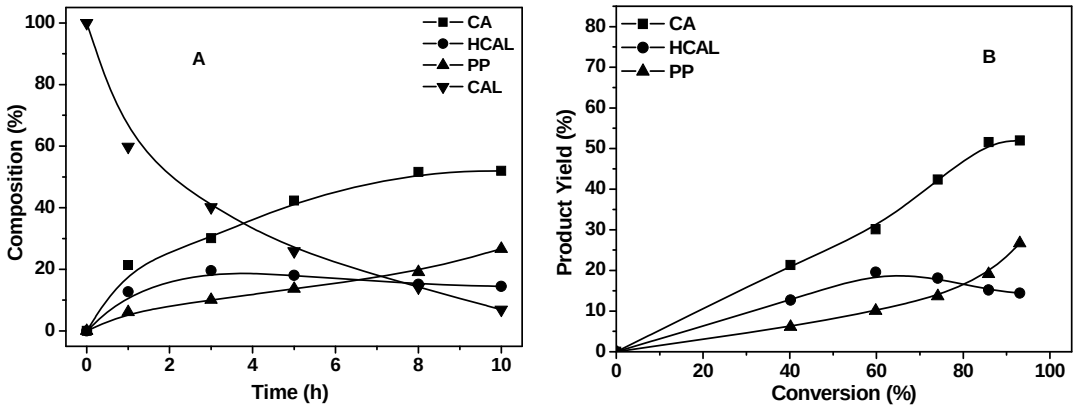

Fig. 4.15. Cinnamaldehyde hydrogenation on Pt/SBA-15(1.8 nm) catalyst; A) composition (%) vs. time, B) product yield vs. conversion.

After 1 h, 21.4% yield of cinnamyl alcohol is obtained at 40.2% conversion. Yield increases with conversion and goes up to maximum 52% after 10 h when conversion

is 93%. Hydrocinnamaldehyde yield increases up to 18% at 5 h when conversion is 74% after which it starts decreasing. Amount of phenyl propanol goes on increasing as reaction proceeds and at the end of reaction i.e. after 10 h it is 26.7%. From this we can conclude that in the given reaction conditions, C=O bond is hydrogenated faster than C=C bond, giving more cinnamyl alcohol. Although hydrocinnamaldehyde is also obtained as a result of hydrogenation of C=C bond but as soon as amount increases to 18% its concentration starts decreasing because of further hydrogenation of C=O bond to give phenyl propanol which is final product.

In the hydrogenation of cinnamaldehyde on Pt/SBA-15(3.6 nm), yield for cinnamyl alcohol is 25% after 1 h, as reaction proceeds it increases and reaches 57% after 10 h. More yield for cinnamyl alcohol on Pt/SBA-15(3.6 nm) indicates the faster hydrogenation of C=O bond in comparison to Pt/SBA-15(1.8 nm). Amount of hydrocinnamaldehyde goes on increasing with time and reaches maximum 12.8% at 5 h. Maximum yield of 24% is obtained for phenylpropanol when conversion is 92% after 10 h.

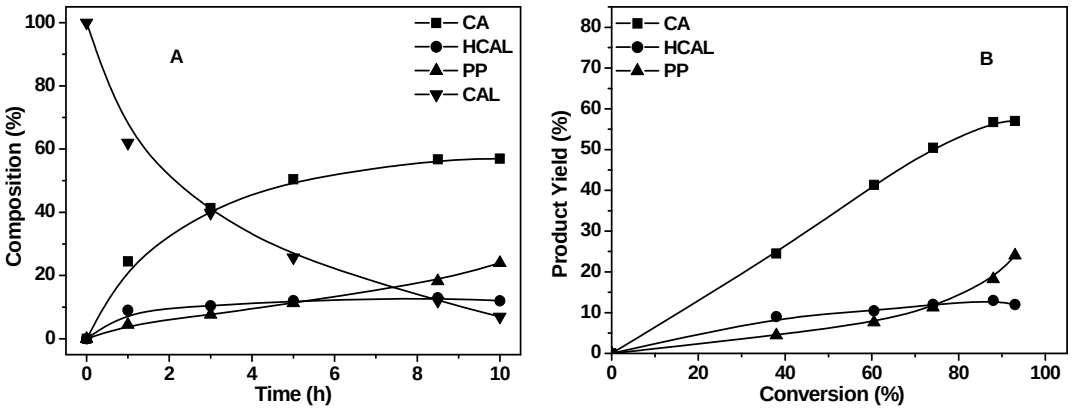

Fig. 4.16. Cinnamaldehyde hydrogenation on Pt/SBA-15(3.6 nm) catalyst; A) composition (%) vs. time, B) product yield vs. conversion.

Pt/SBA-12 (4.9 nm) gives 61.3% yield of cinnamyl alcohol after 10 h at 94% conversion. Here also, it is the major product in the reaction mixture (Fig. 4.17). Yield of hydrocinnamaldehyde is always less than obtained on Pt/SBA-15(1.8 nm) and Pt/SBA-15(3.6 nm) throughout the reaction and reaches maximum up to 12.3% at 75.2% conversion after 5.1 h. Phenyl propanol amount goes on increasing with time (21.6% after 10 h) indicating that both hydrocinnamaldehyde and cinnamyl alcohol gets hydrogenated with time as their concentration increases. Decreased amount of hydrocinnamaldehyde and simultaneous increase in yield of cinnamyl alcohol throughout the reaction in comparison to Pt/SBA-15(1.8 nm) and Pt/SBA-12(3.6 nm)

indicates that hydrogenation of C=O becomes comparatively faster as particle size increases from 1.8 to 4.9 nm.

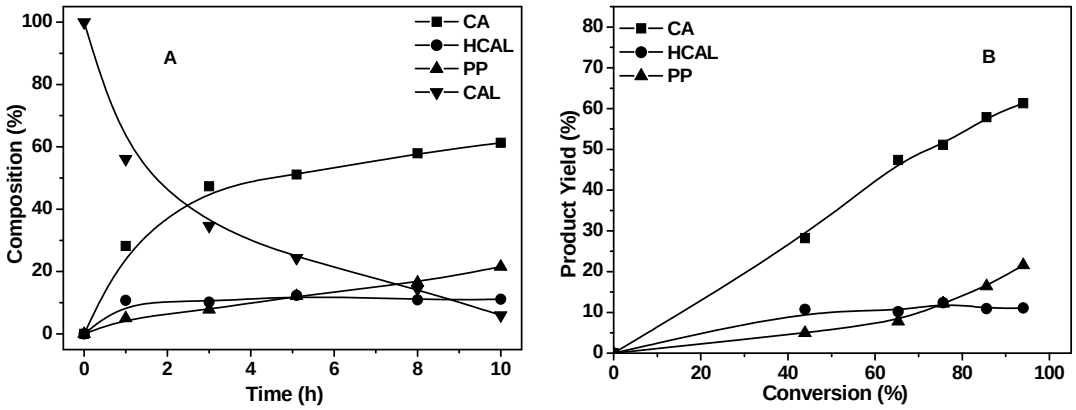

Fig. 4.17. Cinnamaldehyde hydrogenation on Pt/SBA-12(4.9 nm) catalyst; A) composition (%) vs. time, B) product yield vs. conversion.

Pt/SBA-15 (8 nm) gives highest yield for cinnamyl alcohol i.e. 76% after 10 h of reaction. Yield of hydrocinnamaldehyde increase with time up to 5 h to maximum 7.5% at 86% conversion and after that it starts decreasing. Amount of phenyl propanol goes on increasing with time and reaches to 17.1% after 10 h at 96.5% conversion. Increase in the yield of cinnamyl alcohol in comparison to Pt/SBA-12 (4.9 nm), indicates that hydrogenation of C=O bond becomes further faster as particle size increases from 4.9 nm to 8 nm.

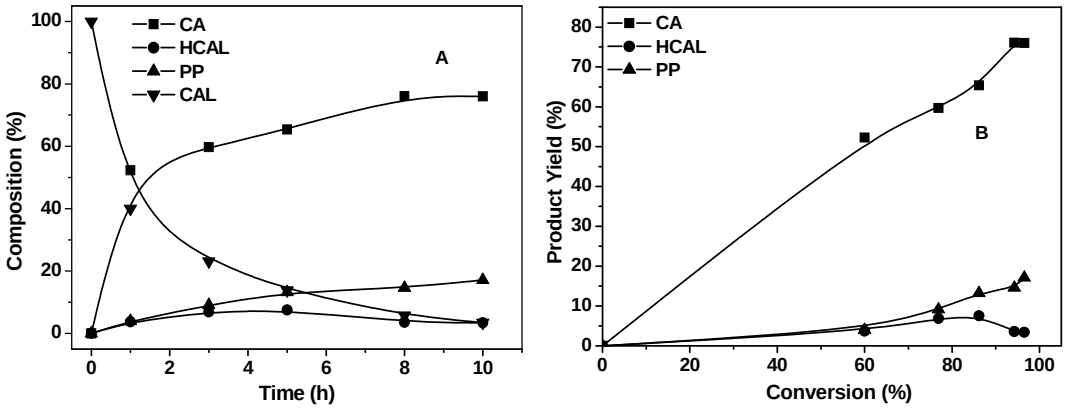

Fig. 4.18. Cinnamaldehyde hydrogenation on Pt/SBA-15(8 nm) catalyst; A) composition (%) vs. time, B) product yield vs. conversion.

Thus, the yield of cinnamyl alcohol increases with increase in particle size and follow the order 8 nm > 4.9 nm >3.6 nm >1.8 nm. Selectivities of cinnamyl alcohol at 50% and 75% conversions on various catalysts have been given in Table 4.2.

Table 4.2. Selectivity of cinnamyl alcohol at 50% (S^{50}) and 75% (S^{75}) conversions on various catalysts.

Catalyst	Av. Particle size (nm)	S^{50}	S^{75}
Pt/SBA-15(1.8 nm)	1.8	51	57
Pt/SBA-15(3.6 nm)	3.6	66	67
Pt/SBA-12(4.9 nm)	4.9	65	69
Pt/SBA-15(8 nm)	8	68	80

As clear from the table, Pt/SBA-15(1.8 nm) with smallest particle size gives minimum selectivity while Pt/SBA-15(8 nm) with largest particle size gives maximum selectivity at 50% and 75% conversion. Fig. 4.19 A and 4.19 B shows the variation of conversion (%) and selectivity for cinnamyl alcohol for all the four catalysts respectively.

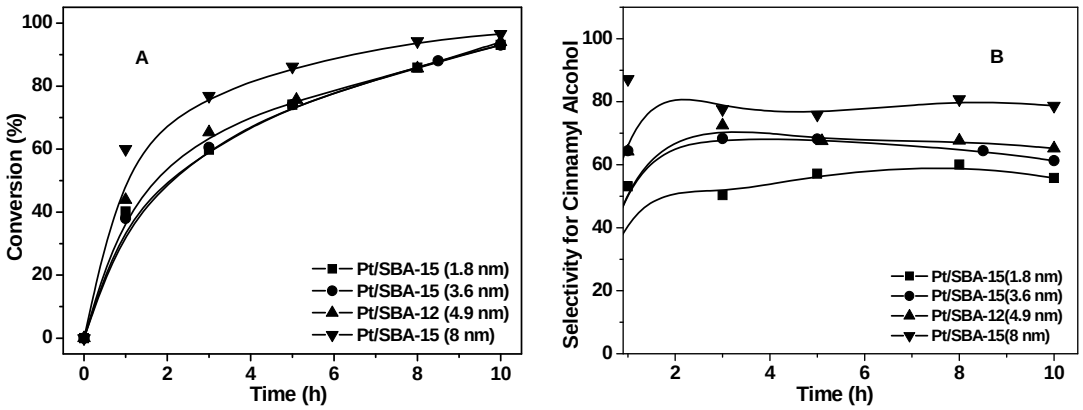

Fig. 4.19. Comparison of Pt/SBA materials with various sizes of Pt particles; A) conversion (%) vs. time, B) variation of selectivity for cinnamyl alcohol with time.

More selectivity for cinnamyl alcohol among all the products on the platinum surface can be explained on basis of width of d-bands of platinum [34, 40]. Because of larger d bandwidth in platinum, the repulsive interaction of C=C with the surface increases, hence reactant molecule prefers to adsorb through C=O. Increase in selectivity of cinnamyl alcohol from 57% to 80% as particle size increases from 1.8 nm to 8 nm can be attributed to change in the extent of exposure of different crystallographic planes with increasing particle size. As particle size increases, the abundance of Pt (111) planes increases [41]. Pt (111) surface is a flat and dense surface and the amount of steps is lower in (111) than in (100) face [42]. The number

of edges and kinks on the surface also decreases with increase in particle size. Cinnamaldehyde molecule being a planar molecule cannot adsorb parallel to a flat metal surface because of the steric repulsion of the aromatic ring [43, 44]. Because of this steric strain C=C bond cannot approach the surface as closely as the C=O bond. But this steric effect has less pronounced effect on small particles (Fig. 4.20).

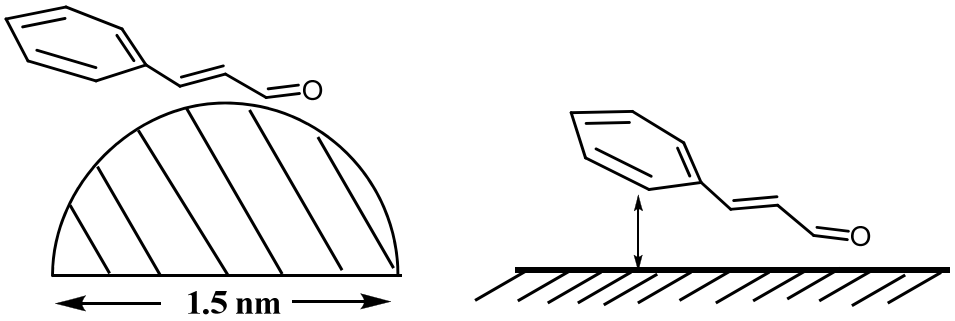

Fig. 4.20. Scheme of cinnamaldehyde adsorption on a small metal particle and on a flat surface. (Ref. 44.)

So, on bigger particles with more flat surface, C=O bond approaches closely to the surface than C=C bond and then hydrogenated preferentially while in smaller particles both the C=C and the C=O can approach the surface. As the particle size increases the exposure of flat Pt (111) faces increases and edges and corners decreases, this increases the probability of activation of C=O bond in comparison to C=C bond, hence selectivity of cinnamyl alcohol increases.

4.4. SUMMARY

In the present chapter, Pt/SBA materials synthesized by *in situ* method as described in chapter 2 and 3 and by known method reported in literature have been tested for CO oxidation and cinnamaldehyde hydrogenation. Materials have been well characterized by XRD and TEM. From TEM images particle size distribution has been calculated. CO oxidation has been carried out at various GHSVs and effect of temperature on conversion has been studied. All the catalysts have been compared for their activity at various GHSVs and activation energy has been calculated by differential and integral analysis based on first principles. Activation energies calculated by both methods are in close agreement with each other indicating that there is no mass transfer limitation. Specific activity has been found to be more for the Pt/SBA-15 with smaller particles (1.8 nm) while it remains constant for higher particle sizes varying from 3.6 to 8 nm. In hydrogenation of cinnamaldehyde, higher

selectivity for cinnamyl alcohol has been obtained on all the catalysts. Selectivity for cinnamyl alcohol increases from 57% to 80% at 75% conversion as particle size increases from 1.8 nm to 8 nm. The increase in selectivity has been attributed to preferred adsorption of C=O bond in comparison to C=C bond on flatter surface which increase with increase in particle size as Pt (111) planes become more abundant.

4.5. REFERENCES

1. M. Boudart, *Adv. Catal.* **1969**, *20*, 153.
2. M. Che, C. O. Bennette, *Adv. Catal.* **1989**, *36*, 55.
3. G. C. Bond, *Chem. Soc. Rev.* **1991**, *20*, 441.
4. R. A. van Santen, *Acc. Chem. Res.* **2009**, *42*, 57.
5. A. K. Prashar, R. P. Hodgkins, R. Kumar, R. N. Devi, *J. Mater. Chem.* **2008**, *18*, 1765.
6. R. M. Rioux, H. Song, J. D. Hoefelmeyer, P. Yang, and G. A. Somorjai, *J. Phys. Chem. B* **2005**, *109,* 2192.
7. T. Engel, G. Ertl, *Adv. Catal.* **1979**, *28*, 1.
8. G. A. Somorjai, *Introduction to Surface Chemistry and Catalysis*, Wiley: New York, 1994.
9. M. S. Chen, Y. Cai, Z. Yan, K. K. Gath, S. Axnanda, D. W. Goodman, *Surf. Sci.* **2007**, *601*, 5326.
10. S. M. McClure, D. W. Goodman, *Chem. Phys. Lett.* **2009**, *469*, 1.
11. G. Blyholder, *J. Chem. Phys.* **1964**, *68*, 2772.
12. M. Boudart and G. Djéga-Mariadassou, *Kinetics of Heterogeneous Catalytic Reactions* (Princeton University Press, Princeton), NJ, 1984.
13. B. E. Nieuwenhuys, V. Ponec, G. van Koten, P. W. N. M. van Leeuven and R. A. Santen, Bonding and elementary steps in catalysis, Chapter 4 in *Studies in Surface Science and Catalysis 79*, Elsevier Science Publisher, B. V. Amsterdam, 1993.

14. K. W. Kolasinski, *Surface Science-Foundations of Catalysis and Nanoscience*, John Wiley & Sons Ltd., 2002.

15. I. Langmuir, *Trans. Farad. Soc.* **1922**, *17*, 621.

16. C. N. Hinshelwood, *The kinetics of Chemical Change*, Clarendon Press, Oxford, 1940.

17. C. T. Campbell, G. Ertl, H. Kuipers, J. Segner, *J. Chem. Phys.***1980**, *73*, 5862.

18. G. Ertl, *Langmuir* **1987**, *3*, 4.

19. D. D. Eley, E. K. Rideal, *Nature* **1946**, *146*, 401.

20. C. C. Cheng e*t al*., *J. Am. Chem. Soc.* **1992**, *114*, 1249.

21. H. Over, Y. D. Kim, A. P. Seitonen, S. Wendt, E. Lundgren, M. Schmidt, P. Varga, A. Morgante, G. Ertl, *Science* **2000**, *287*, 1474.

22. P. Mars, D. W. van Krevelen, *Spec. Suppl. to Chem. Eng . Sci.* **1954**, *3*, 41.

23. B. L. M. Hendriksen, J. W. M. Frenken, *Phys. Rev. Lett*. **2002**, *89*, 046101.

24. M. L. D. Ackermann *et al.*, *Phys. Rev. Lett.* **2005**, *95,* 255505.

25. M. Haruta, S. Tsubota, T. Kobayashi, H. Kageyama, M. J. Genet, B. Delmon, *J. Catal.* **1993**, *144*, 175.

26. M. E. Grass, Y. Zhang, D. R. Butcher, J. Y. Park, Y. Li, H. Bluhm, K. M. Bratlie, T. Zhang, G. A. Somorjai, *Angew. Chem., Int. Ed.* **2008**, *47*, 8893.

27. N. W. Cant, P. C. Hicks, B. S. Lennon, *J. Catal.* **1978**, *54*, 372.

28. E. McCarthy, J. Jahradnik, G. C. Kuczynski, J. J. Carberry, *J. Catal.* **1975**, *39*, 29.

29. K. Weissermel and H. J. Arpe, *Industrial Organic Chemistry*, Verlag Chemie, Weinheim, 1978.

30. K. Bauer and D. Garbe, *Common Fragrance and Flavor Materials*, VCH, Weinheim, 1985.

31. K. Bauer and D. Garbe, in *Ullman Encyclopedia*, VCH, New York, 1988, All, p. 141.

32. C. Mohr, P. Claus, *Sci. Progress*, **2001**, *84*, 311.

33. J. March, *Advanced Organic Chemistry*, McGraw-Hill Kogakusha, Tokyo, 1977, p. 829.

34. F. Delbecq, P.J. Sautet, *J. Catal*. **1995**, *152*, 217.

35. P. Gallezot, D. Richard, *Catal. Rev.-Sci. Eng*. **1998**, *40*, 81.

36. D. Y. Zhao, Q. Huo, J. Feng, B. F. Chmelka, G. D. Stucky, *J. Am. Chem. Soc.* **1998**, *120*, 6020.

37. A. E. Altman, R. J. Gorte, *J. Catal.* **1988**, *110*, 191.

38. G. S. Zafiris, R. J. Gorte, *J. Catal*. **1993**, *140*, 418.

39. N. W. Cant, P. C. Hicks, B. S. Lennon, *J. Catal.* **1978**, 54, 372.

40. Y. A. Ryndin, C. C. Santini, D. Prat, J. M. Basset, *J. Catal.* **2000**, *190*, 364.

41. M. Englisch, A. Jentys, J. A. Lercher, *J. Catal.* **1997**, *166*, 25.

42. R. I. Masel, *Principles of Adsorption and Reaction on Solid Surfaces,*Wiley, New York, 1996.

43. C. Minot, P. Gallezot, *J. Catal.* **1990**, *123*, 341.

44. A. Giroir-Fendler, D. Richard, P. Gallezot, *Catal. Lett.* **1990**, *5*, 175.

CHAPTER 5

SUMMARY AND CONCLUSIONS

5.1. SUMMARY

The present thesis gives an account of

(i) *In situ* synthesis of Pt, Au and Pt-Au nanoparticles in the mesoporous channels of SBA-15

(ii) Synthesis of different morphologies of Pt in SBA-15 channels and fine tuning of the size by synthesising Pt nanoparticles of 4-5.5 nm in the channels of mesoporous SBA-12.

(iii) Effect of platinum particle size on the activation energy of CO oxidation and selectivity in cinnamaldehyde hydrogenation using Pt/SBA materials with different sizes of platinum particles.

Chapter 1 presents a general introduction to the role of metal nanoparticles in heterogeneous catalysis and effect of shape and size in controlling the selectivity of the reaction. It gives details about current status of synthesis procedure of metal nanoparticles in homogeneous medium and their drawback in being used as catalysts. Advantages of mesoporous silica as support for metal nanoparticles have been described. A brief survey of various methods available in literature for synthesizing metal nanoparticles in mesoporous silica channels is also given. Various properties of metal nanoparticles stabilized in mesoporous silica channels like thermal stability, catalytic, optical and magnetic have been described. Basic principles of various physicochemical characterization techniques like X-Ray diffraction, N_2 adsorption, TEM, SEM, UV-Visible spectroscopy, IR and NMR spectroscopy and ICP-OES have been described in detail.

Chapter 2 describes *in situ* method for the synthesis of metal nanoparticles in mesoporous channels of SBA-15. Different SBA-15 materials with varying conc. of CTAB in P123 have been synthesized and characterized by XRD, N_2 adsorption, and SEM. Increase in CTAB conc. results in decrease in mesoporous order of final SBA-15. So, an optimum conc. of 1 mM CTAB was selected to incorporate Pt in SBA-15. XRD and TEM of calcined Pt/SBA-15 showed platinum nanoparticles of average size 8 nm in the mesoporous channels of SBA-15. Mechanism of formation of platinum nanoparticles has been studied by *in situ* XRD and UV-Visible studies. Au and Pt-Au nanoparticles have also been synthesised in SBA-15 using same *in situ* method and materials have been characterized by XRD, UV-Visible studies and TEM.

Chapter 3 deals with the synthesis of various size and morphologies of platinum nanoparticles in mesoporous silica channels. This chapter is divided into two parts.

Part A deals with synthesis of various morphologies of Pt in mesoporous SBA-15 channels. It has been found that change in stirring time of platinum precursor with polymer-CTAB mixed micelle composite results in different morphologies of platinum in the final material. TEM studies of the synthesised material showed that predominant morphology of platinum particles changes from spherical (95%) (stirring time 15 min) to rugby ball (61%) at 4 h stirring time and stirring for longer duration (8 h) results in nanorods morphology (68%). There are two possible mechanisms at play (i) sintering at higher temperature leads to elongated morphologies or (ii) formation of elongated shapes at the precursor stage itself. We did not observe the formation of nanorods in the samples synthesised with 15 min stirring time even after calcination up to 800°C. This rules out the role of sintering at high temperature in the formation of different morphologies. UV-Visible studies and NMR studies of metal precursor mixed micelle composite were done to find out the mechanism of formation of different morphologies. UV-Visible studies show that there is shift of ligand to metal charge transfer band with change in CTAB concentration in precursor mixed micelle composite. This indicates that $[PtCl_6]^{2-}$-CTAB cluster complex diffuse and agglomerate with time and set the stage for the formation of different morphologies in the final material. This was also supported by NMR and IR studies.

Part B describes the synthesis of Pt nanoparticles of average size 4.4 and 4.9 nm in the channels of mesoporous SBA-12 using the *in situ* method. Different SBA-12 materials have been synthesized with various concentration of CTAB in 4 wt% Brij 76 to find out the optimum concentration of CTAB to incorporate platinum. Platinum nanoparticle of narrow size distribution of 4-5.5 nm could be synthesised in channels of mesoporous SBA-12. Since increase in CTAB concentration reduces the pore size of SBA-12, Pt/SBA-12 materials were synthesized with various concentrations of CTAB to find out the effect of concentration of CTAB on Pt particle size. We also studied the effect of increasing the loading on the size of Pt particles by synthesizing Pt/SBA-12 by varying the conc. of Pt precursor in mixed micelle composite template. It results in the formation of some larger size particles outside the channels also. Effect of CTAB concentration on the retention of Pt has been studied

by ICP analysis which shows that increase in CTAB concentration increases the % retention of platinum in the final material. Platinum has also been incorporated in to FDU-12, a three dimensional cubic mesoporous material. Effect of different concentrations of CTAB on the mesoporous order of FDU-12 also has been studied by varying the concentration of CTAB in 1 wt% F127 during the synthesis. All synthesized materials i.e. SBA-12, Pt/SBA-12, FDU-12 and Pt/FDU-12 have been characterized by XRD, N_2 adsorption, SEM and TEM.

Chapter 4 presents catalytic study of Pt/SBA materials with different Pt particle sizes. CO oxidation has been taken as model reaction to study the effect of particle size on the activity. It has been carried out at various GHSVs and effect of temperature on conversion has been studied. All the catalysts have been compared for their activity at various GHSVs and activation energy has been calculated by differential and integral analysis based on first principles. Activation energies calculated by both methods are in close agreement with each other indicating that there is no mass transfer limitation. Specific activity has been found to be more for the Pt/SBA-15 with smaller particles (1.8 nm) while it remains constant for higher particle sizes varying from 3.6 to 8 nm. Hydrogenation of cinnamaldehyde has been taken as model reaction to study the effect of particle size on selectivity. In cinnamaldehyde hydrogenation, higher selectivity for cinnamyl alcohol has been obtained on all the catalysts. Selectivity for cinnamyl alcohol increases from 57% to 80% at 75% conversion as particle size increases from 1.8 nm to 8 nm.

5.2. CONCLUSIONS

5.2.1. *In situ* synthesis of metal nanoparticles in mesoporous SBA-15

- Negatively charged metal salt precursors (e. g. $[PtCl_6]^{2-}$) get dispersed in the mixed micelle composite of CTAB and P123 because of electrostatic interaction with the +ve head of CTAB.
- When silica precursor is added to acidic solution of metal precursor mixed micelle composite, it condenses around the composite and forms silica wall after the hydrothermal treatment. This on calcination gives fairly monodispersed metal particles mostly in the mesoporous channels of SBA-15.

- Addition of higher concentration of CTAB (> 4 mM) results in the loss of mesoporous order as indicated by XRD so 1 mM CTAB was selected to incorporate platinum.
- The Pt incorporated mesoporous material has highly enhanced surface area and adsorption capabilities in comparison to parent materials without any pore blockage.
- *In situ* XRD and UV-Visible studies show that Pt particles are formed during the calcination.
- XRD shows the presence of Au nanoparticles in as synthesized samples also which indicate that the ion pair aggregates seen in case of Pt stabilize it against reduction and agglomeration in the initial stages.
- Au-Pt/SBA-15 shows separate diffraction peaks for Au and Pt, as indicated by the XRD which confirm that the interaction of Pt and Au salts with CTAB and subsequent ion pair formation is inherently different.

5.2.2. Fine tuning of size and morphology of Pt nanoparticles in SBA type materials

- Interaction of Pt precursor with mixed micelle composite for different contact times leads to different morphologies i.e. spherical, rugby ball and nanorods of Pt nanoparticles in mesoporous SBA-15 channels after calcination.
- Mesoporous order is less intact in Pt/SBA-15 with rugby ball and nanorods morphologies and they show less adsorption properties which may be due to formation of pockets not accessible to adsorbed molecules.
- UV-Visible studies of precursor mixed micelle composite show shift in ligand to metal charge transfer band with increase in CTAB conc. while no shift is observed with increase in contact time.
- NMR and IR studies show that $[PtCl_6]^{2-}$ - CTAB ion pair phase separates out but remain in the P123 corona.
- Formation of different morphologies is due to diffusion and agglomeration of $[PtCl_6]^{2-}$ -CTAB in P123 to different extent with time and not the sintering at high temperature.
- CTAB-Brij 76 mixed micelle is comparatively much more stable than CTAB-P123 owing to greater hydrophobicity of hydrocarbon core of Brij 76.

- XRD show that mesoporous order of SBA-12 is retained even up to 32 mM CTAB concentration.
- HRTEM studies show the formation of Pt nanoparticles of 4-5.5 nm in the channels of SBA-12.
- Increase in CTAB concentration does not have much effect on the size of Pt nanoparticle but there is increase in retention of Pt. Increase in loading results in formation of some bigger particles outside the channels also.

5.2.3. CO oxidation and cinnamaldehyde hydrogenation

- Pt/SBA-15 show increase in conversion at particular temperature with decrease in GHSV as contact time increases.
- T_{100} and $T_{light\ off}$ decreases with decrease in particle size and follow the order 8 >4.4 >3.6 >1.8 nm.
- Activation energy for smallest particle size (1.8 nm) are less but increases as particle size increase to 3.6 nm and then remains almost constant with increase in size.
- Specific activity is highest for smallest particle size while it remains constant when particle size increases beyond 3.6 nm.
- All Pt/SBA materials show highest selectivity for cinnamyl alcohol.
- Increase in particle size results in increased extent of (111) plane on Pt particles on which C=O bond is preferably adsorbed than C=C bond leading to higher selectivity for cinnamyl alcohol.

List of Publications

1. *In Situ* Synthesis of Pt Nanoparticles in SBA-15 by Encapsulating in Modified Template Micelles: Size restricted Growth within the Mesochannels
   Atul K. Prashar, Robert P. Hodgkins, Rajiv Kumar and R. Nandini Devi
   J. *Mater. Chem.*, **2008**, *18*, 1765-1770
2. *In Situ* Encapsulation of Pt Architectures of Varying Morphologies in Mesoporous Compounds
   Atul K. Prashar, Robert P. Hodgkins, Jima N. Chandran, P. R. Rajamohanan and R. Nandini Devi
   Chem. Mater., **2010**, *22 (5)*, 1633–1639
3. Ru(II) Phenanthroline Complex as Catalyst for Chemoselective Hydrogenation of Nitro-aryls in a Green Process
   Amit A. Deshmukh, **Atul K. Prashar**, Anil K. Kinage, Rajiv Kumar, and R. Meijboom
   Ind. Eng. Chem. Res., **2010**, *49*, 12180–12184

List of Manuscripts Communicated

1. *In Situ* Encapsulation of Pt Nanoparticles in Mesoporous Silica: Synthesis, Characterization and Effect of Particle Size on CO Oxidation
   Atul K Prashar, S. Mayadevi, P.R. Rajamohanan and R. Nandini Devi
   Applied Catalysis A: General (communicated)
2. Growth of Hydrothermally Stable Mesoporous Silica Structures Interconnected around Microporous Zeolites Crystals
   Anil K. Kinage, **Atul K. Prashar**, Gloria Berlier, Rajiv K. Chaturvedi
   Materials Characterization (communicated)

Contributions to National/International Symposia/Conferences

1. Synthesis of Mesoporous-Microporous Hybrid Material For ß-Amino Alcohol Production

   Atul Kumar, Anil K. Kinage and Rajiv Kumar

   "Catalysis for Future Fuels 18th National Symposium & Indo-US Seminar on Catalysis"
   16–18 April 2007, Indian Institute of Petroleum (IIP), Dehradun ***(Oral Presentation)***

2. Size Restricted Growth of Platinum Nanoparticles within Channels of Mesoporous SBA-15

   Atul K. Prashar, Robert P. Hodgkins, Rajiv Kumar and R. Nandini Devi

   "*Futuristic Materials as Catalysts and Adsorbents, National Workshop on Catalysis"*

   18-20 February 2008, Institute of Minerals and Materials Technology (IMMT), Bhubaneswar-751013 ***(Poster Presentation)***

3. Encapsulation of Platinum Nanoparticles in SBA-15 Channels: Tuning the Different Morphologies of Particles and Their Role in Catalysis

   Atul K. Prashar, Robert P. Hodgkins and R. Nandini Devi

   "Catalysis for Sustainable Energy and Chemicals 19th National Symposium On Catalysis"

   18-21 January 2009, National Chemical Laboratory (NCL), Pune, India **(Oral Presentation)**

4. Synthesis and Characterization of Silicalite/SBA-15 Composites

   Atul Kumar Prashar, Anupam Samanta and Nandini Devi

   "*Catalysis for Sustainable Energy and Chemicals 19th National Symposium On Catalysis"*

   18-21 January 2009, National Chemical Laboratory (NCL), Pune, India. ***(Poster Presentation)***

5. *In situ* Encapsulation of Pt Nano Architectures of Varying Morphologies in Mesoporous Compounds

   Atul K. Prashar, Robert P. Hodgkins and R. Nandini Devi

   "*International Conference on Materials for the Millennium"*

   11-13 January 2010, at Cochin Institute of Applied Science and Technology, Kochi-22, Kerala, India ***(Poster Presentation)***

6. Synthesis and Characterization of ZSM-5/SBA-15 Composites

   Anupam Samanta, **Atul Kumar** and R. Nandini Devi

   "International Conference on Materials for the Millennium"

   11-13 January 2010, at Cochin Institute of Applied Science and Technology, Kochi-22, Kerala, India ***(Poster Presentation)***

7. Effect of Platinum Particle Size over the Activation Energy of CO Oxidation

   Atul Kumar Prashar, S. Mayadevi, R. Nandini Devi

   "Catalysis for Energy Conversion and Conservation of Environment 20th National Symposium"

   19-22 December 2010, Indian institute of Technology (IIT), Madras ***(Oral Presentation)***

APPENDIX-1

1. Calculation of Activation Energy

All the four catalysts SBA-15(1.8 nm), SBA-15(3.6 nm), SBA-12(4.4 nm) and SBA-15(8 nm) containing different sizes of Pt particles were compared for their activation energy calculated based on first principles. Activation energy was calculated by two methods known as rate constant method (based on integral analysis) and direct method (based on differential analysis).

1.1. Integral Analysis

In this method rate constants of reaction at different temperatures were calculated from the data at different flow rates used for each catalyst. Activation energies were found out from the slope of ln k vs. 1/T graph for each catalyst.

CO oxidation reaction when both the reactants are in stoichiometric amount can be given by the following equation:

$$CO + {}^{1}/_{2}\, O_2 \rightarrow CO_2$$

Suppose C_{A_o} = Initial conc. of CO , C_{B_o} = Initial conc. of Oxygen and C_{C_o} = Inital conc. of CO_2

If C_A and C_B are conc. of CO and O_2 at particular time t, then

$$C_A = C_{A_o} - C_{A_o} X_A \ldots\ldots\ldots (1)$$

$$C_B = C_{B_o} - C_{B_o} X_B \ldots\ldots\ldots\ldots\ldots\ldots\ldots\ldots\ldots\ldots\ldots\ldots\ldots\ldots\ldots\ldots\ldots\ldots\ldots\ldots\ldots\ldots\ldots\ldots\ldots\ldots\ldots\ldots (2)$$

$$\text{Here, } C_{B_o} X_B = C_{A_o} {}^{X_A}/_{2} \ldots\ldots\ldots\ldots\ldots\ldots\ldots\ldots\ldots\ldots\ldots\ldots\ldots\ldots\ldots\ldots\ldots\ldots\ldots\ldots\ldots\ldots\ldots\ldots\ldots\ldots (3)$$

Rate of disappearance of CO is given by

$$-\frac{dC_A}{dt} = C_{A_o} \frac{dX_A}{dt} = k C_A C_B \ldots\ldots\ldots\ldots\ldots\ldots (4)$$

Substituting the values of C_A and C_B in equation (4), we get

$$C_{Ao} \frac{dX_A}{dt} = k(C_{Ao} - C_{Ao} X_A)\left(C_{Bo} - C_{Ao} {}^{X_A}/_{2}\right) \ldots\ldots\ldots\ldots\ldots\ldots\ldots\ldots\ldots\ldots\ldots\ldots\ldots\ldots\ldots\ldots\ldots\ldots\ldots\ldots\ldots\ldots\ldots\ldots\ldots\ldots\ldots\ldots (5)$$

$$C_{Ao} \frac{dX_A}{dt} = k C_{Ao}^2 (1 - X_A)\left(m - {}^{X_A}/_{2}\right) \ldots\ldots\ldots\ldots\ldots\ldots\ldots\ldots\ldots\ldots\ldots\ldots\ldots\ldots\ldots\ldots\ldots\ldots\ldots\ldots\ldots\ldots\ldots\ldots\ldots\ldots\ldots\ldots (6)$$

$$\text{Here } m = \frac{C_{Bo}}{C_{Ao}}$$

On rearranging above equation we get:

$$\frac{dX_A}{(1-X_A)\left(m-{X_A}/{2}\right)} = \mathrm{kC_{Ao}dt} \ldots\ldots\ldots\ldots\ldots\ldots\ldots (7)$$

On integrating both sides of eqn. (7):

Integrating left hand side we get:

$$\int \frac{dX_A}{(1-X_A)\left(m-{X_A}/{2}\right)} = \int \frac{2}{(2m-1)}\frac{dX_A}{(1-X_A)} - \int \frac{1}{(2m-1)}\frac{dX_A}{\left(m-{X_A}/{2}\right)}$$

$$= -\frac{2}{(2m-1)}\frac{dX_A}{(1-X_A)} + \frac{2}{(2m-1)}\frac{dX_A}{m-{X_A}/{2}}$$

$$= \frac{2}{(2m-1)}\left[-\ln(1-X_A) + \ln\left(m-{X_A}/{2}\right)\right]$$

$$= \frac{2}{(2m-1)}\ln\frac{\left(m-{X_A}/{2}\right)}{(1-X_A)}$$

Integrating right hand side:

$$\int \mathrm{kC_{Ao}dt} = \mathrm{kC_{Ao}t}$$

After integration equation becomes:

$$\frac{2}{(2m-1)}\ln\frac{\left(\mathrm{m}-{\mathrm{X_A}}/{2}\right)}{(1-\mathrm{X_A})} = \mathrm{kC_{Ao}t} \ldots\ldots\ldots\ldots\ldots\ldots (8)$$

On rearranging we get:

$$\ln\frac{\left(\mathrm{m}-{\mathrm{X_A}}/{2}\right)}{(1-\mathrm{X_A})} = \mathrm{kC_{Ao}}\frac{(2\mathrm{m}-1)}{2}\mathrm{t} \ldots\ldots\ldots\ldots\ldots\ldots\ldots\ldots (9)$$

But $\mathrm{k} = \mathrm{k_o e^{-E_a/RT}} \ldots\ldots\ldots\ldots\ldots\ldots\ldots\ldots (10)$

Taking log on both sides:

$$\ln \mathrm{k} = \ln \mathrm{k_o} - \frac{\mathrm{E_a}}{\mathrm{RT}} \ldots\ldots\ldots\ldots\ldots\ldots\ldots (11)$$

1.2. Differential Analysis

In this method, activation energies were calculated from the data at different flow rates for each catalyst. Since our catalyst weight was very small (0.4 g), the reactor system could be considered to be a differential reactor.

For small amount of catalyst, rate of disappearance CO can be given by:

$$-\frac{dC_A}{dt} = \frac{C_{Ao} - C_A}{t} = \frac{C_{Ao}X_A}{t} \dots\dots\dots\dots\dots\dots\dots (12)$$

$$\text{Since , } \quad -\frac{dC_A}{dt} = kC_AC_B \dots\dots\dots\dots\dots \text{from (4)}$$

$$\text{But } \quad kC_AC_B = kC_{Ao}^2(1 - X_A)\left(m - {X_A}/{2}\right) \dots\dots\dots\dots\dots \text{from (4) and (6)}$$

So,

$$\frac{C_{Ao}X_A}{t} = kC_{Ao}^2(1 - X_A)\left(m - {X_A}/{2}\right) \dots\dots\dots\dots\dots\dots\dots (13)$$

On rearranging the above expression we get:

$$\frac{X_A}{(1 - X_A)\left(m - {X_A}/{2}\right)} = kC_{Ao}t$$

$$\text{Here } k = k_o e^{-{E_a}/{RT}}$$

$$\frac{X_A}{(1 - X_A)\left(m - {X_A}/{2}\right)} = k_oC_{Ao}t\, e^{-{E_a}/{RT}} \dots\dots\dots\dots\dots\dots (14)$$

Taking logarithm on both sides:

$$\ln\frac{X_A}{(1 - X_A)\left(m - {X_A}/{2}\right)} = \ln k_o\, C_{Ao}t - {E_a}/{RT} \dots\dots\dots\dots\dots\dots (15)$$

The activation energy E_a was calculated directly from the slope of the straight line graph obtained by plotting LHS of Eqn. (15) against 1/T at constant t.